

# Electron injection and acceleration in the bubble regime

Inaugural Dissertation

zur Erlangung des Doktorgrades der  
Mathematisch-Naturwissenschaftlichen Fakultät der  
Heinrich-Heine-Universität Düsseldorf

vorgelegt von

**Johannes THOMAS**  
aus Düsseldorf

Düsseldorf, August 21, 2015

aus dem Institut für Theoretische Physik 1  
der Heinrich-Heine-Universität Düsseldorf

Gedruckt mit der Genehmigung der  
Mathematisch-Naturwissenschaftlichen Fakultät der  
Heinrich-Heine-Universität Düsseldorf

Referent: Prof. Dr. Alexander Pukhov  
Korreferent: Prof. Dr. Markus Büscher

Tag der mündlichen Prüfung: 04.02.2015

# Erklärung

Ich, Johannes THOMAS, versichere hiermit, dass ich die vorliegende Dissertation selbstständig und ohne unzulässige, fremde Hilfe angefertigt habe. Alle von mir verwendeten Quellen und Hilfsmittel sind angegeben.

Unterschrift:

---

Ort, Datum:

---



# *Zusammenfassung*

## **Electron injection and acceleration in the bubble regime**

von Johannes THOMAS

Einige der grundlegendsten Fragen der Physik lassen sich heute nur noch mit Hilfe von Experimenten an Teilchenbeschleunigern beantworten (weitere Informationen sind z.B. unter [http://www.weltmaschine.de/cern\\_und\\_lhc/cern/](http://www.weltmaschine.de/cern_und_lhc/cern/) erhältlich). Dabei werden immer höhere Stoßenergien und immer hochwertigere Teilchenstrahlen benötigt. Um die Energie der beschleunigten Teilchen zu erhöhen, müssen herkömmliche Beschleunigersysteme wie Linear- und Zirkularbeschleuniger immer weiter ausgebaut und vergrößert werden. Eine Verstärkung der beschleunigenden elektromagnetischen Felder ist auf Grund sonst auftretender Materialschäden nicht möglich. Ein anderer Ansatz, der diese Schwäche nicht hat, ist die Beschleunigung von Elektronen in Plasmen. Hierbei wird ein Laserpuls, oder ein kurzer hoch energetischer Elektronenstrahl in ein Plasma geschossen um dort freie Elektronen direkt durch den Laser, oder durch eine vom Laserpuls getriebene Plasmawelle zu beschleunigen.

Plasmawellen, die durch kurze hoch-intensive Laserpulse angeregt werden, beherbergen in ihrem Inneren elektromagnetische Felder, die um viele Größenordnungen höher als in herkömmlichen Beschleunigern sind. Ist die Breite des Laserpulses kürzer als eine halbe Plasmawellenlänge, werden Plasmawellen angeregt, die nach einer halben Periode brechen. Eine Besonderheit dieser gebrochenen Wellen ist, dass sie ein Volumen im Plasma bilden, aus dem alle Elektronen entrückt sind, und das sich mit annähernd Lichtgeschwindigkeit durch das Plasma bewegt. Auf Grund seiner Form wird ein solches Volumen auch als Bubble bezeichnet. Elektronen, die in der beschleunigenden Phase der Bubble gefangen werden, formen einen dichten Elektronenstrahl und können innerhalb von wenigen cm auf Energien von einigen GeV beschleunigt werden.

In dieser Arbeit werden verschiedene analytische Bubble Modelle vorgestellt, die individuelle Problemstellungen behandeln. Zuerst wird dabei eine neue Injektionsmethode vorgestellt, bei der ein kurzer Teilchenstrahl seitlich in die Bubble geschossen wird. Dadurch wird die Breite der Energieverteilung des Elektronenstrahls minimiert. Anschließend wird berücksichtigt, dass hoch energetische Elektronen in elektromagnetischen Feldern viel Energie durch Strahlung verlieren. Zum Schluss wird ein neues Model eingeführt, das das Hintergrundplasmadichteprofil für gegebene Felder bestimmbar macht.



# *Abstract*

## **Electron injection and acceleration in the bubble regime**

by Johannes THOMAS

Some of today's most basic questions in physics can only be answered with experiments at particle accelerators (further information is available at [http://www.weltmaschine.de/cern\\_und\\_lhc/cern/](http://www.weltmaschine.de/cern_und_lhc/cern/)). In order to access new research fields the particle energy and the beam quality have to be increased continuously. In order to achieve this, conventional accelerators, like linear and circular accelerators, have to be extended and enlarged since amplification of the accelerating electromagnetic fields is not possible because too large field strengths may cause material damages. Another method that does not suffer from this disadvantage is the acceleration of electrons in plasmas. Here, a laser pulse or a short electron bunch is directed into a plasma such that ambient electrons are accelerated directly by the laser pulse (DLA) or by the laser driven plasma wake field (PWFA).

Plasma waves that are driven by high intense and short pulses may break and build up field strengths that are many orders of magnitude larger than in conventional accelerators. If the laser pulse duration is shorter than half a plasma wave length, the plasma wave breaks after its first oscillation and a highly non-linear broken wave regime is reached. In this regime the laser pulse excites a plasma cavity without any electrons left. The shape of this cavity is spherical so the corresponding acceleration technique is also known as the bubble acceleration and the wake field is called the bubble. Electrons that are trapped in the bubble form a dense bunch that is accelerated to high energies (GeV and more) on a cm scale.

This thesis presents various analytical bubble models that treat individual problems. The first point is to present a new injection technique that describes the lateral injection of short electron bunches into the bubble. This method is suited to minimize the energy spread of the electron bunches. Secondly, radiation reaction for ultra-high electron energies in the GeV regime and above is included into the theory for the new injection method. The last point of this theses is to introduce a new model that calculates the background plasma density profile for given fields.



# *Danksagung*

An dieser Stelle möchte ich mich bei all denen bedanken, die mich während der Zeit meiner Promotion begleitet haben.

Zu aller erst möchte ich meinem Betreuer Herrn Prof. Dr. A. Pukhov für die großartige Möglichkeit danken, in seiner Arbeitsgruppe mit zu wirken und so die in dieser Dissertation vorgetragene Erkenntnisse gewinnen zu können. Ich danke ihm vor allem für seine Geduld, seine Leitung und seine Erfahrung, die er mit mir in den letzten Jahren geteilt hat.

Ich danke Herrn Prof. Dr. M. Büscher für die Übernahme des Korreferats meiner Arbeit und für die Möglichkeit, meinen Horizont außerhalb meines Fachbereichs zu erweitern.

Ein weiterer Dank geht an Herrn Prof. Dr. (i.R.) Karl-Heinz Spatschek und Herrn Prof. Dr. Dr. Carsten Müller für die vielen Diskussionen und dafür, dass ich teil ihres Instituts sein durfte. Des Weiteren danke ich Herrn Prof. Dr. O. Willi, dem SFB TR18 und dem GRK1203 für die langjährige finanzielle Unterstützung.

Was sind Formeln ohne verständliche Diagramme und Bilder? Was sind Programme ohne einen Computer, der - wenn es darauf ankommt - Tag und Nacht läuft? Was wäre ich ohne den jederzeit bereiten Herrn Evgenij Bleile? Vielen Dank an dieser Stelle für die technische Unterstützung. Eine genauso wichtige Art der Unterstützung habe ich von Frau Elvira Gröters erfahren, die sich immer mit voller Kraft für mich und meine Probleme eingesetzt hat. Danke dafür.

Meinen langjährigen Kollegen aus dem Institut: Tobias Tückmantel, Tongpu Yu, Naveen Kumar, Daniel an der Brügge, Götz Lehmann, Liangliang Ji, Oliver Jansen, John Farmer, Phuc Luu, Mykyta Charednycheck, Roberto Martorelli, Matthias Dellweg, Martin Jansen, Friedrich Schluck, Alexey Snyderikov, Ajit Upadhyay, Min Chen, Sebastian Münster möchte ich an dieser Stelle ebenfalls danken. Die aufmunternden und anregenden Gespräche, die konstruktiven Diskussionen und die hervorragende Arbeitsatmosphäre haben meine Zeit in diesem Institut viel kürzer erscheinen lassen, als sie es war.

Ohne die Unterstützung meine Eltern, Geschwister und Freunde wäre nicht nur meine Promotion, sondern auch mein gesamtes Studium in der Form nicht möglich gewesen. Ohne die Zeit, die Kosten, die Mühen, und die Nerven, die in mich investiert wurden, wäre ich heute nicht hier und diese Zeilen würden nicht geschrieben werden. Vielen Dank ihr Lieben - für alles.

Und zum Schluss: Liebe Maria, lieber Gabriel - euch gilt mein ganz besonderer Dank dafür, dass ihr in den letzten Tagen, Wochen, Monaten und Jahren so unendlich viel Geduld mit mir hattet und - egal wie es mir ging - immer an meiner Seite wart.

# Contents

<b>Erklärung</b>	<b>iii</b>
<b>Zusammenfassung</b>	<b>v</b>
<b>Abstract</b>	<b>vii</b>
<b>Danksagung</b>	<b>ix</b>
<b>Contents</b>	<b>xi</b>
<b>List of Figures</b>	<b>xiii</b>
<b>Physical Constants</b>	<b>xv</b>
<b>1 Introduction</b>	<b>1</b>
<b>2 Principles of classical and plasma based acceleration concepts</b>	<b>7</b>
2.1 Principles of conventional accelerators . . . . .	7
2.2 Plasma waves . . . . .	9
2.2.1 The ponderomotive force . . . . .	9
2.2.2 Linear plasma waves . . . . .	11
2.2.3 Nonlinear plasma waves . . . . .	12
2.2.4 Wave breaking . . . . .	13
2.3 Laser plasma accelerators . . . . .	14
2.3.1 The laser wake field accelerator . . . . .	14
2.3.2 The laser beat wave accelerator . . . . .	14
2.3.3 The self-modulated laser wake field accelerator . . . . .	15
2.3.4 Highly nonlinear laser wake field accelerator . . . . .	16
2.3.5 Acceleration limits and scaling laws . . . . .	18
2.4 Electron trapping and injection . . . . .	19
2.4.1 Beam loading and self-injection . . . . .	19
2.4.2 Ponderomotive injection . . . . .	21
2.4.3 Beat wave injection . . . . .	21
2.4.4 Ionization based injection . . . . .	22
2.4.5 Density transition injection . . . . .	22
<b>3 Side injection of short electron bunches into the bubble</b>	<b>23</b>
3.1 Introduction . . . . .	23
3.2 Bubble model and simulations . . . . .	24

3.3	Optimized side injection . . . . .	26
3.4	Analytical estimate of the cut off angle . . . . .	29
3.5	Conclusion . . . . .	34
<b>4</b>	<b>A radiation model for high electron energies in the GeV and TeV regime</b>	<b>35</b>
4.1	Introduction . . . . .	35
4.2	Relativistic radiation damping . . . . .	37
4.3	Optimized injection under consideration of radiation reaction . . . . .	42
4.4	Optimized side injection for ultra high energies and low intensities . . . . .	46
4.5	Optimized side injection for ultra high energies and high intensities . . . . .	49
4.6	Analytical estimate of radiated energy . . . . .	52
4.7	Conclusion . . . . .	55
<b>5</b>	<b>Deep plasma channels for tunable bubble fields</b>	<b>57</b>
5.1	Introduction . . . . .	57
5.2	Potentials and fields in a wake field in a plasma channel . . . . .	59
5.3	The $\delta$ -layer model . . . . .	60
5.3.1	The potentials in terms of the sources . . . . .	62
5.3.2	Calculate the electron sheath current . . . . .	65
5.3.3	Calculate the bubble fields from the sources and vice versa . . . . .	68
5.3.4	Summary for the $\delta$ -layer model . . . . .	72
5.4	The finite layer model . . . . .	73
5.4.1	The potentials in therm of the sources . . . . .	75
5.4.2	Calculate the electron sheath current . . . . .	78
5.4.3	Calculate the electron sheath current in the limit $\epsilon \rightarrow 0$ . . . . .	81
5.4.4	Calculate the fields from the sources and vice versa . . . . .	85
5.5	Important examples . . . . .	85
5.5.1	$\rho_{ion}(r) = \text{const}$ . . . . .	86
5.5.2	$\rho_{ion}(r) = \alpha r$ . . . . .	88
5.5.3	$\rho_{ion}(r) = \alpha r^2$ . . . . .	89
5.5.4	$\rho_{ion}(r) = 1 - \alpha \exp(-r^2/\sigma^2)$ . . . . .	90
5.6	Summary . . . . .	91
<b>6</b>	<b>Summary and prospect</b>	<b>93</b>
<b>A</b>	<b>Derivations in the quasi-static cylindrical approximation for chapter 5</b>	<b>97</b>
	<b>Bibliography</b>	<b>99</b>

# List of Figures

1.1	Wake field and bubble from 3D PIC simulations . . . . .	2
2.1	Linac and cyclotron . . . . .	8
2.2	Synchrotron and Livingston plot . . . . .	10
2.3	Laser wake field accelerator . . . . .	12
2.4	Plasma beat wave accelerator . . . . .	16
2.5	Electron bunch driven low out and laser pulse driven bubble . . . . .	17
2.6	Optical injection . . . . .	19
3.1	Side injected bunch in PIC simulations . . . . .	24
3.2	The injection angle . . . . .	26
3.3	The injection process . . . . .	27
3.4	The minimized energy spread . . . . .	28
3.5	Mean energy spread and amount of trapped electrons . . . . .	29
3.6	Maximal sum of trapped electrons vs laser energy and corresponding in- jection angle . . . . .	30
3.7	The guiding center approximation . . . . .	31
3.8	Amplitude approximation function and cut off angle . . . . .	32
4.1	Comparison of energy gain with and without radiation reaction effects. . .	36
4.2	QED parameter and field strength as seen by a test charge in the bubble .	39
4.3	Injection process with radiation reaction. . . . .	43
4.4	Maximum amount of trapped electrons after side injection with radiation reaction . . . . .	44
4.5	Maximum sum of trapped electrons and mean FWHM for low energies . .	45
4.6	Energy spectrum from a simulation with $E = 1$ MJ and $\lambda_{laser} = 1 \mu\text{m}$ . .	46
4.7	Number of trapped electrons vs incidence angle and maximal sum of trapped electrons vs laser energy for $E = 1$ MJ, $\lambda_{laser} = 1000$ nm, $a_0 = 4$	47
4.8	Maximum sum of trapped electrons and mean FWHM for $E = 1$ MJ, $\lambda_{laser} = 1000$ nm, and $a_0 = 4$ . . . . .	48
4.9	Number of trapped electrons vs incidence angle and maximal sum of trapped electrons vs laser energy for $E = 1$ MJ, $\lambda_{laser} = 1000$ nm, $a_0 = 64$	50
4.10	Maximal sum of trapped electrons and mean FWHM for $E = 1$ MJ, $\lambda_{laser} = 1000$ nm, and $a_0 = 64$ . . . . .	51
4.11	Comparison of energy gain with and without radiation reaction effects . .	54
5.1	Five zones model of the blow out . . . . .	62
5.2	Five zones model of the blow out with finite sheath thickness $\Delta$ . . . . .	75
5.3	Electron layer shapes . . . . .	86

---

5.4	Blow out shape for a homogeneous plasm. . . . .	87
5.5	Blow out shape for a linear plasma profile. . . . .	88
5.6	Blow out shape for a parabolic plasma profile. . . . .	89
5.7	Blow out shape for a Gaussian plasma profile. . . . .	90

# Physical Constants

Speed of Light	$c$	$=$	$2.997\,924\,58 \times 10^8 \text{ ms}^{-1}$
Electron Mass	$m_e$	$=$	$9.109\,382\,91(40) \times 10^{-31} \text{ kg}$
Elementary Charge	$e$	$=$	$1.602\,176\,565(35) \times 10^{-19} \text{ C}$ $= 4.803\,204\,51 \times 10^{-10} \sqrt{\text{g cm}^{-3}}/\text{s}$
Fine-structure constant	$\alpha$	$=$	$7.297\,352\,569\,8(25) \times 10^{-3}$
Planck constant	$h$	$=$	$6.626\,069\,57(29) \times 10^{-34} \text{ Js}$
Reduced Planck constant	$\hbar$	$=$	$1.054\,571\,726(47) \times 10^{-34} \text{ Js}$



# Chapter 1

## Introduction

Since their invention in the 1960s, lasers form the foundation of technological and scientific progress. Today - more than 50 years later available laser systems range from powerful industrial lasers to spectrally very narrow-banded continuous wave lasers for precise measurements of fundamental constants. At the end of the 1960s intensities in the range of  $10^{15}$  W/cm<sup>2</sup> could be produced. Since 1985 a further enhancement of the peak power could be reached with the chirped pulse amplification (CPA) [2] of laser pulses with durations in the pico- and femto-second regime. Today, the CPA method allows an easy generation of atto-second pulses with intensities in the bulk of  $10^{21}$  W/cm<sup>2</sup> [3, 4]. Next generation single shot laser systems that are build for fusion experiments reach  $10^{26}$  W/cm<sup>2</sup> [5]. Even higher intensities can be reached if such strong radiation interacts with plasma. Then it is supposed that non-linear laser-plasma interaction will provide a way to reach field intensities above  $10^{26}$  W/cm<sup>2</sup>. This would exceed the Schwinger-field and lead to pair creation, a prediction from QED theory [6].

One of the most important applications of such high intense laser pulses are laser-plasma accelerators [7–9]. They are considered as a new generation of electron accelerators because the accelerating electrical fields may be larger than 100 GV/m. This is more than three orders of magnitude larger than accelerating fields in conventional linear or circular accelerators. The key for the production of such high field strengths is to maintain high field gradients sufficiently long for particle acceleration. The corresponding effective acceleration time limits all other conventional accelerators. The functional principle of the laser-plasma accelerator is to trap electrons in the accelerating phase of a plasma wake field. The wake field in turn is produced by a relativistic laser pulse and can have a limited life time due to wave breaking. In Fig.(1.1a) a wake field (white border) is driven by high intense laser pulse (yellow area). The laser-plasma parameters are chosen such

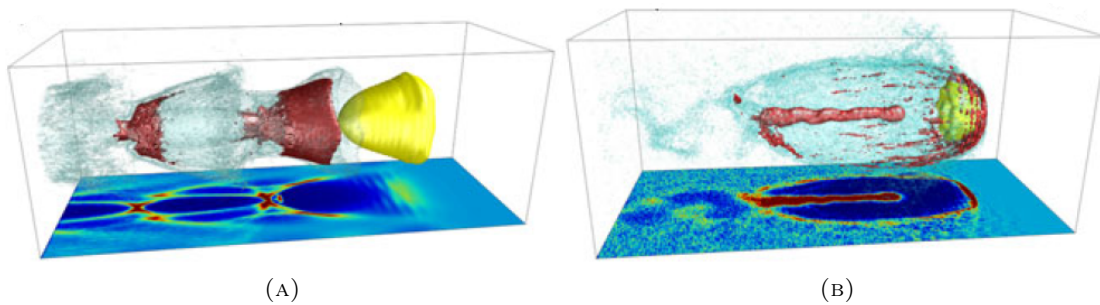


FIGURE 1.1: (a) Laser driven plasma wake field with trapped and accelerated electrons.  
 (b) Bubble with trapped electron bunch. Both pictures are taken from [1].

that the field does not break after its first oscillation. The red area shows the density of trapped electrons in the accelerating phase.

The stability of the wake-field is of central interest for the laser-plasma accelerator scheme because wave-breaking limits the effective acceleration time and thus the maximum achievable electron energy. An analytical description of the wave breaking mechanism of electrostatic plasma waves goes back to a paper from Dawson [7]. Here, plasma waves in the non-relativistic case in a homogeneous background plasma were studied. Furthermore, a critical threshold amplitude below which plasma oscillations are stable were found. When the oscillation amplitude is larger enough, a multi stream-flow sets in within the first oscillation and the wave breaks.

When the plasma wake field is driven to nonlinear amplitudes, it takes the form of an electronic cavity. The acceleration regime is called the "bubble regime" in the case that the wake field is driven by a short laser pulse [10]. If the driver is a dense highly energetic particle bunch the regime is called the "blowout regime" [11, 12]. For the laser driven case, the pulse is shorter than the plasma wavelength and fits perfectly into the first half of the plasma period. The laser intensity is high enough that the created wake field breaks after its first oscillation. In this regime, the wake field takes the form of a distorted spherical cavity from which all electrons are banished and that moves with nearly the speed of light through the plasma. In the following this wake-field is referred as "the bubble".

Inside the bubble, an accompanying electron bunch - the so called beam load - is accelerated until the spherical shape of the bubble breaks down or the electrons get out of phase with the wake. In Fig.(1.1b) the beam load (red bunch) is accelerated in the bubble. The driving laser pulse (yellow area right) is far at the front of the bubble. The life time of the bubble is limited by the energy exhaust of the driver which means that the sphere breaks as soon as the laser pulse has reached a characteristic depletion length [8, 13]. The fields inside the bubble can be calculated from Maxwell's equations for an empty sphere

[14] and a sphere that takes into account the field enhancement at the bubble back due to electron sheet crossing [15, 16]. An even simpler model for the fields inside the bubble has been proposed recently: a static piecewise model (PWM) [17]. This simplified model neglects any spatial or temporal field dependence, but due to its simplicity it is possible to calculate amplitude envelope functions to the transverse particle coordinates and momenta, and to analyze some self-injection physics analytically. In contrast to recent experiments, the PWM misses the prediction of mono energetic electron beams. Another method that modifies the PWM to a more general case but stay analytically treatable is a time dependent semi-piecewise model (tPWM)[18].

Another important point for the optimization of electron acceleration in laser plasma accelerators is the proper injection of electrons into the accelerating phase of the wake field. The physics of electron injection into a non-linear plasma wake, however, is very complex. The most common mechanisms to inject electrons are the beat wave mechanism, the gradient method, the ionization-based injection [19, 20], the transverse colliding laser injection method [21], self-injection of plasma background electrons, and injection of prior accelerated bunches. The modern theory of self-injection is still in early stage as it cannot predict quantitatively quantities observed in experiments, for example, the electron charge loaded in the bubble as function of laser-plasma parameters (plasma density, laser intensity, pulse duration and focal spot size) etc. At present there are many bubble models that treat self-injection physics and suggest their own criteria for electron trapping.

In this context some models suggests that plasma electrons are self-injected in the bubble when the normalized bubble radius is approximately larger than the Lorentz gamma-factor of the bubble rear [22, 23]. Other models suggest that electron self-injection occurs in the evolving bubble when the effective Hamiltonian becomes negative. This implies that the untrapped electrons cross the separatrix in the phase space, get into the 'bucket' and become trapped. In the recent advanced theories the effect of the plasma sheath surrounding bubble, the current distribution in the bubble sheath, and the driver effect is included [24]. Recently it was deduce from 3d numerical simulations that electron self-injection in a laser driven bubble happens when the amplitude of the normalized laser vector potential is approximately more than 3.8 [16].

The only fully-analytical models so far are the piecewise and semi-piecewise model from I. Kostyukov, E. Nerush, A. Pukhov, V. Seredov, and J. Thomas. They are based on a piecewise approximation of the bubble field in a time-independent model[17]. In a generalization the fields are time dependent, but piecewise constant in space. In this case the model is a sphere with an adiabatically growing radius  $R(t)$  and a growing trapping cross-section. A physical justification for this approach is that the interaction of the

electron bunch with the bubble border is taken into account. Since the fields remain constant in space the production of mono energetic electron beams is still missing [18]. A second generalization is to introduce a model that treats the right field gradient in the longitudinal direction. For this case energy spectra that are comparable to PIC simulations and a full gradient model are found. Simplifications in these models are that the interaction between the accelerated electrons and the laser pulse at the bubble front as well as the mutual electron interaction are neglected. The plasma ambient density is always continuous and constant. The motivation for all these assumptions are several observations in the phenomenological model of the bubble regime [14, 22].

Recent experiments in the bubble regime have shown that the production of ultra-cold and low emittance electron bunches is feasible. Normalized transverse emittance between 0.1 mm mrad and 1 mm mrad were realized, measured, and confirmed by numerical simulations [20, 21, 25]. The measurement of the bunch size is determined by an indirect method based on the measurement of the relativistic up shifted betatron x-ray radiation. The characteristics of the x-rays are related to the properties of the electron beam and the plasma wiggler [26]. To control the x-ray source it is necessary to characterize the electron bunch properties within the bubble. A spatial characterization of a laser-plasma based betatron source is used to estimate the transverse diameter of the electron bunch in the bubble. For the characterization both, the betatron oscillation amplitude of the electrons as well as the x-ray source size have to be determined. By measuring the betatron spectrum and comparing with theoretical prediction, the oscillation amplitude can be estimated. Furthermore, the traversal electron bunch size within the bubble is deduced from the x-ray source size and the betatron amplitude [27].

In this work the phenomenological model from [14, 22] is generalized by a new injection technique, the inclusion of radiation reaction effects, and model for the blow out regime that allows the calculation of plasma profiles for given fields inside the blow out. The new injection technique is based on the idea to suppress the self-injection. Then a dense electron bunch is injected from an external source. If the injection process is fast enough, the bunch is strongly localized in space and all electrons have the same longitudinal phase. This in turn leads to the generation of a high dense, ultra-cold electron bunch. The key in the external injection method is to inject the bunch at a certain angle that can be optimized so that more than 50% of the injected electrons are trapped and energy spread is minimized simultaneously.

For high laser energies this thesis also discusses radiation reaction (RR) effects on electron acceleration in the bubble model. Since the bubble fields are always weak enough to neglect QED effects like a recoil from quantized radiation, it is the electron energy that determines whether RR must be included or not. The electron energies that are discussed

in this frame work are fare beyond the GeV regime. It is also show that for MJ laser pulses the known scaling laws [28, 29] fail if RR is considered.

In the last part of this thesis the basis of the phenomenological bubble model is reviewed and all simplifications are reversed as far as possible. The first and most important simplification that is repealed is the model of the ambient plasma. In general the plasma density is homogeneous and constant. Now the driver runs in a deep plasma channel that is cylinder symmetric in propagation direction. Furthermore, the wake field radius depends on driver potential and the bunch potential. This is a significant change to the phenomenological model because a direct back action of the electron bunch on the bubble border was neglected so far. Since the driver field also determines the blow out shape, an indirect action of the driver on the accelerated bunch is included, too. The bubble sheath is modeled in two ways. First a delta layer with thickness zero is assumed so that the potentials and fields everywhere inside the cavity can be determined. For a study of any kind of injection mechanics the layer has a certain width  $\epsilon$ . In this second case the potentials are equal to the former case but the sheath now models the injection mechanics additionally.

The structure of this thesis is the following. In the next chapter a brief overview about current acceleration and injection techniques in the laser plasma accelerators is given. The following chapter discusses a new injection method that shows how prior accelerated electron bunches must be injected into a bubble to minimize the energy spread of the bunch load after acceleration. In this chapter the self-injection mechanism is suppressed. Chapter 4 also neglects the injection of background electrons and considers externally injected electron bunches. Different to the previous chapter, here the energy spread minimization at ultra high laser pulse energies in a new bubble model that includes radiation reaction effects is discussed. Chapter 5 introduces a blow out model that considers an electron sheath and its current, the mean field inside the accelerated electron bunch and a particular field inside the driver. The last chapter gives a summary of all conclusions and a short prospect of the possible further work in the field of bubble acceleration.



## Chapter 2

# Principles of classical and plasma based acceleration concepts

### 2.1 Principles of conventional accelerators

The most important tools for experiments in particles physics are particle accelerator. The working principle of all kinds of accelerators is that a particle with mass  $m$  and charge  $q$  passes an electric field  $\mathbf{E}$  that points in acceleration direction. Then the force

$$\mathbf{F} = q\mathbf{E} \tag{2.1}$$

accelerates the particle. If the velocity is small compared to the speed of light the force accelerates the charge according to Newton's second law  $\mathbf{F} = m\mathbf{a}$ . If the velocity is close to the speed of light,  $\mathbf{F} = d\mathbf{p}/dt$ , where  $\mathbf{p}$  is the particles momentum and  $\mathbf{p} = m\gamma\mathbf{v}$ . The Lorentz factor

$$\gamma = \sqrt{1 + \frac{|\mathbf{p}|^2}{m^2c^2}} \tag{2.2}$$

describes whether the particle is non-relativistic ( $\gamma \ll 1$ ), relativistic ( $\gamma \approx 1$ ), or ultra-relativistic ( $\gamma \gg 1$ ). The relativistic energy of a particle is

$$E = mc^2 + T = \gamma mc^2. \tag{2.3}$$

The kinetic energy  $T$  in the non-relativistic case is the classical expression  $T = m|\mathbf{v}|^2/2 = |\mathbf{p}|^2/(2m)$ . In the relativistic case  $T = (\gamma - 1)mc^2$  and in the ultra-relativistic case  $T \approx |\mathbf{p}|c$ . If a particle passes in parallel to a homogeneous, constant electric field  $\mathbf{E}$

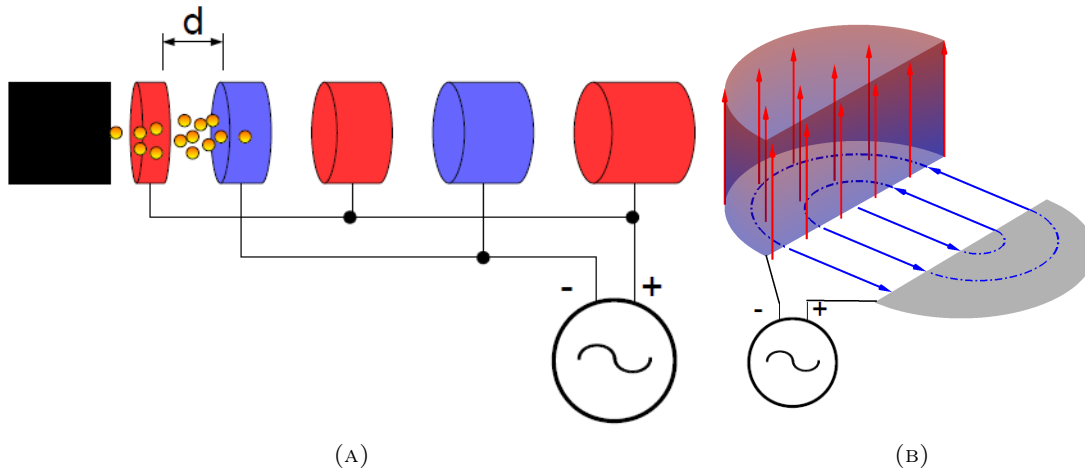


FIGURE 2.1: (a) Working principle of a linac. Charged particles (orange) are emitted from a source (black square) into an accelerating field between two tubes at distance  $d$ . The field is switched when the charges travel through the insulated tubes. (b) Schematic view of a cyclotron from top. The constant (blue) electrical field accelerates particles while the perpendicular (red) magnetic fields bends the trajectory (dotted line) to a circle.

along the distance  $d$  it gains the energy

$$W = q|\mathbf{E}|d. \quad (2.4)$$

As a consequence there are two possibilities to accelerate charged particles to relativistic and ultra-relativistic energies. The first method is to increase the field strength so that a higher accelerating force acts on the particle. The second method is to enlarge the acceleration distance  $d$ .

In a linear accelerator (see Fig.2.1a) charged particles are injected from a source into a series of homogeneous electrical fields. The fields are build up between Faraday tubes and accelerated the charges uniformly. When the particles are inside a tube the field changes its sign and the accelerating phase lies between the next two tubes so that the acceleration goes on. The total energy gain in this linear configuration is limited by the total length of the accelerator and the maximum applicable field strength. The limit for the field strength is material dependent and is usually in the order of  $E_{max} \approx 100$  MeV/m. If higher field strengths are applied, the accelerator material itself breaks which means that a short circuit between the tubes destroys the accelerating field.

Another idea to apply the linear acceleration in a more compact accelerator is the cyclotron (see Fig.2.1b). Here a constant magnet field  $B$  bends the trajectory of charged particle on a circle. On this circle the Lorentz force compensates the centrifugal force

and it is

$$F = \frac{m|\mathbf{v}|^2}{r} = q|\mathbf{v}|B \quad (2.5)$$

where  $r = |\mathbf{v}|/\omega$  is the gyroradius and  $\omega = qB/(\gamma m)$  is the cyclotron angular frequency. The acceleration of the particle is done every half cycle in a static electric field. The direction of the field is turned while the particle crosses the magnetic field. In the classical limit the accelerating field frequency is independent from the particle velocity and the path radius. In the relativistic case it is possible to adjust the magnetic field proportional to the Lorentz factor  $B = \gamma B_0$ . Then the frequency is constant again and the gyroradius  $r = m|\mathbf{v}|/(qB_0)$  depends on the velocity solely.

A further development of the cyclotron is the synchrotron (see Fig.2.2a). In this kind of accelerator the particle is accelerated in a uniform electrical field again. Different to the cyclotron a synchrotron has two kinds of magnetic fields exist. The first kind bends the particle trajectories. The second kind is important if a whole bunch of particles is accelerated as it focuses the bunch. The energies that can be achieved with synchrotron accelerators are only limited by the synchrotron radius. Today's largest synchrotron is the large hadron collider (LHC) in Geneva which is built for collision energies up to 14 TeV.

The development of hadron and electron-positron colliders in the last 50 years is shown in the Livingston plot in Fig.2.2b. Here the original graph produced by M.S. Livingston in 1954 is updated and shows how the maximal reachable laboratory energy of accelerated particle bunches increases with time. An important observation in this graph is that the energy of the accelerators increases exponentially in time. Starting from 1960s the energy has increased both in hadron and  $e^+e^-$ -colliders by a factor of 10 every 15 years.

All above explained acceleration methods use high frequency electric fields to accelerate particles while the maximum applicable field strength is limited by material break down. A completely different method is based on the idea that the particles stay in the accelerating phase of an electromagnetic wave. In the next sections an introduction to plasma waves and basic acceleration concept in plasmas is given.

## 2.2 Plasma waves

### 2.2.1 The ponderomotive force

In laser-driven plasma-based accelerators, plasma waves are driven by the ponderomotive force of a short laser pulse. This force can be derived from the equation of motion of a

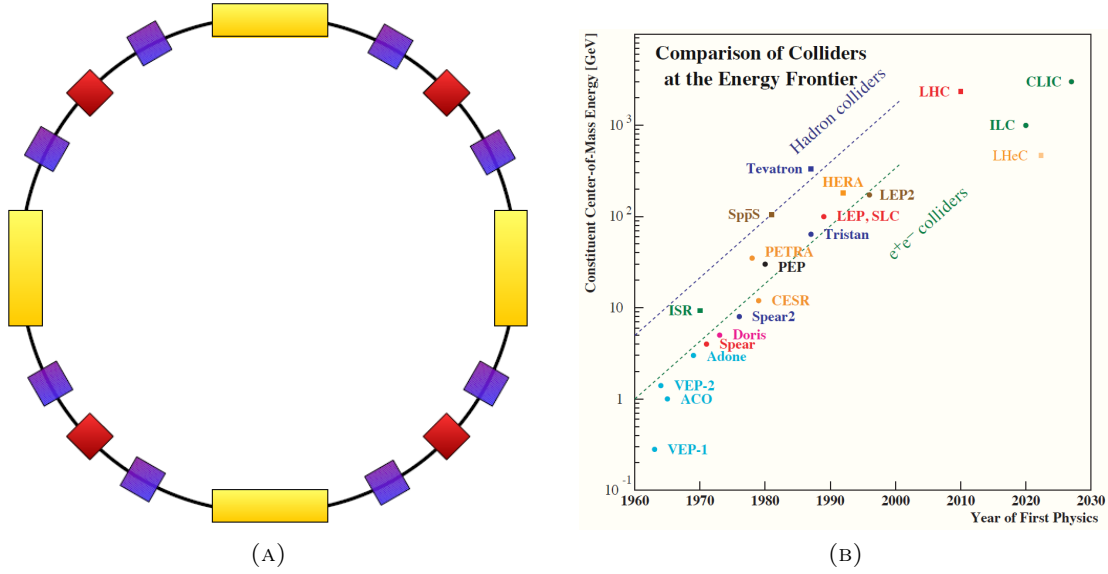


FIGURE 2.2: (a) Schematic view of a synchrotron with yellow accelerating part, red focusing part, and blue bending part. (b) Livingston plot. [30]

single point like particle with charge  $q$  and mass  $m$

$$\frac{d\mathbf{p}}{dt} = q \left( \mathbf{E} + \frac{\mathbf{p}}{mc} \times \mathbf{B} \right), \quad (2.6)$$

where  $\mathbf{E}$  and  $\mathbf{B}$  are the electric and magnetic field of the laser pulse. Since a laser pulse has a pure electromagnetic potential, it is  $\mathbf{E} = -\partial\mathbf{A}/\partial t$  and  $\mathbf{B} = \nabla \times \mathbf{A}$  where  $\mathbf{A} = A_0 \cos(\mathbf{k} \cdot \mathbf{r} - \omega t) \vec{e}_\perp$  is the laser potential. In the non-relativistic limit the normalized vector potential

$$\mathbf{a} = \frac{e\mathbf{A}}{mc^2} \quad (2.7)$$

is smaller than one and equal to the normalized transverse quiver momentum of a plasma electron in the laser field  $\mathbf{p}_q/(mc) = \mathbf{a}$ . The laser strength parameter  $a_0$  is the peak amplitude of  $\mathbf{a}$ . It is related to the peak laser intensity  $I_0$  and the laser power  $P$  via

$$I_0 = \pi c \left( \frac{a_0 m_e c^2}{c \lambda_{laser}} \right)^2, \quad P = \pi r_0^2 I^2, \quad (2.8)$$

where  $r_0$  is the laser focal spot size and  $\lambda_{laser} = 2\pi/k$  is the wave length of a laser with frequency  $\omega_0 = 2\pi c/\lambda_{laser}$

If the momentum of an electron is split up according to  $\mathbf{p} = \mathbf{p}_q + \delta\mathbf{p}$  the second order motion gives the 3D ponderomotive force in the non-relativistic limit [31]

$$\mathbf{F}_p = \frac{d\delta\mathbf{p}}{dt} \approx -m_e [(\mathbf{p}_q/m_e \cdot \nabla) \mathbf{p}_q/m_e + c \mathbf{p}_q/m_e \times (\nabla \times \mathbf{a})] = -\frac{1}{2} m_e c^2 \nabla a^2. \quad (2.9)$$

Here it was used that  $\mathbf{v}_q \approx \mathbf{p}_q/m_e$ ,  $\partial\mathbf{p}_q/\partial t \approx -e\mathbf{E}$ , and  $\gamma \equiv 1$ . In the nonlinear regime the leading order transverse motion of an electron is still the quiver motion if  $r_0 > \lambda_p \gg \lambda_{laser}$ , where  $\lambda_p = 2\pi c/\omega_p$  is the plasma wave length and  $\omega_p = (4\pi n_0 e^2/m_e)^{1/2}$  is the electron plasma frequency in a homogeneous background plasma with density  $n_0$ . The gamma factor of the electron can be expressed in terms of the laser amplitude and the electrostatic wake field potential  $\Psi$  if the energy is averaged over the fast laser period [32, 33]

$$\gamma = \frac{1 + \bar{\mathbf{v}}_{\perp}^2/c^2 + \bar{\mathbf{a}}_{\perp}^2 + (1 + \bar{\Psi})^2}{2(1 + \bar{\Psi})}. \quad (2.10)$$

In a quasi-static approximation that assumes that the laser envelope only depends on the distance to the propagation axis  $r$  and  $\xi = z - ct$  the wake field potential  $\Psi$  can be expressed in terms of the electrostatic potential  $\varphi$  and  $\mathbf{a}$  via  $\Psi = \varphi - a_{\parallel}$  and the effective nonlinear ponderomotive force is

$$\mathbf{F}_{p,rel} = -m_e c^2 \nabla \gamma. \quad (2.11)$$

### 2.2.2 Linear plasma waves

In the non-relativistic limit ( $a_0 \ll 1$ ) a laser pulse excites a linear plasma density perturbation that can be described by the normalized density perturbation  $\delta n/n_0$  and the wake field potential via

$$\left(\frac{\partial^2}{\partial t^2} + \omega_p^2\right) \frac{\delta n}{n_0} = \frac{1}{2} c^2 \nabla^2 \mathbf{a}^2, \quad \left(\frac{\partial^2}{\partial t^2} + \omega_p^2\right) \Psi = \frac{1}{2} \omega_p^2 \mathbf{a}^2. \quad (2.12)$$

If  $\delta n = n - n_0 \ll n_0$  and  $|\mathbf{E}| \ll m_e c \omega_p / e$  Eqs.(2.12) describe sinusoidal plasma waves with frequency  $\omega_p$  so that

$$\frac{\delta n}{n_0} = \frac{c^2}{2\omega_p} \int_0^t \sin(\omega_p(t-t')) \nabla^2 \mathbf{a}^2(\mathbf{r}, t') dt', \quad (2.13)$$

$$\frac{\mathbf{E}}{E_0} = -\frac{c}{2} \int_0^t \sin(\omega_p(t-t')) \nabla \mathbf{a}^2(\mathbf{r}, t') dt'. \quad (2.14)$$

These solutions indicate that the radial extend of the plasma wave is in the order of the laser focal spot size and that the wave is excited effectively if the laser envelope scale length is in the order of the plasma wave length. The cold non-relativistic wave breaking field [7]

$$E_0 = \frac{m_e c \omega_p}{e} \propto \sqrt{n_0} \quad (2.15)$$

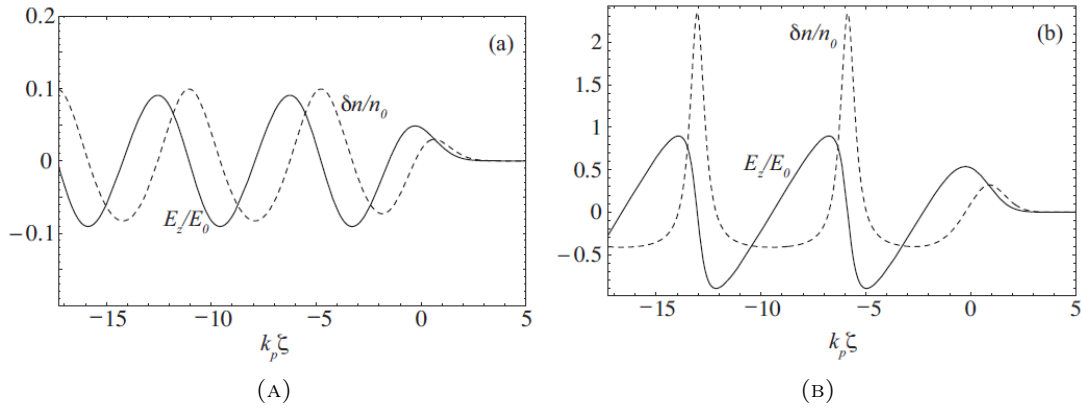


FIGURE 2.3: Time averaged density variation  $\delta n/n_0$  (dashed curve) and axial electric field  $E_z/E_0$  (solid line) in a LWFA for (a)  $a_0 = 0.5$  and (b)  $a_0 = 2$ . [34]

is a limit for the electrical field in linear plasma waves. It can be estimated from the Poisson equation  $\nabla \mathbf{E} = 4\pi e(n_0 - n_e)$  and the idea that all plasma electrons are oscillating with frequency  $\omega_p$  since then  $(\omega_p/c)E_{max} = 4\pi en_0$ . The cold non-relativistic wave breaking field gives a first estimate of how large the accelerating fields in a laser plasma accelerator can be. For example, if the plasma density is in the order of  $n_0 \approx 10^{18} \text{ cm}^{-3}$ , the wave breaking field is  $E_0 \approx 100 \text{ GV/m}$ .

As Fig.2.3a shows, the plasma wave, also called wake field, is a sinusoidal plasma density perturbation with constant phase and amplitude at a certain distance from the driving laser pulse. The key for the laser plasma acceleration now is to inject electrons into the accelerating phase of the wake field and to extract them before they reach the decelerating phase.

### 2.2.3 Nonlinear plasma waves

In the relativistic  $a_0 > 1$ , or non-linear limit  $|\mathbf{E}| > E_0$  the plasma wave becomes highly non-linear, i.e. the wave steepens and its wave length increases as Fig.2.3b illustrates. Now the wake field potential oscillates between a minimum and a maximum which are related to the amplitude of the axial electric field via

$$-E_{max} \leq E_z \leq E_{max}, \quad (2.16)$$

$$\Psi_{min} = \frac{E_{max}^2}{2E_0^2} - \frac{v_p}{c} \sqrt{\left(1 + \frac{E_{max}^2}{2E_0^2}\right)^2 - 1}, \quad (2.17)$$

$$\Psi_{max} = \frac{E_{max}^2}{2E_0^2} + \frac{v_p}{c} \sqrt{\left(1 + \frac{E_{max}^2}{2E_0^2}\right)^2 - 1}, \quad (2.18)$$

where,  $v_p \leq c$  is the phase velocity of the plasma wave. The form of the electric field exhibits a characteristic sawtooth profile that indicates the wave steepening while the density perturbations become highly peaked. The lengthening of the plasma wave length can be described by [35, 36]

$$\lambda_{p,rel} = \begin{cases} \lambda_p \left( 1 + 3 \frac{E_{max}^2}{16E_0^2} \right), & \frac{E_{max}}{E_0} \ll 1 \\ \frac{2\lambda_p}{\pi} \left( \frac{E_{max}}{E_0} + \frac{E_0}{E_{max}} \right), & \frac{E_{max}}{E_0} \gg 1. \end{cases} \quad (2.19)$$

This increase of the wave length with increasing wave amplitude has an important effect on nonlinear 2D and 3D plasma waves because it explains a basic mechanism for wave breaking. The reason why the new amplitude dependence can lead to wave breaking is that the plasma wave amplitude is maximum on the  $z$ -axis and decreasing radially. Thus  $\lambda_{p,rel}$  is a function on the laser focal radius which leads to a bending of the wave fronts. If the curvature is too strong the wave breaks radially.

#### 2.2.4 Wave breaking

The cold non-relativistic wave breaking field in the linear regime must be corrected for stronger fields ( $E_{max} > E_0$ ) and larger laser pulse amplitudes ( $a_0 > 1$ ). This is usually done by using the nonlinear, relativistic, cold fluid equations in one dimension. In the limit  $\gamma_p = (1 - v_p^2/c^2)^{-1/2} \approx \omega_{laser}/\omega_p \gg 1$  they are [35]

$$\frac{n}{n_0} = \frac{\gamma_{\perp}^2 + (1 + \Psi)^2}{2(1 + \Psi)^2}, \quad \frac{v_z}{c} = \frac{\gamma_{\perp}^2 - (1 + \Psi)^2}{2(1 + \Psi)}, \quad \gamma = \frac{\gamma_{\perp}^2 + (1 + \Psi)^2}{2(1 + \Psi)}, \quad (2.20)$$

where  $\gamma_{\perp} = 1 + \mathbf{a}^2$  and  $\mathbf{a} = \mathbf{v}_{\perp}/c$ . The cold relativistic wave breaking field that is related to these non-linear equations is [37]

$$E_{0,rel} = \sqrt{2\gamma_p - 2}E_0. \quad (2.21)$$

If the electric field amplitude now approaches the wave breaking limit, the minimum wake field [cmp. Eq.(2.17)] becomes

$$\Psi_{min} = \gamma_p - 1 - \sqrt{1 - \frac{1}{\gamma_p^2}} \sqrt{\gamma_p^2 - 1} = \frac{1}{\gamma_p} - 1 \quad (2.22)$$

and the cold plasma density diverges. The cold fluid equations can be applied as long as electron fluid velocity  $v_e$  is less than the wake field phase velocity. In the calculation above, however,  $v_e \rightarrow v_p$ , so the wave is said to "break" if  $v_e \approx v_p$  and the density becomes singular.

General expressions for the maximum field amplitude in three dimensions are not known yet. However, full relativistic particle in cell simulations indicated first that after the nonlinear wake field regime an even more promising acceleration regime exists [10, 38]. In this highly nonlinear regime the plasma wave is broken after the first oscillation and the shape of the electron density is a sphere from which all electrons are dispelled (see Fig.2.5b).

The next sections discuss how these wake fields can be excited and how electrons can be injected into the accelerating phase of the fields.

## 2.3 Laser plasma accelerators

### 2.3.1 The laser wake field accelerator

In the laser wake field acceleration (LWFA) a short ( $\tau < 1$  ps), high intense ( $I_0 > 10^{17}$  W/cm<sup>2</sup>) laser pulse drives a wake field in an under dense plasma ( $\lambda_{laser}/\lambda_p \ll 1$ ) in the linear or nonlinear regime. The plasma wave is excited most efficiently if the pulse length  $L = c\tau$  is in the order of the plasma wave length. A first demonstration of the LWFA was possible with the invention of the chirped pulse amplification (CPA) [2] while the nonlinear theory in one dimension was developed. In the linear wake field regime ( $a_0 < 1$ ) the optimal pulse length conditions in terms of the full width at half maximum (FWHM) for square, sine, and Gaussian pulse profiles are  $L_{FWHM} = 0.5\lambda_p$ ,  $L_{FWHM} = 0.42\lambda_p$ , and  $L_{FWHM} = 0.37\lambda_p$  respectively. The maximum electrical fields at these optimized scalings are  $E_{max} = a_0^2 E_0$  for square pulses,  $E_{max} = 0.82a_0^2 E_0$  for sine pulses, and  $E_{max} = 0.76a_0^2 E_0$  for Gaussian pulses. [39]. First experiments that could achieve accelerating gradients in the order of 100 GeV/m were realized at the turn of the millennium [40, 41]. Today, electron bunches that are accelerated in the LWFA regime have durations in the order of femto-seconds as the driving laser pulses have durations in the same order.

In the nonlinear regime the laser wake field acceleration is dominantly performed in the highly nonlinear regime where the wake field breaks after a view oscillations or shortly after the driver. Thus this kind of acceleration has its own subsection in 2.3.4.

### 2.3.2 The laser beat wave accelerator

If long  $L \gg \lambda_p$  laser pulses are shot into a plasma no wake field is excited. However, if two long laser pulses with frequencies  $\omega_1$  and  $\omega_2$  are shot into an underdense plasma

and if the frequencies satisfy the resonance condition  $\omega_1 - \omega_2 \approx \omega_p$ , a wake field is driven resonantly. The method of properly adjusting the two frequencies is called the plasma beat wave acceleration (PBWA) and excites the plasma wave similar to the laser wake field acceleration. Here, however, the ponderomotive force is a nonlinear combination of the ponderomotive forces each laser pulse involves. In the non-relativistic regime the total force is  $F_p \propto \nabla \mathbf{a}^2$ , where  $|\mathbf{a}| = a_1 \cos(k_1 z - \omega_1 t) + a_2 \cos(k_2 z - \omega_2 t)$  and the beat term  $a_1 a_2 \cos((k_1 - k_2)z - \Delta\omega t)$  can resonantly drive a plasma wave with wake field potential  $\Psi = a_1 a_2 k_p \xi \sin((k_1 - k_2)z - \Delta\omega t)/4$  at distance  $\xi = z - ct$  from the front of the laser pulse. Simplified, the laser beat wave can be described as a series of laser pulses each with amplitude  $a_1 a_2$  and duration  $2\pi/\Delta\omega$ .

In the nonlinear regime the plasma wave length increases with increasing wave amplitude. Thus the wake field will become out of phase with the laser beat wave so that the maximum plasma wave amplitude is limited. The growth of the plasma wave stops as soon as the difference between the laser beat wave and the plasma wave is  $\pi/2$  which gives a characteristic saturation distance after the laser pulse front and a maximum wake field amplitude of  $\Psi_{max} = (2\pi a_1 a_2)^{1/3}$  [42]. If the beat frequency is slightly detuned ( $\Delta\omega < \omega_p$ ) it is possible to maximize the plasma wave amplitude at an optimal detuning. This principle is illustrated in Fig.2.4. Here a laser beat wave consists of four beat periods generated by four laser pulses. In Fig.2.4a the detuning is not considered and  $\Delta\omega = \omega_p$ . The wake field amplitude saturates after the second beat wave but is driven down by the third and fourth shortly after. The net wake field excitation after the four beat waves is nothing more but a very small density perturbation. However, if the beat period is optimized the wake field is driven to nonlinear amplitudes and the wake steepening in Fig.2.4b matches the sawtooth form already discussed in the nonlinear plasma wave section.

First experiments that report about plasma wave excitation in the PBWA regime were done in 1985[43]. Later electrons from the plasma back ground could be accelerated by beat wave driven wake fields. Since prior to 1985 the generation of short laser pulses was not possible, the principle of LBWA was the only realistic method to accelerate electrons in a plasma wake field.

### 2.3.3 The self-modulated laser wake field accelerator

Another acceleration method that uses long laser pulses to drive plasma wake fields is the self-modulated laser wake field acceleration (SMLWFA). Here, a single long pulse breaks up into many short pulses due to enhanced focusing and diffraction in different regions of the plasma wave. Each laser pulse fragment has a width in the order of the plasma wave

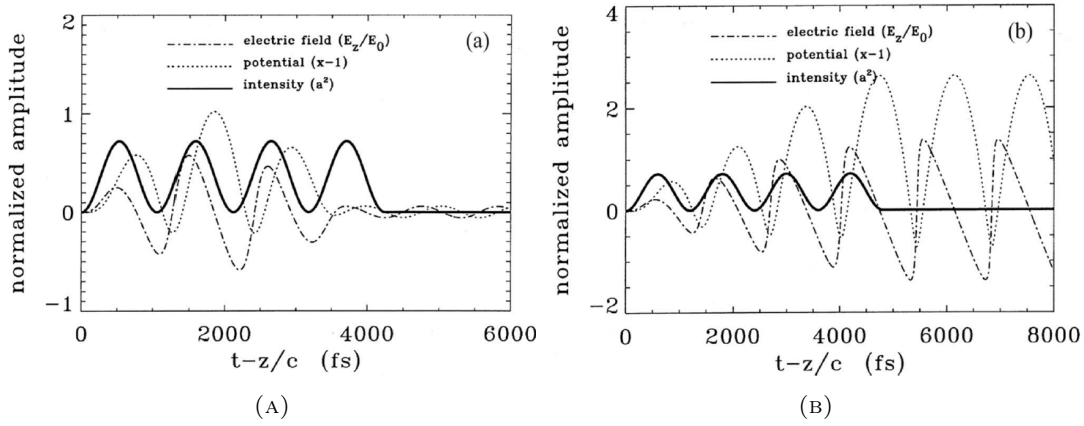


FIGURE 2.4: (a) PBWA example with four beat pulses without optimization showing the effect of detuning. (b) PBWA example with four beat pulses with optimization  $\Delta\omega < \omega_p$ . [44]

length  $L \approx \lambda_p$ . This self-modulation process has a couple of advantages over the short pulse driven LWFA regime. First, the SMWFA regime does not need matching condition like  $L \approx \lambda_p$  or a special laser pulse tailoring. Second, the acceleration is enhanced because (i) the SMWFA regime operates at higher densities, (ii) the laser pulse tends to focus to higher intensities, (iii) the wake field is resonantly excited by a couple of laser pulses, and (iv) relativistic optical guiding extends the acceleration distance to several Rayleigh lengths. Experiments with laser pulses in the range of picoseconds showed that trapped electrons from background plasma could be accelerated up to more than 40 MeV while an estimate of the electron dephasing length indicated that the field strength in acceleration direction must be at least 100 GeV/m [45].

### 2.3.4 Highly nonlinear laser wake field accelerator

If a wake field is driven to the nonlinear regime the electron density profile exhibits deviations from the sinusoidal form that is known as an analytical solution to the linear regime. In three dimensions a completely new shape is formed if the wake field breaks or - equivalently - if the driver pushes all electrons from the axis. Then a cavity develops right after the driver and moves with nearly speed of light through the plasma. If the driver is a short electron bunch, the cavity is referred to as the "blow out", while a short and high intense laser pulse usually excites a so called "bubble" [10]. Both regimes are characterized by an accelerating field that depends only on the distance to the driver and a focusing field that is linear in the distance to the propagation axis. The fields in cylindrical coordinates in the quasi-static approximation  $\xi = r_{||} - ct$  are [14, 46]

$$E_{||} \approx \frac{1}{2}k_p\xi E_0, \quad E_{\perp} = \frac{1}{4}k_p r E_0, \quad B_{\varphi} = -\frac{1}{4}k_p r E_0. \quad (2.23)$$

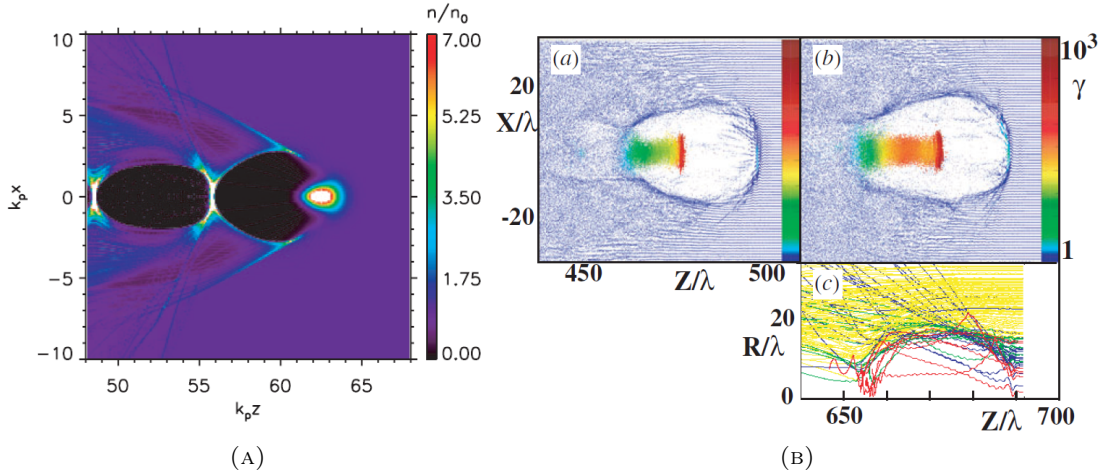


FIGURE 2.5: (a) Blow out driven by an electron beam with energy 0.5 GeV [34]. (b) Bubble driven by a laser pulse with energy 12 J and duration 33 fs [48].

As a consequence the radial focusing force  $F_{\perp} = E_{\perp} - B_{\varphi}$  on a trapped electron is as large as the forward accelerating force and both are equal to the radial space charge force in a long ion channel [11].

An example for the blow out regime is shown in Fig.2.5a. Here a Gaussian electron bunch with density  $n_b = 5n_0$  and energy  $\epsilon = 0.5$  GeV drives a cavity with radius  $k_p r_b \approx 3$ . Experiments in the blow out regime have demonstrated the generation of 40 GeV electron bunches and simultaneously showed that the energy of the driving bunch was lowered as a certain amount of energy is needed to drive the wake field [47].

To drive a wake field in the bubble regime, a high intense ( $a_0 \gg 1$ ) laser pulse that satisfies  $\sqrt{a_0} \geq r_0 k_p / 2$  is shot into an under-dense plasma. An example of a bubble is shown in Fig.2.5b. Here, a laser pulse with  $a_0 = 5$ ,  $r_0 = 9 \mu\text{m}$ , and  $\lambda_{laser} = 800$  nm excites an almost spherical bubble with radius  $k_p r_b = 3$ . If electrons are trapped in the bubble the wake field associated with the trapped bunch can lead to beam loading effects and thus to an elongation of the bubble. Theoretical models for the bubble regime include a similarity theory that describes the wake field by the similarity parameter [49]

$$S = \frac{n_0}{a_0 n_{cr}} \quad (2.24)$$

where  $n_{cr} = m_e \omega_{laser} / (4\pi e^2)$  is the critical density. The S parameter allows to distinguish between relativistically overdense ( $S \gg 1$ ) and underdense ( $S \ll 1$ ) plasmas. The optimal laser plasma parameters to drive a bubble are  $k_p a_0 \approx \sqrt{a_0}$ ,  $L = c\tau \leq r_0$ , and  $P(\text{GW}) > 30[\tau(\text{fs})/\lambda_{laser}(\mu\text{m})]^2$ . Since most laser systems use wave lengths in the range

of 300 nm to 1.2  $\mu\text{m}$ , the critical density is always in the range of  $10^{21} \text{cm}^{-3}$  because

$$n_{cr}[\text{cm}^{-3}] = \frac{\pi m_e c^2}{e^2} \frac{1}{\lambda_{laser}^2} = \frac{1.127 \times 10^{21}}{\lambda_{laser}^2[\mu\text{m}]}.$$
 (2.25)

### 2.3.5 Acceleration limits and scaling laws

An estimate of the energy an electron bunch may reach after acceleration in the bubble regime is

$$W \approx 0.22 m_e c^2 \frac{c\tau}{\lambda_{laser}} \sqrt{P(\text{GW})}.$$
 (2.26)

The acceleration length the bunch needs to travel before it reaches this energy is  $L_{acc} \approx 0.7 c\tau Z_R / \lambda_{laser}$ . In general, however, there are many mechanisms in the laser plasma interaction that limit the energy gain in a laser plasma accelerator. The most important are laser diffraction (for laser driven plasma waves), pump depletion, and dephasing.

The laser diffraction is the natural laser pulse broadening within a few Rayleigh lengths. It limits the acceleration because at some point a broadened pulse loses the ability to drive a wake field. A successful countermeasure that prevents the laser pulse diffraction is optical guiding such as a preformed plasma channel. In the highly nonlinear regime, this measure is not necessary because high intense, ultra short laser pulses usually experience self focusing effects.

The pump depletion is a limiting factor that cannot be avoided by some optical guiding since it describes the energy transfer from the driver to the wake field and the accelerated electron bunch. The pump depletion length  $L_{dp}$  is the absolute limit of the acceleration distance. It can be estimated by considering that the whole energy from the driver is converted to wake field energy. Consequently, in case of a laser driver with field  $E_L$  it is

$$L_{dp} \approx c\tau \frac{E_L^2}{E_z^2}.$$
 (2.27)

In the nonlinear regime depletion is the dominant effect that limits the energy gain. In the linear regime, however, the depletion length is long enough to allow accelerated electrons to outrun the accelerating phase of the wake field. Thus, in the non-relativistic case the limiting factor is the dephasing length  $L_d$  that determines how much energy a trapped electron may gain in a plasma wake field accelerator. An estimate of the dephasing length in the linear limit is

$$L_d = \frac{\lambda_p}{2(1 - v_p/c)} \approx \gamma_p^2 \lambda_p$$
 (2.28)

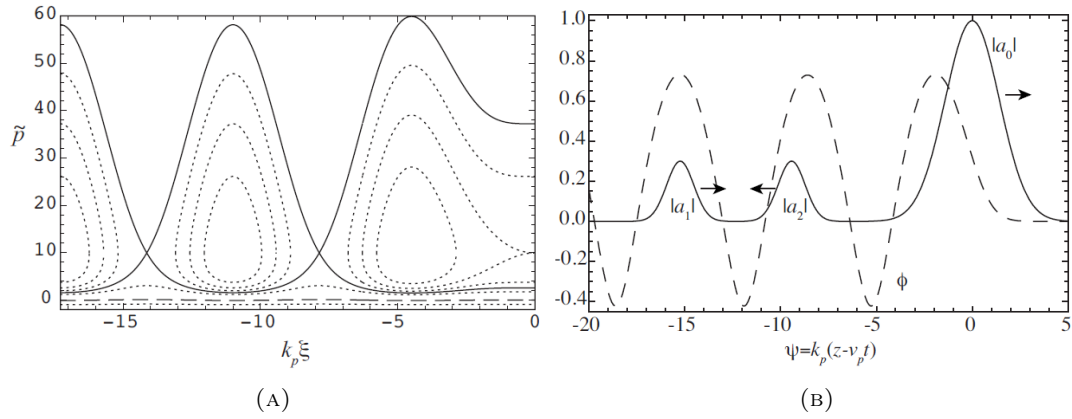


FIGURE 2.6: (a) Single particle orbits in phase space for an electron in a small amplitude sinusoidal plasma wave. The solid curve is the separatrix. The dashed curves are cold fluid orbits. [34] (b) Profiles of the pump laser  $a_0$ , the wake  $\Psi$  (dashed curve), the forward injection pulse  $a_1$ , and the backward injection pulse  $a_2$ . In the  $\Psi = k_p(z - v_p t)$  frame  $a_0$ ,  $a_1$ , and  $\Psi$  are stationary while  $a_2$  moves with velocity  $\approx 2c$  to the left. [34, 50]

where  $\gamma_p$  is the gamma factor related to the phase velocity  $v_p$  of the wake field.

## 2.4 Electron trapping and injection

### 2.4.1 Beam loading and self-injection

To decide whether an injected electron is trapped in a wake field it is reasonable to analyze its trajectory in phase space where trapped particles move on closed orbits. An example from a 1D linear model is shown in Fig.2.6a. Here single particle orbits are dotted curves within a separatrix (solid line). The orbits of electrons in the cold fluid are dashed. In this linear regime the wake field is described by the sinusoidal electrostatic potential  $\Psi = \Psi_0 \cos(k_p \xi)$  with  $\Psi_0 = E_{max}/E_0$ . So the phase region  $-\pi < k_p \xi < 0$  is accelerating and an electron that is injected at  $\xi = 0$  with  $v_{||} < v_p$  first moves further into the accelerating region. If the electron has an initially sufficient large velocity it will be faster than the wake field  $v_{||} > v_p$  at some point and performs closed orbits in the  $-\pi < k_p \xi < \pi$  range. Since the energy of the electron is conserved in the plasma wave, it will never leave the orbit and is trapped. If the initial velocity of the electron is too small, it slips out of the wake at  $k_p \xi = -\pi$  and continues slipping backward in the plasma wave. This behavior is related to untrapped electrons. The separatrix separates regions of trapped and untrapped orbits in phase space.

A more mathematical description of electron trapping in a wake field is possible with the Hamiltonian of a single electron in a laser pulse generated plasma wave

$$H = \gamma - \frac{v_p}{c} \tilde{p} - \Psi, \quad (2.29)$$

where  $\tilde{p}$  is the normalized momentum of the electron. Since in most quasi-static models the electron energy is a constant of motion the minimum initial electron momentum can be calculated from  $H_0 = \gamma_0 - \frac{v_p}{c} \tilde{p}_0 = H_s$  and [51]

$$\tilde{p}_0 = \gamma_p \frac{v_p}{c} (\gamma_{\perp} - \gamma_p \Psi_{min}) - \gamma_p \sqrt{(\gamma_{\perp} - \gamma_p \Psi_{min})^2 - 1}. \quad (2.30)$$

Here  $H_s$  is the Hamiltonian that describes the orbit in phase space which lies on the separatrix.

When the driver propagates through the plasma more electrons get trapped and a dark current in the plasma wave builds up. If beam loading is neglected, i.e. if the wake field produced by the trapped electrons is much smaller than the confining field, a first estimate suggests that charges in the bulk of nC can be trapped. However, if the wake field amplitude is substantially reduced due to beam loading the charge limit is the number of accelerated electrons that necessary to produce a wake field which cancels the accelerating field [52].

At present there are many bubble models that treat self-injection physics and suggest their own criteria for electron trapping. In this context the KNPS model [I. Kostyukov et al., Phys. Rev. Lett. 103, 175003 (2009) [22]] suggests that plasma electrons are self-injected in the bubble when the normalized bubble radius is approximately more than Lorentz gamma-factor of the bubble rear. The same criterion has been derived in the framework of the CSV model by S. Corde, A. Stordeur, and V. Malka [23]. A modification of this criterion has been proposed in a model by A. G. R. Thomas [53, 54]. However, this modification has been seriously criticized in the Comment of S. Corde et al. [23]. The KYKS models by S. Kalmykov, S. Yi, V. Khudik, and G. Shvets [55–57] suggest that electron self-injection occurs in the evolving bubble when the effective Hamiltonian becomes negative. This implies that the untrapped electrons cross the separatrix in the phase space, get into the 'bucket' and become trapped. In the recent advanced version of the KYKS models the effect of the plasma sheath surrounding bubble, the current distribution in the bubble sheath, and of the driver effect is included [24]. W. Lu et al. have deduced from PIC simulations a simple criterion that electron self-injection in a laser driven bubble happens when the amplitude of the normalized laser vector potential is approximately more than 3.8 [16]. In more recent papers the trapping condition is expressed through a wake pseudo-potential [58, 59].

### 2.4.2 Ponderomotive injection

If a small energy spread electron bunch is injected into the accelerating phase of a laser wake field the bunch can be accelerated to high energies while the energy spread is conserved. To achieve this it is necessary that the bunch length is in the order of the plasma wave length, i.e. in the  $\mu\text{m}$  range. To trigger the injection ultra-short high intense laser pulses can be used. A first realization of this idea included two laser pulses propagating perpendicular to another. Here, the first pulse drives the wake field while the second pulse intersects the wake at a certain distance to the driver. The ponderomotive force of the injecting pulse then accelerates a fraction of the plasma electrons in the wake so that they become trapped. The key role of the injecting pulse is to change the momenta of the electrons sufficiently so that they cross the separatrix of the wake field. Today this injection method is used to gain additional control on the electron bunch emittance during the injection process [21].

### 2.4.3 Beat wave injection

In the ponderomotive injection it is the time-averaged intensity gradient that pushes the electrons into the separatrix of the wake field. In contrast to that the beat wave injection uses the ponderomotive force associated with the slow beat wave of two intersecting pulses [50]. Fig.2.6b illustrates this idea. Here, three short laser pulses are used to drive the wake field (done by the pump pulse with intensity  $a_0 \approx 1$ ) and to drive a beat wave for injection. The beat wave is generated by a forward going pulse  $a_1$  and a backward going pulse  $a_2$  which are both orthogonally polarized to avoid interaction with the driver. The injection pulse frequencies are adjusted so that  $\omega_1 - \omega_2 = \Delta\omega \gg \omega_p$ . The forward running injection pulse is as fast as the driver and travels at a fixed distance that controls the point of injection into the wake field. When the injection pulses collide a slow ponderomotive beat wave is generated and during the overlapping time a two-stage accelerating process can occur. In this process the beat wave traps and heats background plasma electrons and thus can inject them into the separatrix of the wake field.

Advantages of the beat wave injection method are a detailed control of (i) the injection phase via the position of the forward injection pulse, (ii) the beat wave velocity via  $\Delta\omega$ , (iii) the injection energy via  $a_1$  and  $a_2$ , and (iv) the number of injected electrons via the backward injection pulse duration. Another setup for the beat wave injection is to use only two laser pulses that are equally polarized. Then the tail of the pump laser pulse is used to beat the second, counter propagating laser pulse [60].

#### 2.4.4 Ionization based injection

Another idea to inject electrons from the plasma background into the accelerating phase of a plasma wake field is to use a second laser pulse that further ionizes the plasma so that the newly released electrons can be trapped. This kind of injection requires high Z plasmas and was first proposed in [61]. A few years later a realization of the ionization based injection showed the injection of a few 100 keV electrons from a low pressure Kr gas [62]. Today the ionization-induced injection method is also applicable to the highly nonlinear regime [19].

#### 2.4.5 Density transition injection

To inject electrons into the accelerating phase of a wake field a decreasing plasma density ramp that is either long compared to the plasma wave length [63] or sharp and short [64] can be used. The basic mechanism that injects electrons and leads to trapping is a change of the wake field phase velocity  $v_p$  due to the density change. In general trapping will occur as soon as the local phase velocity of the wake field on the density ramp equals the fluid velocity of the electrons. A stable experimental method to generate negative density gradients has been demonstrated by focusing a laser on the downstream edge of a gas jet [65].

Results from this chapter are/will be published in the following publications:

J. Thomas, A. Pukhov, I. Yu. Kostyukov, *Temporal and spatial expansion of a multi-dimensional model for electron acceleration in the bubble regime*, published to Laser and Particle Beams **32**, 277-284 (2014)

## Chapter 3

# Side injection of short electron bunches into the bubble

### 3.1 Introduction

The acceleration of electrons in the bubble regime [10] has experienced massive progress in the last decade. In this time injection techniques as the beat wave mechanism, the density gradient method, the ionization-based injection, the injection by (transverse) colliding laser pulses, and the self-injection of plasma background electrons [19–21, 65–73] have been developed. During this process the achievable electron energy has been continuously raised. Recent experiments report form bunches with energies above 10 GeV and numerical simulations suggest that the limit is not reached by far [1, 74]. The relativistic emittance of the accelerated electron bunch has been reduced to a few mm mrad while at the same time smaller energy spreads could be produced [20, 21, 25, 65, 75, 75–78]. In comparison to classical linear or circular accelerators, however, these energy spreads are rather large. Since many present-day applications base on the production of high energetic, small spread electron bunches, it is of utmost interest to develop new bubble acceleration techniques that minimize the energy spread and maximize the number of accelerated electrons.

In this chapter an injection method is presented that allows to minimize the energy spread of the accelerated electrons under a mean FWHM of 0.5% mean electron energy. Simultaneously it is shown that this method is applicable to all energy ranges if radiation effects of ultra-high energetic electrons are neglected. It is also shown that the new injection technique can trap a quit large amount (more than 70%) of injected electrons. The basic idea of this method is to switch off the self injection of background plasma electrons into the bubble and to inject a small electron cloud from side at a certain angle

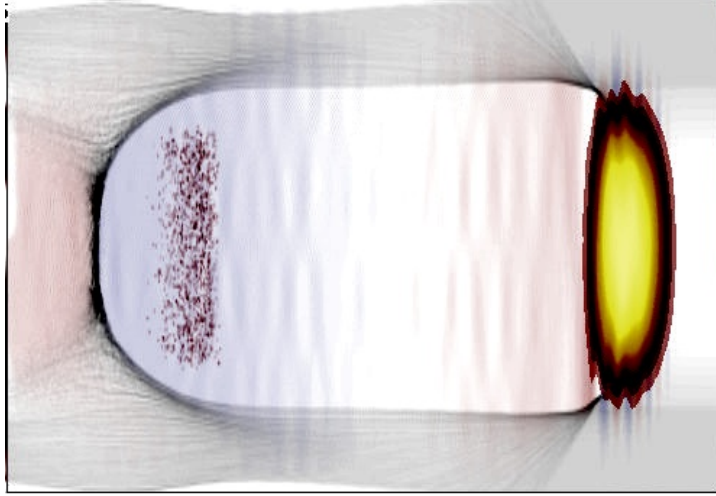


FIGURE 3.1: PIC simulation of accelerated electron bunch (red dots left) in the bubble after side injection. The driving laser pulse (yellow-red left) is far in front of the bubble and does not interact directly with the bunch.

$\alpha$ . From PIC simulations it is known that this injection method is applicable. For the discussion of the new technique this chapter models all electrons as test particles in the phenomenological bubble model of a perfect sphere with constant radius  $R_0$ . The bubble moves with laser group velocity  $V$  behind a generating laser pulse in  $z$ - direction. The bunch interaction with the laser field is neglected [10, 17, 22]. Any electron interaction is also ignored as number of accelerated electrons is always small and the inter-particle distances are large. In the first part of this chapter it is shown how side injection can be optimized to reach a minimal FWHM and a high amount of trapped electrons at the same time. In the second part the cut-off angle  $\alpha_{cut}$  beyond which no electrons that are injected from side will be trapped is calculated. Afterward, this angle is compared to full 3D simulations of an electron cloud that is injected into the bubble.

## 3.2 Bubble model and simulations

Simulations with a full 3d PIC code prove that the self-injection mechanism indeed can be suppressed. Furthermore, these simulations show that is possible inject and accelerated external electron bunches in the now always empty bubble. A PIC simulation for side injected electrons is shown in Fig.(3.1). Here a bunch of injected electrons (red dots left) was trapped in a bubble that is driven by a high intense laser pulse (yellow spot right). The electrons are in the accelerating phase of the bubble (blue background) and will stay spatially close together until the bubble breaks due to depletion of the laser pulse. In the following simulations bunches of test electrons are injected into analytically given fields from a certain 3d bubble model that allows to simply switch off self injection

[14, 22, 46]. Then the equations of motion are solved for every test particle individually. For the present analytical bubble model the wake field potential  $\Psi$  is coupled to the electromagnetic potential  $\mathbf{A}$  and the electrostatic potential  $\varphi$  via

$$\Phi(\mathbf{r}) = \frac{\xi^2 + \rho^2 - R_0^2}{4}, \quad A_{\parallel} = -\varphi = \frac{\Phi}{2}, \quad \mathbf{A}_{\perp} = 0. \quad (3.1)$$

Here,  $\rho^2 = |\mathbf{r}_{\perp}|^2$  is the displacement of the charge from the propagation axis and  $\xi = z - Vt$  because the laser pulse is propagating in  $z$ -direction. In this notion the standard relativistic normalization of variables is used: The electron plasma frequency  $\omega_{pe} = (4\pi e^2 n_0 / m_e)^{1/2}$ , the electron mass  $m_e$ , the velocity of light  $c$ , and the plasma background density  $n_0$  are used to normalize by substituting  $\mathbf{r} \rightarrow \mathbf{r}\omega_{pe}/c$  for length,  $t \rightarrow t\omega_{pe}$  for time,  $\mathbf{v} \rightarrow \mathbf{v}/c$  for velocity,  $\mathbf{p} \rightarrow \mathbf{p}/(m_e c)$  for the kinetic momentum, and  $\Phi \rightarrow e\Phi/(m_e c^2)$  for potentials.

The idea that all potentials are only depending on  $\xi$  and  $\rho$  is a quasi-static approximation of the bubble potentials. The electrical field  $\mathbf{E}$  and the magnetic field  $\mathbf{B}$  inside the bubble are  $\mathbf{E} = -\nabla\varphi - \partial/\partial t\mathbf{A}$  and  $\mathbf{B} = \nabla \times \mathbf{A}$ , so

$$\mathbf{E}(\mathbf{r}) = \frac{1}{4} \begin{pmatrix} x \\ y \\ (1+V)\xi \end{pmatrix}, \quad \mathbf{B}(\mathbf{r}) = \frac{1}{4} \begin{pmatrix} y \\ -x \\ 0 \end{pmatrix}. \quad (3.2)$$

From these analytically given fields the equations of motion for a single test electron in a co-moving frame of reference are

$$\frac{dp_{\parallel}}{dt} = -(1+V)\frac{\xi}{4} + \frac{\mathbf{r}_{\perp} \cdot \mathbf{p}_{\perp}}{4\gamma}, \quad \frac{d\xi}{dt} = \frac{p_{\parallel}}{\gamma} - V, \quad (3.3)$$

$$\frac{d\mathbf{p}_{\perp}}{dt} = -\left(1 + \frac{p_{\parallel}}{\gamma}\right) \frac{\mathbf{r}_{\perp}}{4}, \quad \frac{d\mathbf{r}_{\perp}}{dt} = \frac{\mathbf{p}_{\perp}}{\gamma}. \quad (3.4)$$

Here, the double dashed variables are the vector components of the longitudinal, in laser propagation direction pointing vectors. Those variables with a corner are the perpendicular vector components.

The setup for our simulations is shown in Fig.3.2a. Here, a cloud of test electrons (colored cloud) is injected from side at an angle  $\alpha$  into a bubble. The bubble moves with velocity  $V = \sqrt{1 - 1/\gamma_0^2}$  in  $\xi$ -direction. The initial momentum of every electron in the cloud is  $\mathbf{p}_0 = p_0(\cos(\alpha), -\sin(\alpha), 0)$ , where  $p_0 \sim N(\mu_0, 0.05\mu_0)$  is normal distributed and  $\mu_0 = 1.2\gamma_0$ . Thus, the initial energy distribution of the electron ensemble is a Gaussian as shown in Fig(3.2b). The initial position of the cloud is chosen such that its center of mass passes the point  $(0, R_0, 0)$  on the bubble border. The size of electron bunch is always  $a \times b \times b$ , where  $a = 0.5R_0$  and  $b = 0.25R_0$ . This ensures that all

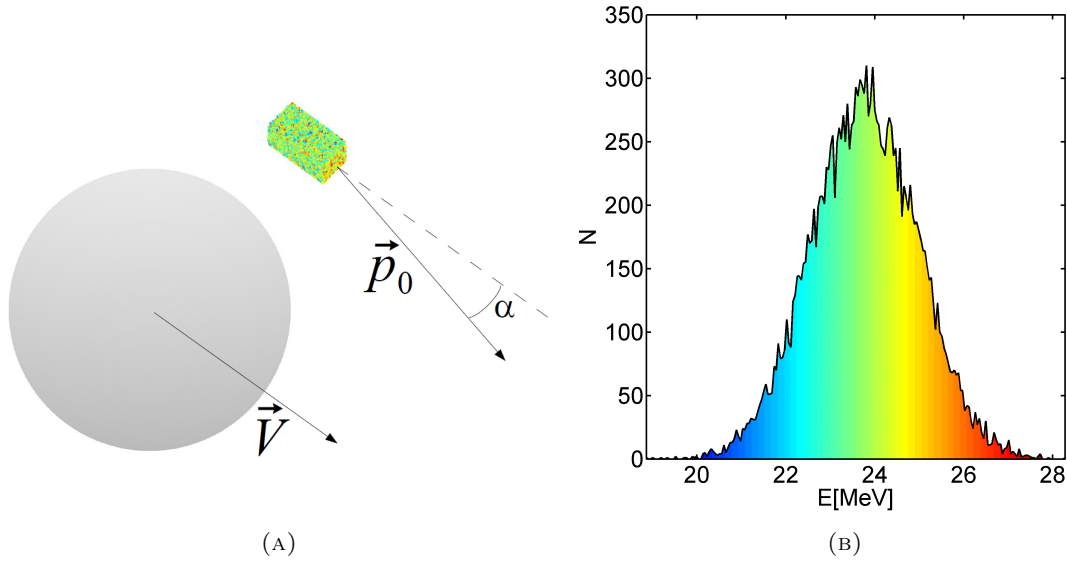


FIGURE 3.2: Simulation with  $E = 100$  J,  $\lambda_{laser} = 600$  nm, and  $a_0 = 9$ . (a): Initial configuration of the electron bunch before the injection, (b): Corresponding initial energy spectrum.

electrons in the bunch will be injected. The normalized bubble radius  $R_0$  and the bubble velocity  $V$  are calculated for a spherical laser pulse with duration  $\tau = R_0/c$ , wave length  $\lambda_{laser} = 600$  nm, dimensionless amplitude  $a_0 = 9$ , and laser energy  $E_{laser}$  between  $1J$  and  $1kJ$  according to known scaling laws[1, 28, 49]. Then the maximum sum of trapped electrons, the cut off angle, after which no electron is trapped, and the mean energy spread over all minimal energy spreads from simulations that could trap at least 50% of the bunch are analyzed. The equations of motion Eqs.(3.3)-(3.4) are solved for every electron independently.

### 3.3 Optimized side injection

During the injection process the former Gaussian shape of the energy distribution is broadened (see Fig.(3.3a)) because those electrons that enter the bubble first are also the first who are accelerated in  $\xi$ -direction (see Fig.(3.3b)). The energy spread briefly after injection is rather large because the absolute maximal energy difference in the spectrum is large compared to mean energy. The shape of the energy spectrum also has lost its Gaussian form and now looks similar to an equal distribution. In Fig.(3.3b) the initially chosen 10% energy spread already increased to 100% and will stay at this level until the injection is finished. In the hereafter following acceleration, the spectrum becomes more Gaussian like again and the spatial distribution of the electrons is dense, too.

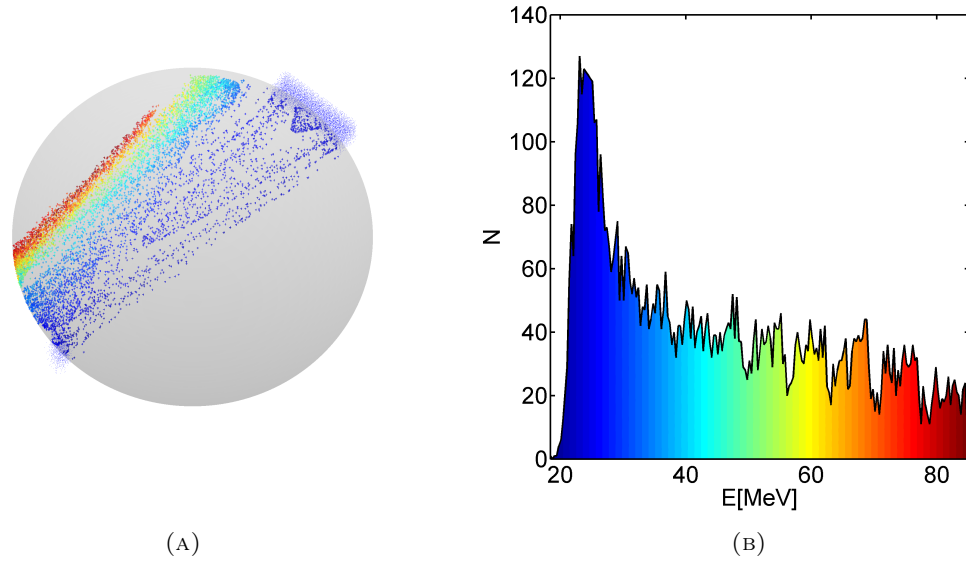


FIGURE 3.3: Simulation with  $E = 100$  J,  $\lambda_{laser} = 600$  nm, and  $a_0 = 9$ . (a): Electron distribution during the injection process, (b): Corresponding energy spectrum.

After the electron bunch has reached the dephasing length of the bubble, the mean electron energy is maximized and the energy spread is minimized. The spatial distribution is squeezed in  $\xi$ -direction and the energy spectrum is Gaussian again. In this state the transversal beam width is two times the betatron amplitude in injection direction (see Fig.(3.4a). A comparison between the color scheme of the corresponding energy spectrum in Fig.(3.4b)) and the color distribution in the bubble shows that the individual energy of the electrons has no impact on position inside the bunch. This is very different to the injection situation in Fig.(3.3a) where hot (red) electrons are always left to cold (blue) electrons. The simulation for Fig.(3.2), (3.3), and (3.4) was done for a laser pulse energy of  $E = 100$  J, a laser wave length of  $\lambda = 600$  nm, and a laser intensity of  $a_0 = 9$ . The minimal energy spread after acceleration is as low as 0.6% while the mean bunch energy is  $E_b = 4.7$  GeV.

After injection the number of finally trapped electrons strongly depends on the injection angle  $\alpha$  (see Fig.3.5a). For small angles the amount of trapped electrons is in a range of 80 – 100% but for  $\alpha$  larger than some cut off angle  $\alpha_{cut}$  the hole electron bunch passes the bubble and no charge is trapped. Now, the main goal of a series of simulations is to find out, how far the energy spectra of the injected and accelerated electrons can be compressed. Of course, the minimal energy spread is always found in a vicinity of  $\alpha_{cut}$  since then the spatial distribution is always point like. In the simulation series, however, it is not only important to find a minimal energy spread but also to maximize the number of trapped electrons. Thus, the mean minimal energy spread  $\langle FWHM \rangle$  is calculated over all injection angles for which more than 50% of all electrons are trapped.

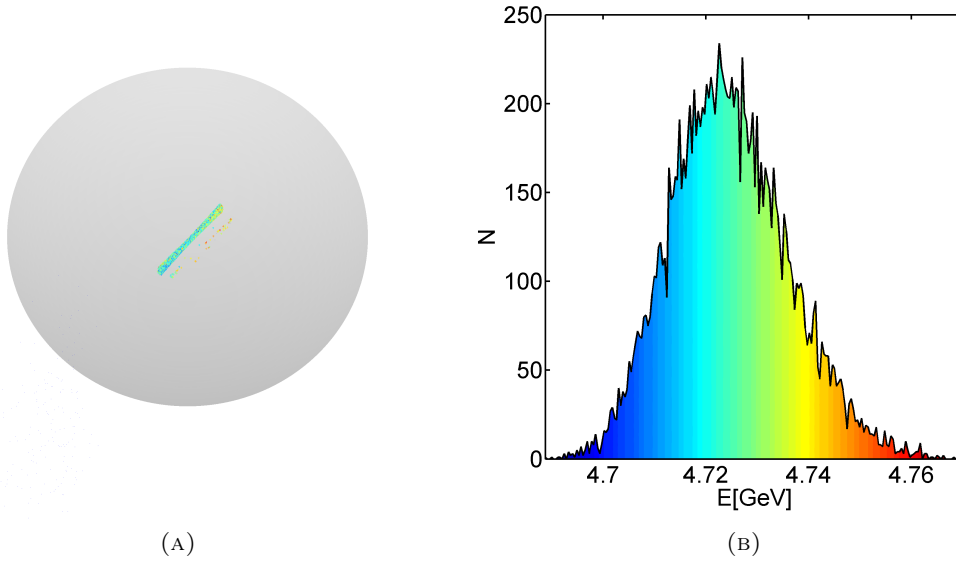


FIGURE 3.4: Simulation with  $E = 100$  J,  $\lambda_{laser} = 600$  nm, and  $a_0 = 9$ . (a), (b): Electron bunch after injection and spectrum with  $FWHM = 0.6\% \mu$ .

The simulation series varies the laser energy but fixes both the intensity  $a_0 = 9$  and the laser wave length  $\lambda = 600$  nm in order to fix the normalized bubble radius  $R_0 = 3.6$ , too. Then the geometry of the bubble-bunch configuration remains the while and all other laser-plasma parameters like laser power, laser duration and plasma density are adjusted. An overview about the scaling of these parameters is given in Tab.3.1.

Fig.3.5b shows the connection between  $\langle FWHM \rangle$  and  $E$ . Here it can be observed that  $\langle FWHM \rangle$  decreases with increasing laser energy. The reason therefor is that two counteracting effects determine the energy spread. The first effect which raises the energy spread is that the angle of incidence must be chosen smaller the higher  $\gamma_0$  is. With decreasing  $\alpha$  the injection time increases and thus the spectrum is broadened from the beginning on. The other, helping effect is that the maximal energy of the trapped electron cloud strongly increases with  $E_{laser}$  and thus reduces the ratio  $\Delta\gamma/\gamma$ .

The maximum amount of trapped electrons seams to be weakly dependent from the laser energy and is always above 75%. The progression of Fig.(3.6a), however, indicates

$E_{laser}$ [J]	$P_{laser}$ [W]	$E_{mono}$ [GeV]	$n_e/n_c$	$\tau$ [fs]	S	$R$ [ $\lambda_{laser}$ ]
1	$1.2 \times 10^{14}$	0.24	$1.9 \times 10^{-2}$	8.3	$2.1 \times 10^{-3}$	4.2
10	$5.6 \times 10^{14}$	1.1	$4.1 \times 10^{-3}$	18	$4.5 \times 10^{-4}$	9
100	$2.6 \times 10^{15}$	5.1	$8.7 \times 10^{-4}$	39	$9.7 \times 10^{-5}$	19
1000	$1.2 \times 10^{16}$	23	$1.9 \times 10^{-4}$	83	$2.1 \times 10^{-5}$	42

TABLE 3.1: Overview about the scaling of the laser-plasma parameter for simulations of the side injection method for  $\lambda_{laser} = 600$  nm,  $a_0 = 9$ , and  $n_c = 3.1 \times 10^{21}$  cm $^{-3}$ .

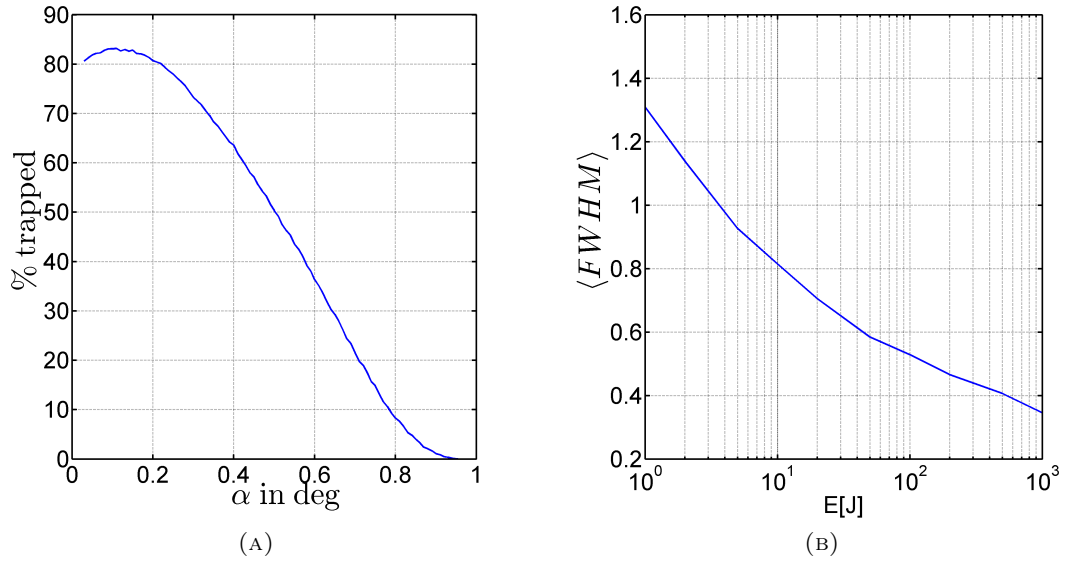


FIGURE 3.5: (a): Rel. number of trapped electrons vs incidence angle for  $E = 100J$ ,  $\lambda_{laser} = 600nm$ ,  $a_0 = 9$ . (b): Mean FWHM of the energy spectra for different laser energies. The mean value is calculated for all those spectra that contain at least 50% of all particles.

that the limit decreases with increasing laser energy. In contrast to that the angle at which the maximum of trapped electrons is observed -  $\alpha_{max}$  - strongly depends on  $E$ . As Fig.(3.6b) shows  $\alpha_{max}$  converges to 0 for large  $E_{laser}$ . The cut off angle after which no electrons could be trapped also converges to 0 for large  $E_{laser}$  (see Fig.3.8b) but is for laser energies in the bulk of 1 J to 100 J one order of magnitude larger than  $\alpha_{max}$ . As seen in Fig.(3.5a) the number of trapped particles rapidly decreases for  $\alpha > \alpha_{max}$ . Thus it is favorable to inject bunches between  $\alpha_{max}$  and  $\alpha_{cut}$ . The next section introduces an analytical estimate for the cut off angle and shows how it scales with the laser energy.

### 3.4 Analytical estimate of the cut off angle

If the equations of motion are solved for a single test electron, the solution is the trajectory shown in Fig.3.8a. Here, the electron oscillation fast around the  $\xi$ -axis and approaches the bubble center slowly. The fast oscillations are well known betatron oscillations that are also seen in experiments [20, 26, 27]. To calculate the cut-off angle it is necessary to know an approximation function to the envelope of this oscillation and solutions of  $\xi(t)$  and  $p_{\parallel}(t)$  near the bubble center. The latter can be calculated from a guiding center approximation for times near the critical time  $t_{max}$  with  $\xi(t_{max}) = 0$ . The guiding center approximation takes only the mean displacement of an electron from the  $\xi$ -axis into account. This, however, is zero and the differential equation system for

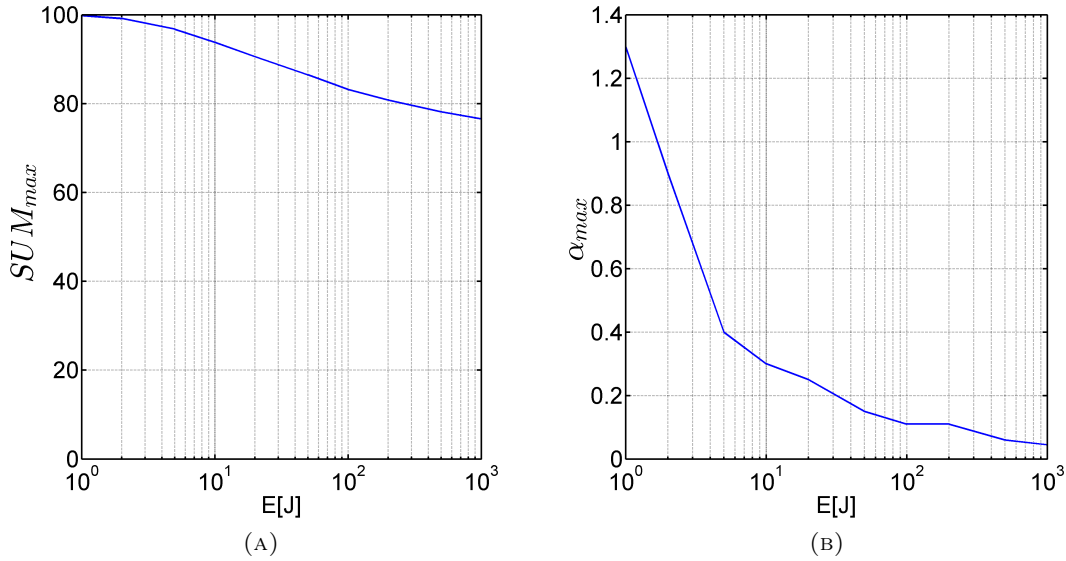


FIGURE 3.6: (a): Maximal sum of trapped electrons vs laser energy. (b): Injection angle at which the maximal sum of trapped electrons is achieved.

$\xi(t)$  and  $p_{||}(t)$  in terms of  $\tau = t - t_{max}$  becomes

$$\frac{dp_{||}}{d\tau} = -(1+V)\frac{\xi}{4}, \quad \frac{d\xi}{d\tau} = \frac{p_{||}}{\gamma} - V \approx \frac{1}{2\gamma_0^2} - \frac{1}{2\gamma^2}. \quad (3.5)$$

Since the energy of the electro is maximal for  $\tau = 0$ , the velocity  $d\xi/d\tau$  is nearly constant in a wide range of the bubble. The solutions to these equations are then deduced from the initial conditions  $\xi(\tau = 0) = 0$  and  $\gamma(\tau = 0) = \gamma_{max}$  by simply integrating

$$\gamma(\tau) \approx p_{||}(\tau) \approx \gamma_{max} - \frac{(1+V)\tau^2}{16\gamma_0^2}, \quad \xi(\tau) \approx \frac{\tau}{2\gamma_0^2}. \quad (3.6)$$

A combination of Eqs.(3.3) and (3.4) leads to a second order ODE for  $\rho(\tau) = |\mathbf{r}_{\perp}(\tau)|$ . In the limit  $\rho'(\tau)^2/2 \ll 1$  this ODE becomes the damped harmonic oscillator

$$\rho''(\tau) + P\rho'(\tau) + Q\rho(\tau) = 0 \quad (3.7)$$

with coefficient functions  $P = -\tilde{V}\xi/(4\gamma)$ ,  $Q = 1/(2\gamma)$ , and  $\tilde{V} = 1 + V$ . The approximation  $\rho'(\tau)^2/2 \ll 1$  is applicable because the envelope function varies slowly in time (compare Fig.3.8a). To separate the slowly evolving envelope from the fast oscillation, the trajectory of the test electron in the  $\rho - \xi$ -plane is canonically identified with a complex function  $f : \mathbb{R} \rightarrow \mathbb{C}$ . The phase function of  $f$  then bears the information about the fast betatron oscillation which occurs on a much shorter time scale than the evolution of the envelop function. To model this two different times scales properly a smallness

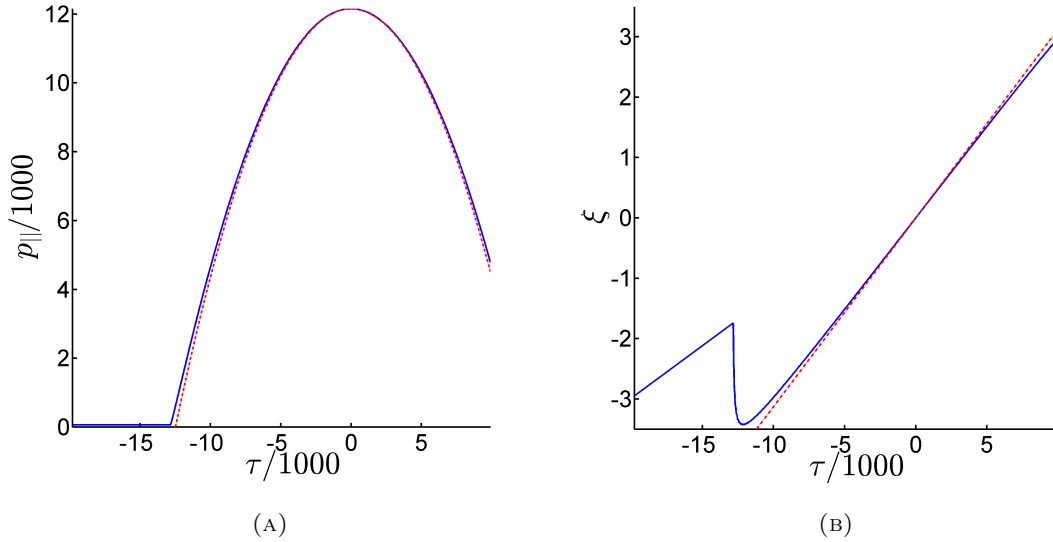


FIGURE 3.7: Guiding center approximation to  $p_{\parallel}$  and  $\xi$ . (a): The blue solid line is the  $p_{\parallel}(\tau)$  function, the red dotted line is the guiding center approximation to  $p_{\parallel}$ . (b): The blue solid line is the  $\xi(\tau)$  function, the red dotted line is the guiding center approximation to  $\xi$ .

parameter  $\epsilon$  is introduced. Then it is convenient to define

$$\rho(\tau) = g(\epsilon\tau)e^{i\tau}. \quad (3.8)$$

and postulate  $\epsilon^2 \equiv 0$ . In this multi-scale approach  $g(\epsilon\tau)$  is an arbitrary complex function with a slowly developing complex amplitude and a certain phase. The phase of  $\rho(\tau)$  is coded in the sum of this phase and the one from the exponential function and describes the motion betatron oscillation of the particle. If this multi-scale approach is substituted in Eq.(3.7) a new first order ODE with known time-dependent coefficient functions for the slowly varying function evolves

$$g'(\epsilon\tau)(2i + P)\epsilon + g(\epsilon\tau)(-1 + iP + Q) = 0. \quad (3.9)$$

The complex part describes how the electron slowly approaches the bubble center. The real part of Eq.3.9 is the envelop approximation function  $\tilde{\rho}(\tau)$  so

$$\tilde{\rho}(\tau) = A \exp\left(-\frac{1}{\epsilon} \int \frac{P(1+Q)}{P^2+4} d\tau\right). \quad (3.10)$$

The solution to the integral expression on the right hand side can be expressed as

$$I = -\frac{1}{8} \log(a - \tilde{V}\tau^2 + b\tau^4) + \frac{c}{4\tilde{V}^2} \tan^{-1}(4\tau^2 - 1) \quad (3.11)$$

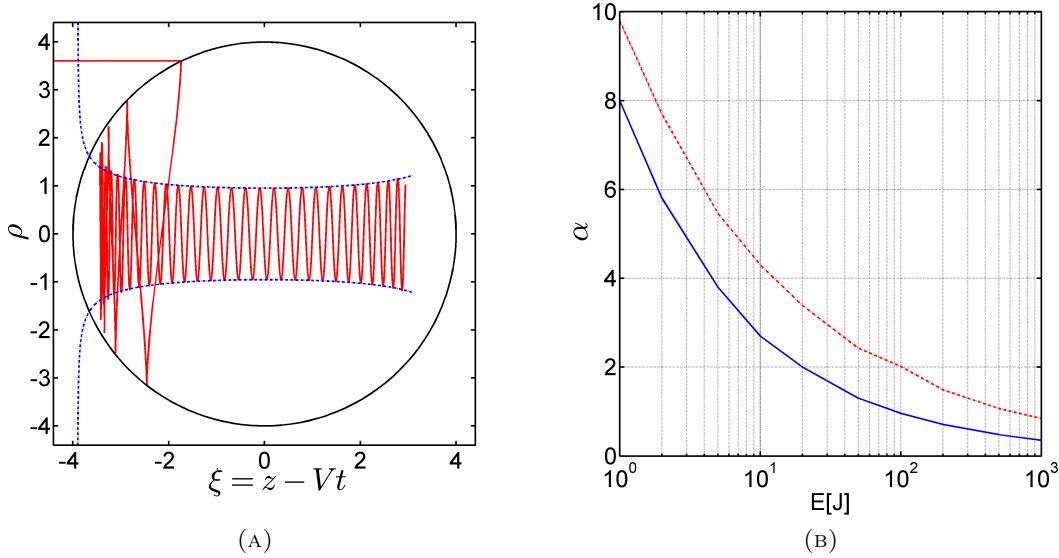


FIGURE 3.8: (a): Trajectory in the 2D model together with amplitude envelope approximation functions. (b): Cut off angle vs laser energy for simulations with  $\lambda_{laser} = 600nm$  and  $a_0 = 9$ . Red dotted line: analytical prediction; Blue solid line: numerical simulations.

with  $a = 8\gamma_0^2(2\gamma_{max} + 1)$ ,  $b = 256\gamma_0^4\gamma_{max}$ , and  $c = \tilde{V}^2 - 32\gamma_0^2\gamma_{max}\tilde{V}$ . This solution has two degrees of freedom, namely the  $A$  and  $\epsilon$ . To fit  $\tilde{\rho}(\tau)$  to the actual trajectory two points  $(\rho_1, \tau_1)$ ,  $(\rho_2, \tau_2)$  are taken from a single one particle simulation. Then the two degrees of freedom are determined via

$$\epsilon = \frac{I(\tau_1) - I(\tau_2)}{\log(\rho_1/\rho_2)}, \quad A = \rho_1 \exp\left(\frac{I(\tau_1)}{\epsilon}\right). \quad (3.12)$$

These solutions together with Eq.(3.10) give the envelop approximation function  $\tilde{\rho}(\tau)$ . In contrast to [17, 18] this approximation is found without any reductions of the phenomenological bubble model.

A plot of a single test electron trajectory as solid red line in Fig.(3.8a) together with the analytical envelope approximation function  $\tilde{\rho}$  as dotted blue line shows that the approximation fits as long as the Taylor expansions to  $\gamma(\tau)$  and  $\xi(\tau)$  hold. This in turn is true as long as the trapping process is successfully passed. Nevertheless, the time at which the envelop approximation function crosses the bubble border is approximately the time at which the electron's guiding center drift in  $\xi$ -direction is reversed and the electron gets trapped.

An important application for the amplitude envelope approximation function in Eq.3.10 is to estimate the cut-off angle  $\alpha_{cut}$  beyond which no injected electrons can be trapped. To estimate  $\alpha_{cut}$  analytically, it is necessary to determine the distance of the electron to

the bubble origin at any time the electron is inside the bubble. A single test electron that enters the bubble at  $\mathbf{r} = (0, R_0, 0)$  with  $\mathbf{p} = p_0(\cos(\alpha), -\sin(\alpha), 0)$ , and  $\gamma(0) = \gamma_b = 1.2\gamma_0$  is a representative example. It has the same initial parameters as the center of mass of the injected electron bunch in the previous section. The Hamiltonian of this test electron is  $H(\mathbf{r}, \mathbf{p}) = \gamma - Vp_{\parallel} + (1 + V)\Phi(\mathbf{r})/2$ . Since the present bubble model assumes that the bubble radius  $R_0$  is constant the Hamiltonian is a constant of motion and the initial conditions give

$$\gamma - Vp_{\parallel} + \frac{\tilde{V}}{2}\Phi(\mathbf{r}) = \gamma_b - V\cos(\alpha)p_0 \quad (3.13)$$

If the wake field potential  $\Phi = (|\mathbf{r}|^2 - R_0^2)/4$  is substituted the test electron approaches the bubble center according to

$$|\mathbf{r}|^2 \approx \frac{8}{\tilde{V}}(\gamma_b - V\cos(\alpha)p_0) - \frac{4p_{\parallel}}{\tilde{V}\gamma_0^2} + R_0^2. \quad (3.14)$$

To decide, whether the electron will be trapped, it is necessary to look at the points of maximal  $|\mathbf{r}|$ . These are found with  $d|\mathbf{r}|/dt \stackrel{!}{=} 0$ , or equivalently  $|\rho(\tau_{cirt})||\rho'(\tau_{cirt})| = \tilde{V}|\xi(\tau_{cirt})|$  for a certain  $\tau_{cirt}$ . The key to find the right  $\tau_{cirt}$  is to substitute  $\rho'(\tau)$  from Eq.(3.9) and to write a new equation in terms of  $\tilde{\rho}(\tau)$ . Then

$$\tilde{\rho}^2(\tau_{cirt}) \left( 1 + \left| \frac{P(\tau_{cirt})(1 + Q(\tau_{cirt}))}{P(\tau_{cirt})^2 + 4} \right| \right) = \tilde{V}|\xi(\tau_{cirt})|. \quad (3.15)$$

gives the critical time  $\tau_{cirt}$  at which the electron is near the bubble border. The solution to this equation is determined by the envelope approximation function and the approximating functions to  $\gamma(\tau)$  and  $\xi(\tau)$  solely. The externally injected test electron stays trapped if  $\mathbf{r}^2 \leq R_0^2$  for all  $\tau$ . As a consequence

$$|\alpha| \leq \arccos \left( \frac{\gamma_b}{Vp_0} - \frac{\gamma(\tau_{cirt})}{2Vp_0\gamma_0^2} \right) \approx \arccos \left( 1 - \frac{\gamma(\tau_{cirt})}{2p_0\gamma_0^2} \right) \quad (3.16)$$

is an explicit restriction to the angle of incidence  $\alpha$ . The critical time  $\tau_{cirt}$ , however, must be calculated numerically from Eq.(3.15). As is easy to see, for large initial electron energies the maximum applicable angle is not depending on the bubble radius but on the laser group velocity and the momentum of the injected electron.

A comparison between the analytically found cut-off angle (red dotted line) with found angles from 3d multi particle simulations (solid blue line) is shown in Fig.(3.8b). Here  $\alpha_{cut}$  is plotted against the applied laser energy while the initial energies for the calculation of Eq.(3.16) is always chosen as  $\gamma(0) = \gamma_b = 1.2\gamma_0$ . Both graphs in Fig.(3.8b) converge to zero for large  $E_{laser}$ . This behavior is now better understood since  $\arccos(1 - \gamma(\tau_{cirt})/2.4\gamma_0^2) \rightarrow 0$  for  $\gamma_0 \rightarrow \infty$ . The offset between both lines can be explained from the fact that not all

electrons in the many particle simulations pass the point  $\mathbf{r} = (0, R_0, 0)$  and have different energies. Thus all electrons have different initial conditions and Eq.(3.16) gives an upper bound for  $\alpha_{max}$ .

### 3.5 Conclusion

In this chapter a new injection mechanism for the bubble regime of electron acceleration is discussed. The lateral injection of an electron bunch under a certain angle into the bubble has been investigated. Furthermore, it is shown that the mean FWHM as well as the trapping rate can be optimized if the injection angle is chosen small enough. An analytical estimate for the maximal applicable injection angle is found from a guiding center approximation and a multi-scale approach to the envelope approximation function of the trajectory of a single test electron.

An important conclusion of this chapter is that for high laser energies  $E \geq 50J$  and small injection angles  $\alpha \approx \pi/180$  rad the minimal FWHM of the trapped electron bunches can be pushed well under 0.5% of the actual bunch energy. At the same time, the ratio of trapped electrons stays well above 70% for all energies. The cut-off angle above which no electrons can be trapped is reviewed numerically in 3d multi particle simulations and analytically evaluated in a reduced 2d model. The comparison shows that for laser energies  $E \geq 50J$  both angles are comparable but not for lower energies. Consequently, the side injection of electron bunches in the GeV-regime is a promising accelerating and focusing mechanism that will be a center of interest for the next time.

Another important aspect of the side injection, that has been ignored so far, is the effect of radiation reaction of accelerated electrons. In the bubble regime the field strength is small compared to the Schwinger fields but if the electron energies are in the order of 10 GeV and above, radiation reaction effects become important. The simulations with highest energies in this chapter involve laser energies of  $J=1$  kJ and lead to mean electron bunch energies in the range of 23 GeV. Since the energy spread is minimized for these high energies, the following chapter discusses the impact of radiation reactions on the optimized side injection for high and ultra-high laser energies.

Results from this chapter are/will be published in the following publications:

J. Thomas, O. Jansen, A. Pukhov, *Side injection and full solution to the bubble model*, to be submitted

## Chapter 4

# A radiation model for high electron energies in the GeV and TeV regime

### 4.1 Introduction

Research in ultra-relativistic laser-material interaction is progressing significantly [48, 79]. At present, table top laser intensities of  $10^{19}$  W/cm<sup>2</sup> are available based on chirped pulse amplification methods, while larger laser systems may deliver intensities up to  $I \approx 10^{23}$  W/cm<sup>2</sup> at the focal spot. In the near future, extreme laser intensities  $I \gg 10^{23}$  W/cm<sup>2</sup> are expected to become available. Electrons that directly interact with laser pulses of these intensities are accelerated to ultra-high energies within a fraction of the laser period [80]. If this happens, non-linear effects like radiation reaction due to the huge acceleration and self-interaction become important [81]. One of the most important phenomena of laser-matter interaction at these intensities is the production of electron-positron pairs from vacuum and the appearance of showers of charged particles. These showers are produced by repeated emission of hard photons and pair creation by hard photons. Qualitative estimations predict that cascades might arise as soon as the field strength exceeds a certain threshold [82]

$$E_s = \frac{m_e^2 c^3}{e \hbar} \approx 1.3 \times 10^{18} \text{V/m} \quad (4.1)$$

where  $\hbar$  is the reduced Plank constant,  $m_e$  is the electron mass, and  $c$  is the speed of light [83–86]. In general  $E_s$  is also referred to as the Schwinger field because Julian Schwinger first derived the leading nonlinear corrections to electro magnetic fields in the non-linear regime and calculated the production rate of electron-positron pairs in a strong field.

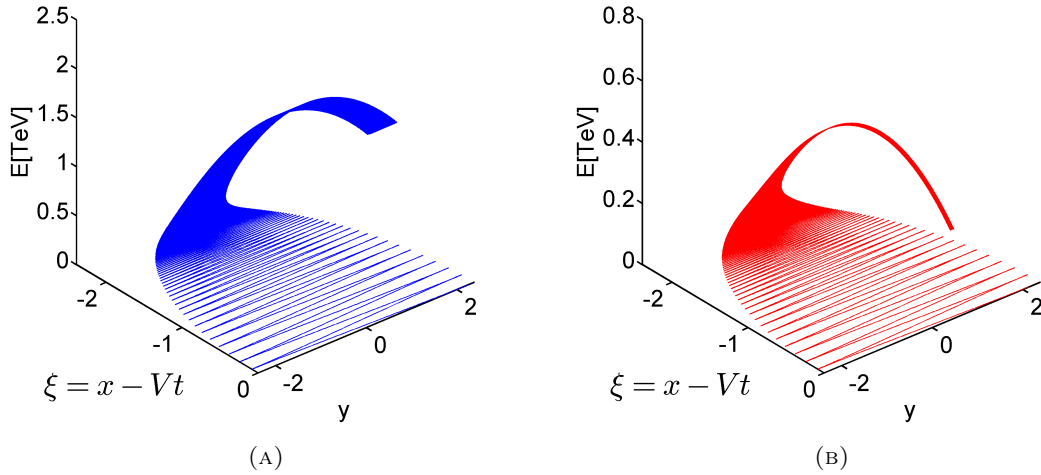


FIGURE 4.1: Comparison of energy gain with and without radiation reaction effects in a simulation with  $a_0 = 4$ ,  $\lambda_{laser} = 1 \mu\text{m}$ , and  $E = 1 \text{ MJ}$ . (a): Phase space plot of the trajectory of a test charge without RR. (b): Phase space plot of the trajectory of a test charge with RR.

Similar to the last chapters this chapter treats the laser wake field acceleration and the side injection of dense electron bunches. Different to the last chapters here it is considered that the electron energies are so high enough that radiation reaction effects must be considered. In general, the laser wake field based acceleration uses a plasma wave with a phase velocity that is close to the speed of light to accelerates trapped electrons to ultra-high energies. The wake is driven by a short high intense laser pulse and electrons can be injected and trapped by various techniques. A special case of the laser wake field acceleration is the so called bubble regime, in which all electrons are radially expelled from a volume that is created by the laser pulse [10]. A necessary condition for this regime is that the laser pulse length is shorter than the plasma wavelength and fits into the first half of the period. The bubble regime cannot be described by fluid dynamics anymore. However, recent bubble models have been introduced that describe the inner electromagnetic fields, the boundary, and the trapping of electrons in the bubble [9, 10, 12, 14, 16–18, 22]. All these models neglect the direct electron-laser interaction but recent scaling laws connect the bubble shape, the bubble speed, and the acceleration length with the laser intensity. Scalings for highest energies suggest to use laser pulses with durations of  $\tau = R/c$ , where  $R$  is the laser radius and  $c$  is the speed of light. Then the bubble takes the form of a sphere and trapped electron bunches - the so called beam load - are accelerated until the laser is depleted or the bunch has reached the dephasing length [1, 16, 28, 87].

If electrons are accelerated to energies in the GeV and TeV range new effects like radiation

reaction (RR) appear. A comparison of single particle simulations in the bubble regime in Fig.(4.1) gives a strong impression about the impact of the RR. Here, two phase space plots of a single trapped electron are shown. In Fig.4.1a the simulation neglects RR while Fig.4.1b is from a simulation with same parameters but under consideration of RR. In both simulations an electron was injected into a bubble that is driven by a 1 MJ laser pulse with wave length  $\lambda = 1 \mu\text{m}$  and intensity  $I = 2.2 \times 10^{19} \text{ W/cm}^2$ . For the blue graph in Fig.(4.1a) the equations of motion (3.3) and (3.4) are solved. The highest energy the electron could reach after it has reached the dephasing length is more than 1.5 TeV (see projection of the blue graph to the energy axis). In contrast to that, for the red graph in Fig.(4.1b) the equations of motion are completed by a classical radiation term that is introduced in the following sections. The betatron amplitude of the damped electron is much smaller than the amplitude of the undamped one and the maximum energy (see projection of red graph to the energy axis) is not more than than 500 GeV - this is a factor of three between both maximum energies.

This chapter discusses the impact of radiation reaction on the maximum achievable electron energy after bubble acceleration. Furthermore, the discussion of the last chapter is extended to the current situation, so the laser energy will be varied again while the laser intensity and the laser wave length is fixed. In the following, section 4.2 introduces a new analytical bubble model that includes classical radiation reaction effects for high electron energies. An application of the new model is given in section 4.3, 4.4, and 4.5 where the side injection of electron bunches is optimized again to achieve minimal energy spreads and to maximize the number of trapped electrons at the same time. Different to the last chapter this is also done for laser energies in the MeV regime. The following section 4.6 estimates the radiated energy for high energies and corrects the expected maximum energy gain from recent bubble scaling laws. The end of this chapter is a conclusion and summary.

## 4.2 Relativistic radiation damping

If radiation of relativistic and ultra-relativistic charges in external electromagnetic fields is considered, there are two principle ways to treat the particle field interaction. The first way is to describe the radiation in the frame work of QED [88, 89]. Here, the electrons are scattered at photons from the bubble back ground field. Every time this event happens, the electron energy might be reduced drastically and the electron's momentum must be calculated from the conservation of the four-momentum  $p_e^\mu + q^\mu = p_e'^\mu + p_\gamma^\mu$ . Here  $p_e^\mu$  is the four-momentum of the accelerated electron,  $q^\mu$  is the momentum extracted from the bubble field,  $p_e'^\mu$  is the momentum of the electron after the scattering process, and  $p_\gamma^\mu$  is

the momentum of the emitted photon. Common simulation techniques for this approach are quantum Monte-Carlo simulation [86, 90–92].

The other way to include radiation reaction into the acceleration model of the bubble regime is to treat the radiation classically. In this case a basic idea from Lorentz, Abraham, and Dirac (LAD) [81] is sufficient for the description of the new set of equations of motion. For relatively weak fields, the Landau-Lifshitz approach (which is followed in this thesis) is widely accepted [93] because it does not produce paradox situations as e.g. a diverging acceleration in the absence of an external field and it is equivalent to the LAD equation up to the first order in the coupling parameter [94]. To decide which approach is best suited to describe radiation reaction in the bubble regime an investigation of the Lorentz-invariant QED parameter

$$\chi = \sqrt{\left(\gamma \frac{\mathbf{E}}{E_s} + \frac{\mathbf{p}}{m_e c^2} \times \frac{\mathbf{B}}{B_s}\right)^2 - \left(\frac{\mathbf{E} \cdot \mathbf{p}}{m_e c^2 E_s}\right)^2} \quad (4.2)$$

is helpful. In general it is understood that if  $\chi \ll 1$  the loss of energy due to emission of a single photon is negligible and the damping can be describes in a continuous classical theory. If, in contrast to that,  $\chi \geq 1$  the emission causes both a considerable loss of energy and a recoil in moving direction. Hence, the radiation must be treated in terms of QED.

In this thesis the electron energies are considered to be quiet large but the bubble fields are usually small enough to ensure that the QED parameter of every test charge in the simulations is much smaller than unity. A representative example therefor is shown in Fig.(4.2). Here both the local field strength  $\sqrt{\mathbf{E}^2 + \mathbf{B}^2}$  and the QED parameter are calculated for a single test electron and the same the simulation parameters as in Fig.(4.1). Since the fields are linear in the distance to the axis, the field strength is strongest when the electron enters the bubble and vanish as soon as the electron reaches the dephasing length [see Fig.(4.2a)]. The QED parameter as seen by the electron is shown in Fig.(4.2b). If radiation reaction is not included (black line) the maximum of  $\chi$  is  $0.1 < 1$ . In contrast to that the consideration of radiation (red line) decreases the electrons energy while the fields are the same so that  $\max \chi = 0.007 \ll 1$ . Thus it is justified to treat radiation reaction in the bubble regime classical.

In the following, RR is described as in Landau-Lifschitz (LL) §75 [93]. So the general covariant formulation of the equations of motion for a relativistic particle with mass  $m$  and charge  $q$  in the presence of an electromagnetic field is

$$mc \frac{du^i}{ds} = \frac{q}{c} F^{ik} u_k + g^i. \quad (4.3)$$

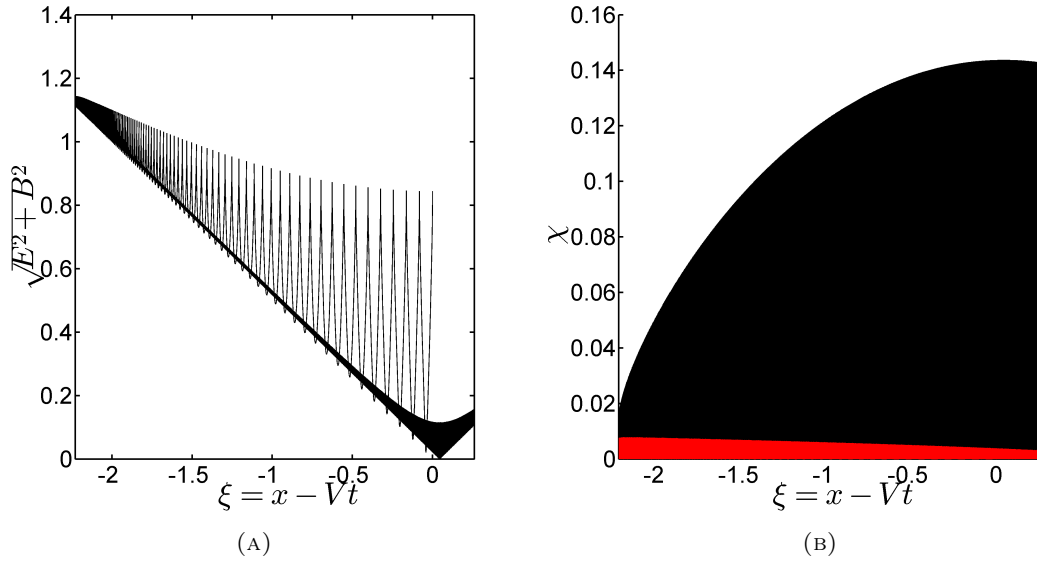


FIGURE 4.2: QED parameter and field strength as seen by a test charge which is accelerated in the bubble. (a): Field strength as seen by a fast oscillating test charge in a simulation without RR. (b): Fast oscillating QED parameter as seen by a test charge with RR (red) and without RR (black). The envelope of  $\chi$  shows that a classical approach to RR is justified.

The force four-vector  $g^i$  can be formulated in the Lorentz-Abraham-Dirac form [81]

$$g^i = \frac{2}{3} \frac{e^2}{c} \left( \frac{d^2 u^i}{ds^2} - u^i u^k \frac{d^2 u_k}{ds^2} \right). \quad (4.4)$$

In this form the three space components of  $g^i$  go over into  $g^i \approx f = 2e^2 \ddot{\mathbf{v}} / (3c^3)$  for  $|\mathbf{v}|/c \ll 1$  and it is  $g_i g^i = 0$ . The force  $f$  in turn is related to dipole radiation [see §75 in [93]] which is the first kind of radiation that appears in the general theory of interacting charges in an electromagnetic field. The basic idea of LL is to neglect all derivatives  $dg^i/ds$  which is equivalent to the assumption that  $g^i$  is small in the rest frame of the particle. In the special case that the charge is an electron it is  $m = m_e$ ,  $q = -e$ , and

$$g^i \approx \frac{2}{3} \frac{e^2}{c} \left[ -\frac{e}{m_e c^2} \frac{\partial F^{ik}}{\partial x^l} u_k u^l - \frac{e^2}{m_e^2 c^4} F^{ik} F_{lk} u^l + \frac{e^2}{m_e^2 c^4} (F_{lk} u^k) (F^{lm} u_m) u^i \right]. \quad (4.5)$$

A further discussion of all terms in this expression is given in [93, 95].

In terms of the coupling constant  $\Lambda = 2/3 \cdot e^2 \omega_p / (m_e c^3)$  and after a normalization of variables according to  $x \rightarrow x \omega_{pe} / c$ ,  $t \rightarrow t \omega_{pe}$ ,  $\mathbf{v} \rightarrow \mathbf{v} / c$ ,  $\mathbf{p} \rightarrow \mathbf{p} / (m_e c)$ , and  $\Phi \rightarrow e \Phi / (m_e c^2)$ , where  $\omega_{pe} = (4\pi e^2 n_0 / m_e)^{1/2}$  is the electron plasma frequency and  $n_0$  is the

plasma background density, the equations of motion for an electron are

$$\frac{d\mathbf{r}}{dt} = \frac{\mathbf{p}}{\gamma}, \quad (4.6)$$

$$\frac{d\mathbf{p}}{dt} = -(\mathbf{E} + \mathbf{v} \times \mathbf{B}) + \mathbf{R}\mathbf{R}_1 + \mathbf{R}\mathbf{R}_2 + \mathbf{R}\mathbf{R}_3, \quad (4.7)$$

$$\mathbf{R}\mathbf{R}_1 = -\Lambda\gamma \left[ \frac{d\mathbf{E}}{dt} + \mathbf{v} \times \frac{d\mathbf{B}}{dt} \right], \quad (4.8)$$

$$\mathbf{R}\mathbf{R}_2 = -\Lambda\mathbf{v}\gamma^2 [(\mathbf{E} + \mathbf{v} \times \mathbf{B})^2 - (\mathbf{E} \cdot \mathbf{v})^2], \quad (4.9)$$

$$\mathbf{R}\mathbf{R}_3 = +\Lambda[\mathbf{E}(\mathbf{E} \cdot \mathbf{v}) + (\mathbf{E} \times \mathbf{B}) - \mathbf{B} \times (\mathbf{B} \times \mathbf{v})]. \quad (4.10)$$

After the normalization the QED parameter is

$$\chi = \frac{3}{2} \frac{\Lambda}{\alpha} \sqrt{(\gamma\mathbf{E} + \mathbf{p} \times \mathbf{B})^2 - (\mathbf{E} \cdot \mathbf{p})^2} \quad (4.11)$$

where  $\alpha = e^2/\hbar c = 1/137$  is the fine structure constant. The electromagnetic field inside the bubble is given independently from the electron energy. An analytical expression from a recent phenomenological model is [17]

$$\mathbf{E} = \frac{1}{4} \begin{pmatrix} (1+V)(x-Vt) \\ y \\ z \end{pmatrix} \quad \mathbf{B} = \frac{1}{4} \begin{pmatrix} 0 \\ z \\ -y \end{pmatrix}, \quad (4.12)$$

where  $V = \sqrt{1 - 1/\gamma_0^2} \approx 1$  is the velocity of the bubble. If these fields are substituted into Eqs.(4.6-4.10) and transformed into the co-moving frame of reference  $\xi = x - Vt$ , a new set of equations arises that represents a new bubble model for trapped test-electrons

$$\frac{dp_{\parallel}}{dt} = -(1+V)\frac{\xi}{4} + \frac{\mathbf{r}_{\perp}}{4} \cdot \frac{\mathbf{p}_{\perp}}{\gamma} + \Lambda G_x, \quad \frac{d\xi}{dt} = \frac{p_{\parallel}}{\gamma} - V \quad (4.13)$$

$$\frac{d\mathbf{p}_{\perp}}{dt} = -\left(1 + \frac{p_x}{\gamma}\right) \frac{\mathbf{r}_{\perp}}{4} + \Lambda \mathbf{G}_{\perp}, \quad \frac{d\mathbf{r}_{\perp}}{dt} = \frac{\mathbf{p}_{\perp}}{\gamma}. \quad (4.14)$$

Here, the radiation factor  $\mathbf{G}$  collects all terms in  $\mathbf{R}\mathbf{R}_1$  to  $\mathbf{R}\mathbf{R}_3$  which are

$$\frac{d\mathbf{E}}{dt} + \mathbf{v} \times \frac{d\mathbf{B}}{dt} = \frac{1}{4\gamma^2} \begin{pmatrix} \tilde{V}(\gamma p_x - \gamma^2 V) - |\mathbf{p}_{\perp}|^2 \\ (\gamma + p_x)p_y \\ (\gamma + p_x)p_z \end{pmatrix}, \quad (4.15)$$

$$(\mathbf{E} + \mathbf{v} \times \mathbf{B})^2 = \frac{1}{16\gamma^2} [\tilde{V}^2 \xi^2 \gamma^2 - 2\tilde{V}\xi\gamma\mathbf{r}_{\perp} \cdot \mathbf{p}_{\perp} + (\mathbf{r}_{\perp} \cdot \mathbf{p}_{\perp})^2 + (\gamma + p_x)^2 |\mathbf{r}_{\perp}|^2], \quad (4.16)$$

$$(\mathbf{E} \cdot \mathbf{v})^2 = \frac{1}{16\gamma^2} [\tilde{V}^2 \xi^2 p_x^2 + 2\tilde{V}\xi p_x \mathbf{r}_\perp \cdot \mathbf{p}_\perp + (\mathbf{r}_\perp \cdot \mathbf{p}_\perp)^2], \quad (4.17)$$

$$\mathbf{E}(\mathbf{E} \cdot \mathbf{v}) = \frac{1}{16\gamma} \begin{pmatrix} \tilde{V}\xi(\tilde{V}\xi p_x + \mathbf{r}_\perp \cdot \mathbf{p}_\perp) \\ y(\tilde{V}\xi p_x + \mathbf{r}_\perp \cdot \mathbf{p}_\perp) \\ z(\tilde{V}\xi p_x + \mathbf{r}_\perp \cdot \mathbf{p}_\perp) \end{pmatrix}, \quad (4.18)$$

$$\mathbf{E} \times \mathbf{B} = \frac{1}{16} \begin{pmatrix} -|\mathbf{r}_\perp|^2 \\ \tilde{V}\xi y \\ \tilde{V}\xi z \end{pmatrix}, \quad (4.19)$$

$$\mathbf{B} \times (\mathbf{B} \times \mathbf{v}) = -\frac{1}{16\gamma} \begin{pmatrix} p_x |\mathbf{r}_\perp|^2 \\ y \mathbf{r}_\perp \cdot \mathbf{p}_\perp \\ z \mathbf{r}_\perp \cdot \mathbf{p}_\perp \end{pmatrix}. \quad (4.20)$$

For high electron energies  $p_x \approx \gamma$ ,  $\gamma \gg |\mathbf{p}_\perp|$ , and  $|\mathbf{p}_\perp| \gg 1$ . Thus the terms in  $\mathbf{G}$  simplify to

$$\gamma \left[ \frac{d\mathbf{E}}{dt} + \mathbf{v} \times \frac{d\mathbf{B}}{dt} \right] \approx \frac{1}{4\gamma} \begin{pmatrix} -|\mathbf{p}_\perp|^2 \\ 2\gamma p_y \\ 2\gamma p_z \end{pmatrix}, \quad (4.21)$$

$$\frac{\mathbf{p}}{\gamma} \gamma^2 (\mathbf{E} + \mathbf{v} \times \mathbf{B})^2 \approx \frac{\mathbf{p}}{16\gamma} [\tilde{V}^2 \xi^2 \gamma^2 + 4\gamma^2 |\mathbf{r}_\perp|^2], \quad (4.22)$$

$$\frac{\mathbf{p}}{\gamma} \gamma^2 (\mathbf{E} \cdot \mathbf{v})^2 \approx \frac{\mathbf{p}}{16\gamma} \tilde{V}^2 \xi^2 p_x^2, \quad (4.23)$$

$$\mathbf{E}(\mathbf{E} \cdot \mathbf{v}) = \frac{1}{16\gamma} \begin{pmatrix} \tilde{V}\xi(\tilde{V}\xi p_x + \mathbf{r}_\perp \cdot \mathbf{p}_\perp) \\ y(\tilde{V}\xi p_x + \mathbf{r}_\perp \cdot \mathbf{p}_\perp) \\ z(\tilde{V}\xi p_x + \mathbf{r}_\perp \cdot \mathbf{p}_\perp) \end{pmatrix}, \quad (4.24)$$

$$\mathbf{E} \times \mathbf{B} = \frac{1}{16\gamma} \begin{pmatrix} -\gamma |\mathbf{r}_\perp|^2 \\ \tilde{V}\xi \gamma y \\ \tilde{V}\xi \gamma z \end{pmatrix}, \quad (4.25)$$

$$\mathbf{B} \times (\mathbf{B} \times \mathbf{v}) = -\frac{1}{16\gamma} \begin{pmatrix} p_x |\mathbf{r}_\perp|^2 \\ y \mathbf{r}_\perp \cdot \mathbf{p}_\perp \\ z \mathbf{r}_\perp \cdot \mathbf{p}_\perp \end{pmatrix}. \quad (4.26)$$

In all these terms many different products occur. Some are composed by momenta solely, others only depend on spatial components. Many terms are canceling out and others vanish in their mean action on the charge, averaged over a betatron oscillation. The leading, non-vanishing term that is at least  $\gamma$ -times stronger than all other terms primarily determines the radiation reaction. As a consequence  $\mathbf{G}$  can be approximated by

$$\mathbf{G} \approx -\frac{\gamma}{4} \mathbf{r}_\perp^2 \mathbf{p} \quad (4.27)$$

and - written in terms of the classical Lorentz force - the equations of motion of an electron with ultra high energies in a co-moving frame of reference are

$$\frac{d\mathbf{r}}{dt} = \frac{\mathbf{p}}{\gamma} - V\vec{e}_x, \quad \frac{d\mathbf{p}}{dt} = - \left( \mathbf{E} + \frac{\mathbf{p}}{\gamma} \times \mathbf{B} \right) - \frac{\Lambda}{4} \mathbf{r}_\perp^2 \gamma \mathbf{p}. \quad (4.28)$$

In the next section the minimal energy spread of an externally injected and accelerated electron bunch in this model is analyzed and optimized. In the simulations it is assumed (i) that the bubble driver does not interact with the electron bunch; (ii) that the plasma background density is homogeneous; (iii) that the accelerated electrons do not interact. The electron bunches are side injected as in chapter 3.4. Different to that chapter, the following work does not focus on laser energies in the range  $E = 1J - 1kJ$  but will also discuss an application of MJ ( $E = 1kJ - 1MJ$ ) lasers to the bubble regime. In the following sections, three kind of simulation series are done. The first series is for the laser-plasma parameters  $E = 1 \dots 1000$  J,  $\lambda_{laser} = 600$  nm, and  $a_0 = 9$  which corresponds to a laser intensity of  $I = 6.2 \times 10^{20}$  W/cm<sup>2</sup>. With these parameters the bubble has a constant normalized radius of  $R_0 = 3.6$ . The variation of the other laser parameters is summarized in Tab.4.1. In the second series the laser intensity is  $I = 4.4 \times 10^{19}$  W/cm<sup>2</sup> which corresponds to  $a_0 = 4$  and the energy is varied from 1 kJ to 1MJ. The laser wave length  $\lambda_{laser} = 1 \mu\text{m}$  for these energies is adjusted to that of MJ laser systems[5, 96]. The variation of the other laser parameters is summarized in Tab.4.2. In the third and last series the dimensionless amplitude is  $a_0 = 64$  which corresponds to a laser intensity of  $I = 1.1 \times 10^{22}$  W/cm<sup>2</sup>. The energy is varied from 1 kJ to 1MJ and the laser wave length is  $\lambda_{laser} = 1 \mu\text{m}$  again. The variation of the other laser parameters is summarized in Tab.4.3.

### 4.3 Optimized injection under consideration of radiation re-action

In the last section the equations of motion for a test particle with the same mass and charge as an electron was derived. In this section the impact of the damping term on the optimal side injection is discussed. The simulations series are done for varying laser energies but fixed laser intensities and fixed laser wave lengths again (cmp. Ch.3). In addition the connection between the focal spot size  $R$  of the laser and the laser duration  $\tau$  is assumed to be  $\tau = R/c$  again.

The spatial simulation setup it the same as in the last chapter, so a cloud of not interacting test electrons (colored cloud in Fig.3.2a) is injected from side at an angle  $\alpha$  into a bubble. The bubble moves with velocity  $V = \sqrt{1 - 1/\gamma_0^2}$  in  $\xi$ -direction. The

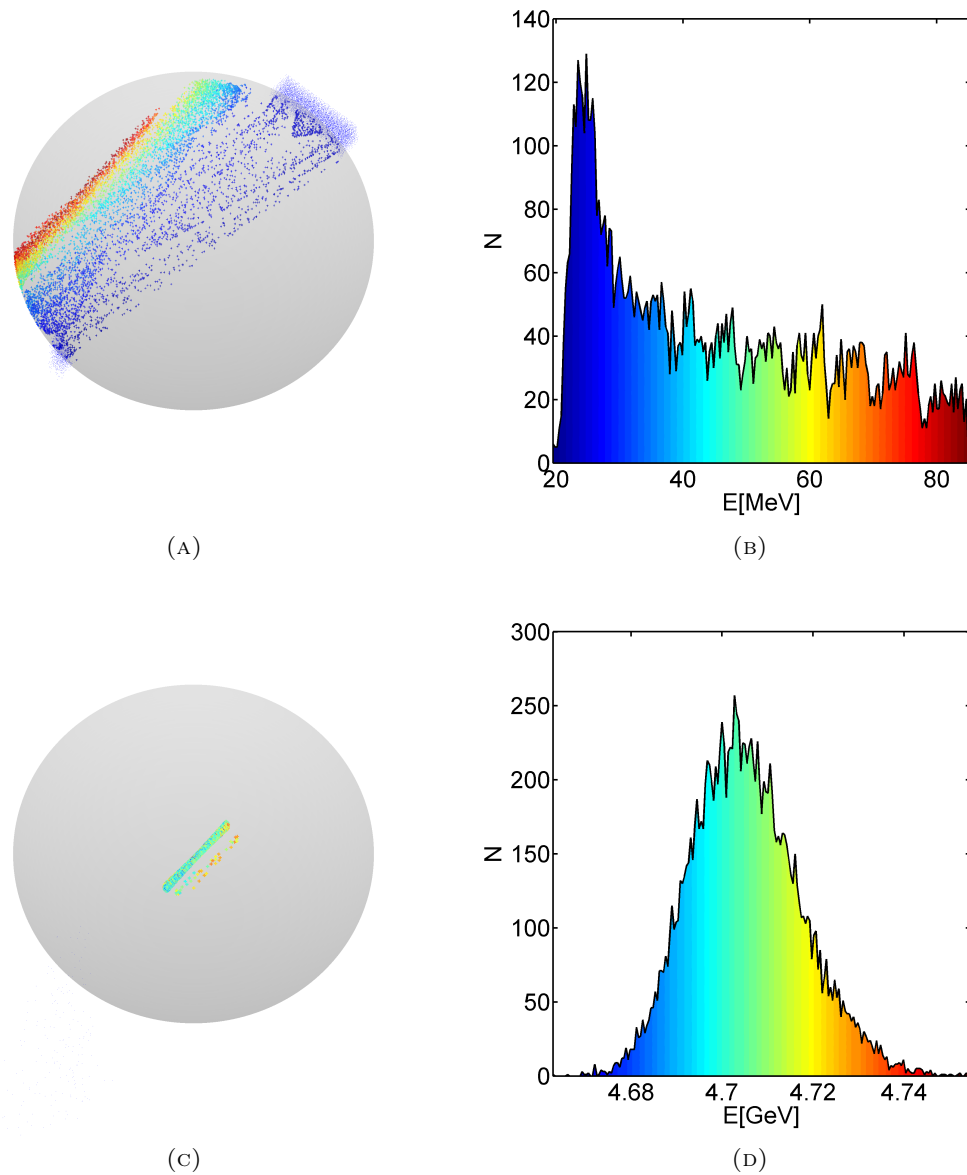


FIGURE 4.3: (a), (b): Injection process and corresponding energy spectrum. (c), (d): Electron bunch after injection and its spectrum with  $FWHM = 0.6\% \mu$  for  $E = 100J$ ,  $\lambda_{laser} = 600nm$ ,  $a_0 = 9$ .

initial momentum of every electron in the cloud is  $\mathbf{p}_0 = p_0(\cos(\alpha), -\sin(\alpha), 0)$ , where  $p_0 \sim N(\mu_0, 0.05\mu_0)$  is normal distributed and  $\mu_0 = 1.2\gamma_0$ . Thus, the initial energy distribution of the electron ensemble is a Gaussian as shown in Fig(3.2b). The initial position of the cloud is chosen such that its center of mass passes the point  $(0, R_0, 0)$  on the bubble border. The size of electron bunch is always  $a \times b \times b$ , where  $a = 0.5R_0$  and  $b = 0.25R_0$ . This ensures that all electrons in the bunch will be injected. Furthermore, the maximum sum of trapped electrons, the cut off angle, after which no electron is trapped, and the mean energy spread over all minimal energy spreads from simulations that could trap at least 50% of the bunch are analyzed. The equations of motion are solved for every

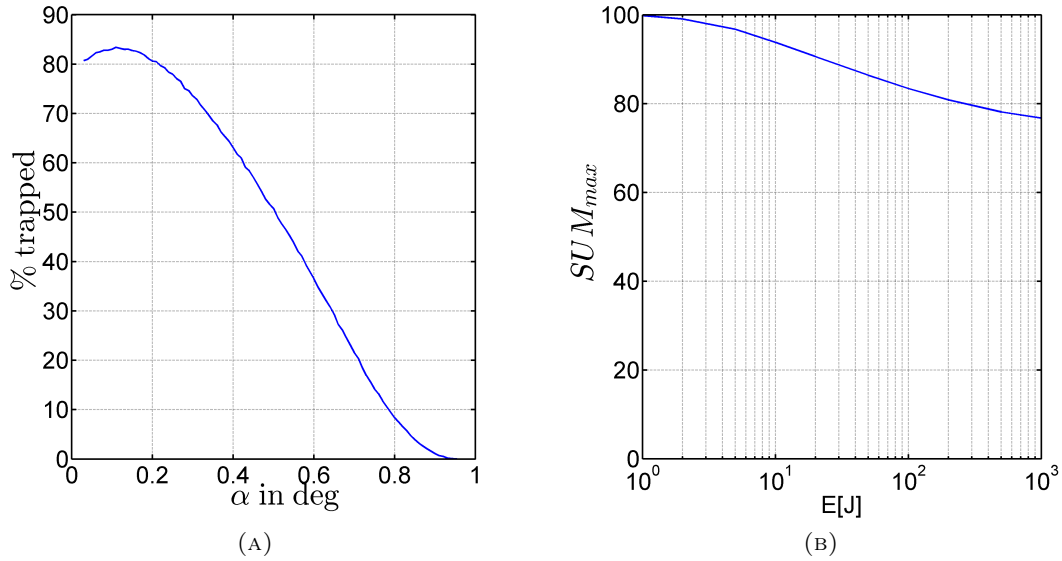


FIGURE 4.4: (a): Rel. number of trapped electrons vs incidence angle for  $E = 100J$ ,  $\lambda_{laser} = 600nm$ ,  $a_0 = 9$  in the radiation reaction model. (b): Maximal sum of trapped electrons vs laser energy in the radiation reaction model.

electron independently. However, in the simulations  $\mathbf{G}$  is not reduced as in Eq.(4.27) but linked to the QED parameter as

$$\mathbf{G} = -\frac{4\alpha^2}{9\Lambda^2}\chi^2\frac{\mathbf{p}}{\gamma} = -\frac{\mathbf{p}}{\gamma}[(\gamma\mathbf{E} + \mathbf{p} \times \mathbf{B})^2 - (\mathbf{E} \cdot \mathbf{p})^2]. \quad (4.29)$$

In this form,  $\mathbf{G}$  clearly reduces to the leading term in Eq.(4.27) but is also the limit of a QED radiation method that describes radiation in terms of Monte-Carlo simulations. Thus the here presented results can always be interpreted as the expected limit of Monte-Carlo simulations for  $\chi \ll 1$ .

In the first simulation series with the same laser plasma parameters as in the last section the additional damping terms has almost no influence. The injection process and the energy spectra at injection time are the same (see Fig.4.3a and 4.3b). The spatial distribution of the bunch after the acceleration in Fig.4.3c is identical focused as in the

$E_{laser}$ [J]	$P_{laser}$ [TW]	$E_{mono}$ [GeV]	$n_e/n_c$	$\tau$ [fs]	S	$R$ [ $\lambda_{laser}$ ]
1	120	0.24	$1.9 \times 10^{-2}$	8.3	$2.1 \times 10^{-3}$	4.2
10	560	1.1	$4.1 \times 10^{-3}$	18	$4.5 \times 10^{-4}$	9
100	2600	5.1	$8.7 \times 10^{-4}$	39	$9.7 \times 10^{-5}$	19
1000	12000	23	$1.9 \times 10^{-4}$	83	$2.1 \times 10^{-5}$	42

TABLE 4.1: Overview about the scaling of the laser-plasma parameter for the side injection method in the radiation reaction model with  $a_0 = 9$ ,  $\lambda_{laser} = 0.6 \mu m$ , and  $n_c = 3.1 \times 10^{21} \text{ cm}^{-3}$ .

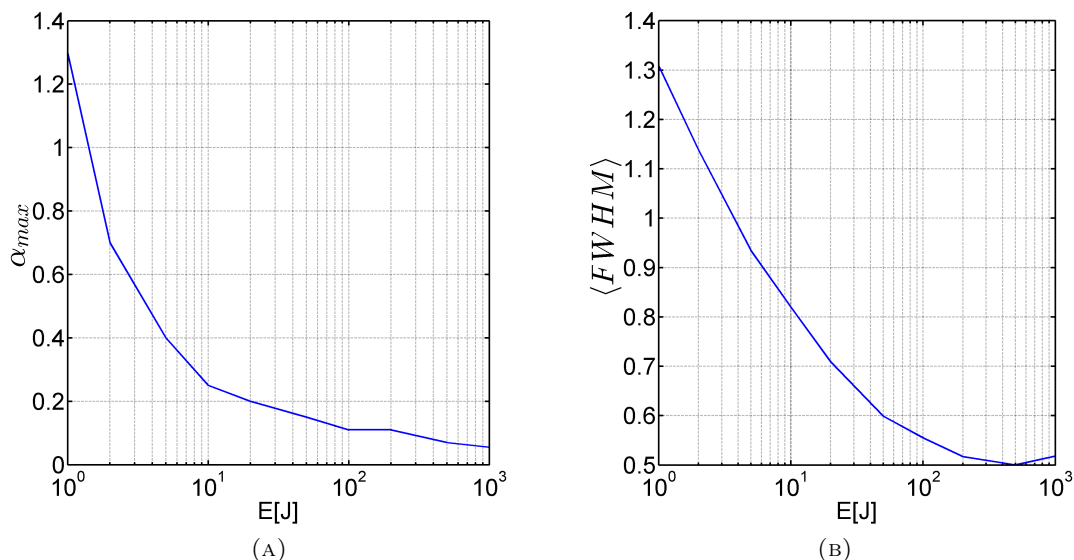


FIGURE 4.5: (a): Injection angle at which the maximal sum of trapped electrons is achieved in the radiation reaction model. (b): Mean FWHM of the energy spectra for different laser energies in the radiation reaction model. The mean value is calculated for all those spectra that contain at least 50% of all particles.

undamped case. The energy spectrum, however, shows a small difference. In the damped case in Fig.4.3d the mean energy is about 20 MeV smaller than in the undamped simulation in Fig.3.4b. Thus the bunch gained 0.4% less energy in the whole acceleration process for  $E = 100$  J.

The amount of trapped particles vs incident angle for  $E = 100$  J in Fig.4.4a shows that also the injection angle for laser energies in the range of 1 J to 1 kJ is comparable. As in the last section most electrons are trapped for small injection angles. The decrease of the number of trapped particles with growing angle is also similar to the case without radiation. The maximum amount of trapped electrons vs laser energy in Fig.4.4b clearly shows that it is always possible to trap more than 70% of all electrons. The number is slightly decreasing with increasing laser energy. The injection angle at which most electrons can be trapped depending on the laser energy in Fig.4.5a is again rapidly decreasing for low energies and slowly converging to zero for higher energies. The angles are in a close vicinity of the cut off angles after which no electron can be trapped.

The mean energy spread over all angles for which more than 50% of the injected electrons could be trapped -  $\langle FWHM \rangle$  - is strongly related to the laser energy (see Fig.4.5b). For low energies and relatively high injection angles  $\langle FWHM \rangle$  is in the range of 1% mean bunch energy. This is comparable to energy spreads from experiments with other injection methods [19–21, 65–73]. For increasing laser energies the mean energy spread decreases linearly until the minimum possible mean spread of about 0.5% is reached.

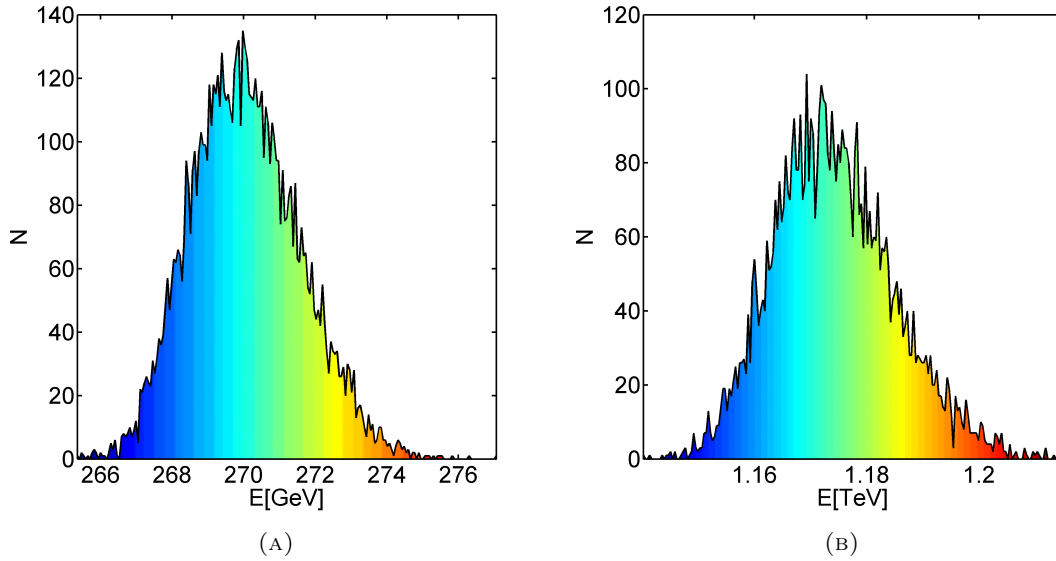


FIGURE 4.6: (a) Final spectrum from a simulation with  $FWHM = 2\% \mu$  for  $a_0 = 64$ . and (b) Final energy spectrum with  $FWHM = 2\% \mu$  from a simulation with  $a_0 = 4$ . In both simulations the laser energy is  $E = 1$  MJ and  $\lambda_{laser} = 1 \mu\text{m}$ .

When the minimum is reached the strong dependency to the laser energy disappears. It is possible to state that the energy spread is always in the bulk of 0.5% mean bunch energy if the laser energy is more than 100 J. This result differs to the found behavior in the last section where Fig.3.5b proved a further decrease of  $\langle FWHM \rangle$  with increasing energy. The reason for this observation is the additional radiation term in the equations of motion. Since the radiation lowers the maximum reachable bunch energy it also increases the minimum achievable energy spread. Additionally the absolute spread is enlarged. For energies in the range of 100 J to 1 kJ this broadening can be seen in a comparison between Fig.4.3d and Fig.3.4b. Here both spreads are Gaussian and the spectrum from the simulation without radiation reaction has a absolute width of 25 MeV. The spectrum from the simulation with radiation has an absolute spread of 30 MeV, this is 5 MeV or 20% more.

#### 4.4 Optimized side injection for ultra high energies and low intensities

In the second simulation series the laser energy goes beyond the 1 kJ limit. The laser intensity, however, is decreased to  $I = 4.4 \times 10^{19} \text{ W/cm}^2$  which corresponds to  $a_0 = 4$  and a normalized bubble radius of  $R_0 = 2.4$ . The laser wave length is  $\lambda_{laser} = 1 \mu\text{m}$  so that the parameters correspond to known laser parameters from MJ laser systems. The electron energies after acceleration could be in the TeV range if radiation effects did not

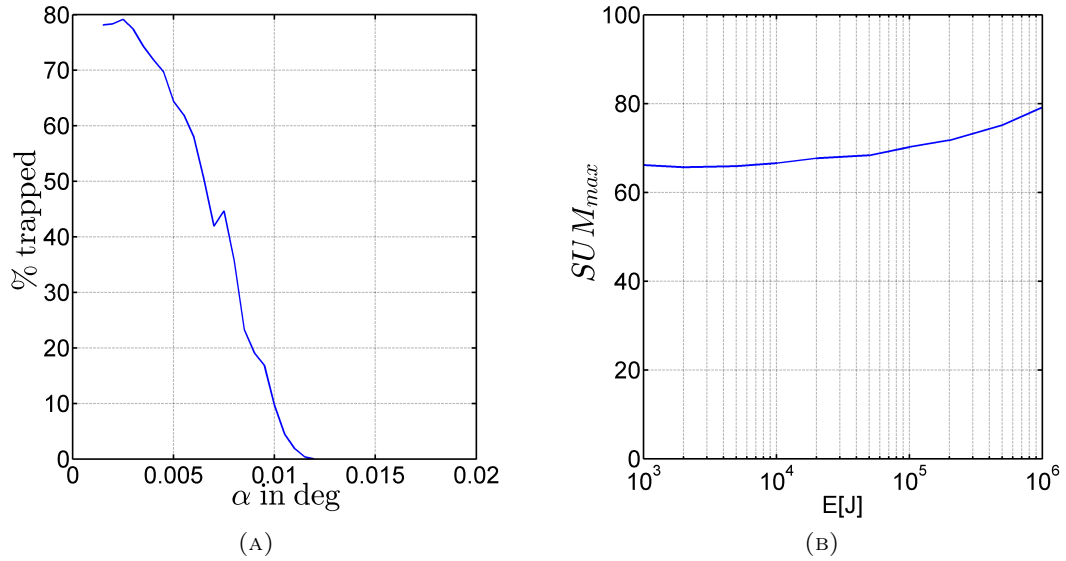


FIGURE 4.7: (a): Rel. number of trapped electrons vs incidence angle for  $E = 1$  MJ,  $\lambda_{laser} = 1000$  nm, and  $a_0 = 4$  in the radiation reaction model. (b): Maximal sum of trapped electrons vs laser energy in the radiation reaction model.

act. Since these high energies must be expected even with radiation reaction, the initial bunch energy before the injection is considered to be in the range of several hundred MeV so that the energy spread is 20% mean bunch energy again.

During the injection the bunch is fanned out and the energy spectrum is broadened. After the accelerated bunch has reached its maximal energy the spectrum is Gaussian again. The mean energy is in the bulk of 1.17 TeV and the spread is 25 GeV (see Fig.4.6b). Since the initial absolute spread and the absolute spread during the injection are more than ten times smaller, the additional radiation reaction term in the equations of motion seems not only to lower the maximum achievable energy but also broadens the absolute energy spread.

The reason why the spread after injection is as large as many GeV is the small injection angle that must be applied. For  $E = 1$  MJ the necessary injection angle is as small

$E_{laser}$ [kJ]	$P_{laser}$ [PW]	$E_{mono}$ [GeV]	$n_e/n_c$	$\tau$ [fs]	S	$R$ [ $\lambda_{laser}$ ]
1	5	22	$4.0 \times 10^{-5}$	200	$1 \times 10^{-5}$	60
10	23	100	$8.6 \times 10^{-6}$	430	$2.1 \times 10^{-6}$	130
100	110	470	$1.9 \times 10^{-6}$	930	$4.6 \times 10^{-7}$	280
1000	500	2200	$4.0 \times 10^{-7}$	2000	$1 \times 10^{-7}$	600

TABLE 4.2: Overview about the scaling of the laser-plasma parameter for the side injection method in the radiation reaction model with  $a_0 = 4$ ,  $\lambda_{laser} = 1$   $\mu\text{m}$ , and  $n_c = 1.1 \times 10^{21}$   $\text{cm}^{-3}$ .

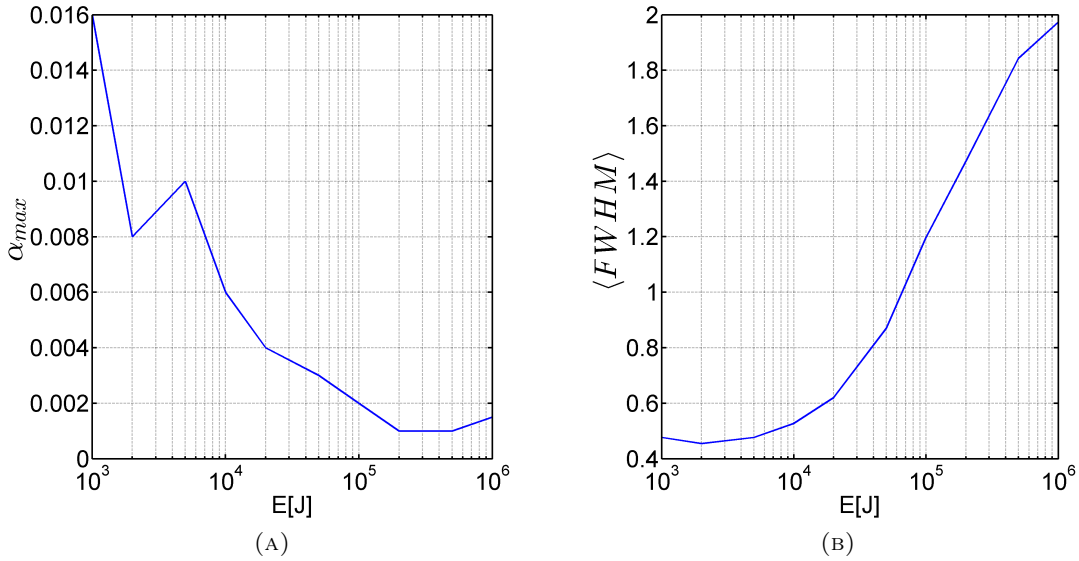


FIGURE 4.8: Simulation with  $E = 1 \text{ MJ}$ ,  $\lambda_{laser} = 1000 \text{ nm}$ , and  $a_0 = 4$  in the radiation reaction model. (a): Injection angle at which the maximal sum of trapped electrons is achieved. (b): Mean FWHM of the energy spectra for different laser energies in the radiation reaction model. The mean value is calculated for all those spectra that contain at least 50% of all particles.

as 0.01 deg. To reach the maximum amount an even ten times smaller injection angle is required. For  $E = 1 \text{ MJ}$  the number of trapped electrons is shown in Fig.4.7a. As in all previous simulation series the number of trapped electrons strongly decreases for increasing injection angles. Different is that the angles are very small while the bubble radius is in the same order.

The maximum amount of trapped electrons vs laser energy at these small angles is shown in Fig.4.7b. Here, the maximum is always above 60% and slightly increasing for higher energies. Different to the low energy cases is that the maximum does not go over the 80% mark. At these small angles it is hard to distinguish between the optimal injection angle to trap many electrons as possible and the cut off angle. Both converge rapidly to zero which also affects the mean energy spread.

In Fig.4.8a the injection angles at which most electrons could be trapped are plotted against the applied laser energy. The resulting graph starts at angles that are as small as the those from the last simulation series for  $E = 1 \text{ kJ}$ . Then the graph decreases steadily but it does not seem to converge to zero. The graph of the mean energy spread over all angles for which more than 50% of the injected electrons could be trapped begins where the graph from the last series ends (see Fig.4.5b). Then the  $\langle FWHM \rangle$  stays at the 0.5% level until  $E$  reaches 10 kJ. For higher energies  $\langle FWHM \rangle$  increases linearly until the maximum at  $E = 1 \text{ MJ}$  is reached.

The dominant reasons that lead to this development are the small injection angles and the broadening of the energy spreads. Due to the small angles the time the bunch needs to be injected - the injection time - is large and those electrons that are accelerated first experience the action of the radiation stronger. Due to the spatial concentration of the beam load it is solely the energy difference between the electrons that determines radiation and since the radiation is proportional to the square of the energy, the energy spread is broadened with increasing mean energy. The only possibility to hold down the growth of the energy spread with increasing laser energy is to enlarge the injection angle. This, however, is difficult because the low injection angles result from the fact that the bunches are injected at energies that are higher than maximum bunch energies from other experiments and simulations.

## 4.5 Optimized side injection for ultra high energies and high intensities

The next simulation series discusses the side injection for energies in the range  $E = 1$  kJ to  $E = 1$  MJ and a thousand times higher intensity of  $I = 1.1 \times 10^{22}$  W/cm<sup>2</sup> which corresponds to  $a_0 = 64$  and a normalized bubble radius of  $R_0 = 9.6$ . The laser wave length is  $\lambda_{laser} = 1$   $\mu$ m again. The expected electron energies after acceleration are well below the TeV limit if radiation effects did not act. Since these energies are much lower than in the previous simulation series, the initial bunch energy before the injection does not need to be in the range of several hundred MeV but rather in the range of 50 MeV to 200 MeV. The energy spread is 20% mean bunch energy again.

During the injection the bunch is fanned out across the whole bubble volume which is now three times larger than in the previous ones. After the accelerated bunch has reached its maximal energy the spectrum is Gaussian again. The mean energy is in the bulk of 270 GeV and the spread is 4 GeV (see Fig.4.6a). This time the initial absolute spread is more than a hundred times smaller but the absolute spread during the injection is more than two times larger. Thus the additional radiation reaction term in the equations of

$E_{laser}$ [kJ]	$P_{laser}$ [PW]	$E_{mono}$ [GeV]	$n_e/n_c$	$\tau$ [fs]	S	$R [\lambda_{laser}]$
1	32	8.6	$2.6 \times 10^{-2}$	32	$4 \times 10^{-4}$	10
10	150	40	$5.6 \times 10^{-3}$	68	$8.7 \times 10^{-5}$	20
100	680	190	$1.2 \times 10^{-3}$	150	$1.9 \times 10^{-5}$	44
1000	3200	870	$2.6 \times 10^{-4}$	320	$4 \times 10^{-6}$	95

TABLE 4.3: Overview about the scaling of the laser-plasma parameter for the side injection method in the radiation reaction model with  $a_0 = 64$ ,  $\lambda_{laser} = 1$   $\mu$ m, and  $n_c = 1.1 \times 10^{21}$  cm<sup>-3</sup>.

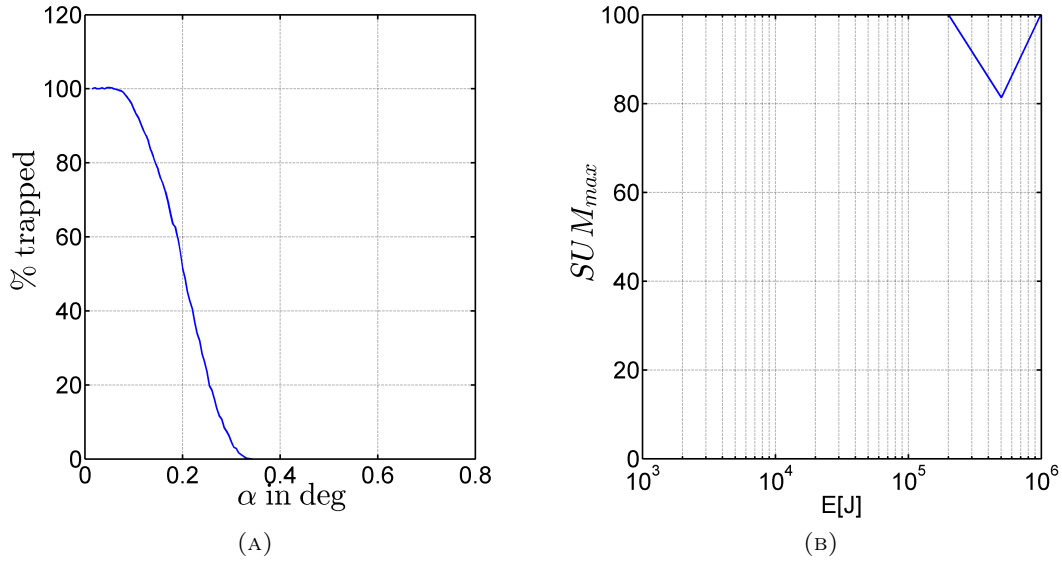


FIGURE 4.9: (a): Rel. number of trapped electrons vs incidence angle for  $E = 1$  MJ,  $\lambda_{laser} = 1000$  nm, and  $a_0 = 64$  in the radiation reaction model. (b): Maximal sum of trapped electrons vs laser energy in the radiation reaction model.

motion does lower the maximum achievable energy but has not the same effect on the energy spread than in the last low intensity simulation series.

The reason why the spread after injection is again in the range of some GeV is the small injection angle that must be applied. This times the angles are by far not that small as in the last series but still small against those from the first series with lower energies. For  $E = 1$  MJ the necessary injection angle must be chosen as small as 0.3 deg to trap at least some electrons. To reach the maximum amount a three times smaller injection angle is required. For  $E = 1$  MJ the number of trapped electrons is shown in Fig.4.9a. As in all previous simulation series the number of trapped electrons strongly decreases for increasing injection angles. Different is that the angles are between those from the last series while the bubble radius is now the largest.

The maximum amount of trapped electrons vs laser energy is shown in Fig.4.9b. Here, the maximum is almost always 100%. An explanation for this curious effect is shown in Fig.4.9a where the graph converges to 100% for small angles. This is different to the last simulation series where the number of trapped particles decreases again after the optimal injection angle. An explanation why the present series show a complete different behavior is the large bubble radius combined with radiation effects so that injected electrons have enough space to oscillate and can radiate a sufficient amount of radial momentum at the same time.

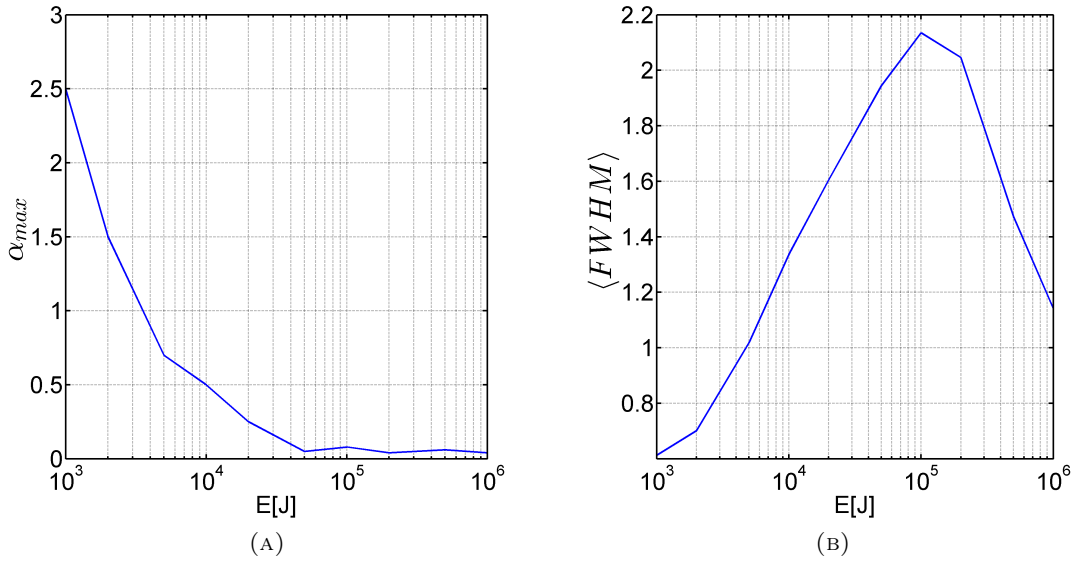


FIGURE 4.10: Simulation with  $E = 1$  MJ,  $\lambda_{laser} = 1000$  nm, and  $a_0 = 64$  in the radiation reaction model. (a): Injection angle at which the maximal sum of trapped electrons is achieved. (b): Mean FWHM of the energy spectra for different laser energies in the radiation reaction model. The mean value is calculated for all those spectra that contain at least 50% of all particles.

The injection angle at which the maximum number of electrons is trapped is somewhere between the angle at which the graphs similar to Fig.4.9b begin to converge to 100% and the minimum applied angle. In Fig.4.10a the injection angles at which most electrons could be trapped are plotted against the applied laser energy. The resulting graph starts at angles that are much larger than those from last section and much larger than those from the last simulation series for  $E = 1$  kJ. Then the graph decreases steadily and converge to zero. The graph of the mean energy spread over all angles for which more than 50% of the injected electrons could be trapped begins where the graph from the last series ends (see Fig.4.5b). Then  $\langle FWHM \rangle$  increases immediately linear until a maximum is reached. For higher energies  $\langle FWHM \rangle$  decreases again but stays always well above the 1% level.

Now that a qualitative analysis of the side injection method under consideration of radiation reaction has shown that larger laser intensities lead to lower particle energies but to higher trapping rates, it is important to understand the basic mechanism that leads to this effect. Since it is the radiation of energy that is responsible for the observed phenomena the next section gives an analytical estimate of the radiated energy in transversal and forward direction and explains why larger laser intensities are better suited to accelerate electrons in the far GeV bubble regime.

## 4.6 Analytical estimate of radiated energy

If the equations of motion are solved for a single test electron, the solution is the trajectory shown in Fig.4.1b. Here, the electron oscillates fast around the  $\xi$ -axis and approaches the bubble center slowly. The fast oscillations are well known betatron oscillations that are also seen in experiments [20, 26, 27]. To estimate the amount of radiated energy during the acceleration the following calculations estimate the radially emitted energy and the forward radiation by averaging over a betatron oscillation.

Similar to the last chapter the center of mass acceleration can be approximated by a guiding center approximation for times near the critical time  $t_{max}$  with  $\max p_{||}(t) = p_{||}(t_{max})$ . The guiding center approximation takes only the mean displacement of an electron from the  $\xi$ -axis into account. This, however, is zero and the differential equation system for  $\xi(t)$  and  $p_{||}(t)$  in terms of  $\tau = t - t_{max}$  and  $\rho = |\mathbf{r}_{\perp}|$  becomes

$$\frac{dp_{||}}{d\tau} = -(1+V)\frac{\xi}{4} - \frac{\Lambda}{4}\rho^2\gamma p_{||}, \quad \frac{d\xi}{d\tau} = \frac{p_{||}}{\gamma} - V \approx \frac{1}{2\gamma_0^2} - \frac{1+\mathbf{p}_{\perp}^2}{2\gamma^2}. \quad (4.30)$$

Since the energy of the electro is maximal for  $\tau = 0$  and since the maximum reachable energy is much larger than the transversal energy, the velocity  $d\xi/d\tau$  is nearly constant in a wide range of the bubble. The solutions to Eq.(4.30) are then deduced from the initial conditions  $\xi(\tau = 0) = \xi_0$  and  $\gamma(\tau = 0) = \gamma_{max}^{RR}$  [cmp. Fig.4.11a] by simply integrating

$$\xi(\tau) = \xi_0 + \frac{1}{2\gamma_0^2}\tau, \quad \gamma(\tau) \approx p_{||}(\tau) = \gamma_{max}^{RR} - \frac{(1+V)}{16\gamma_0^2}\tau^2. \quad (4.31)$$

Here  $dp_{||}(\tau)/d\tau = d\gamma(\tau)/d\tau = 0$ ,  $\langle \rho \rangle \equiv 0$ , and  $\langle \mathbf{p}_{\perp} \rangle \equiv 0$  for high energies (see Fig.4.11b) was used so that the radiation reaction force  $G_x$  has no influence at this level of accuracy. The position at which the maximal energy is reached, however, does depend on  $G_x$  and can be calculated from the maximum energy and the beam waist radius  $\rho_0$  via

$$\frac{dp_{||}(\tau)}{d\tau} = 0 \quad \Rightarrow \quad \xi_0 \approx -\frac{\Lambda}{1+V}\rho_0^2(\gamma_{max}^{RR})^2. \quad (4.32)$$

Since  $\xi_0 \leq 0$  radiation damping always decreases the effective acceleration length. Due to the extremely small damping factor  $\lambda$ , which is usually in the order of  $10^{-9}$  to  $10^{-10}$ , this additional energy gain limiting effect is important for very high electron energies in the far GeV regime solely.

The time-independent notation of the test electron energy

$$\gamma(\xi) = -\frac{(1+V)}{4}\gamma_0^2(\xi - \xi_0)^2 + \gamma_{max}^{RR}. \quad (4.33)$$

shows that the evolution of the damped particle energy can be modeled as a shifted parabola. The vertex is, in contrast to the side injection without radiation reaction, not only shifted along the energy axis but also to the left. Since  $\xi_0$  is proportional to  $\gamma_{max}^2$  all vertices lie on a parabola through the vertex of the undamped energy curve with  $\xi_0 = 0$  and  $\gamma_{max}^0 > \gamma_{max}^{RR}$ .

According to Fig.4.11b the envelop oscillation amplitude of the betatron oscillation around the  $\xi$  axis changes very slowly. Thus the shift from the axis can be modeled as

$$\rho(\tau) = \rho_0 \sin(\omega_\beta \tau), \quad \rho'(\tau) = \frac{p_\perp}{\gamma} = \rho_0 \omega_\beta \cos(\omega_\beta \tau). \quad (4.34)$$

In general the betatron oscillation is  $\omega_\beta = \omega_p / \sqrt{2\gamma}$  [97–99] and the characteristic time  $\propto 1/\omega_\beta$  is short enough to assume that  $\gamma$  is quasi constant in a period. Within the current normalization of variables the betatron frequency is  $\omega_\beta = 1/\sqrt{2\gamma}$  and the transversally radiated energy during one oscillation is

$$\langle E_\perp \rangle = \int_0^{2\pi\sqrt{2\gamma}} \lambda G_\perp |d\rho| \approx \lambda \gamma^2 \int_0^{\sqrt{2\gamma}\pi/2} (\rho(\tau))^2 (\rho'(\tau))^2 d\tau. \quad (4.35)$$

With Eq.(4.34) the anti derivative of the integral is proportional to  $\tau$  and  $\sin(4\omega_\beta \tau)$ . Thus the transversally radiated energy after one period is

$$\langle E_\perp \rangle \approx \lambda \omega_\beta^2 \gamma^2 \rho_0^4 \frac{\sqrt{2\gamma}\pi}{16} = \frac{\lambda\pi}{16\sqrt{2}} \rho_0^4 \gamma^{3/2}. \quad (4.36)$$

The longitudinally radiated energy during one oscillation is

$$\langle E_\parallel \rangle = \int_0^{2\pi\sqrt{2\gamma}} \lambda G_\parallel |d\xi| \approx \frac{\lambda\gamma^2}{2\gamma_0^2} \int_0^{\sqrt{2\gamma}\pi/2} (\rho(\tau))^2 d\tau. \quad (4.37)$$

With Eq.(4.34) the anti derivative of the integral is proportional to  $\tau$  and  $\sin(2\omega_\beta \tau)$ . Thus the forward radiated energy after one period is

$$\langle E_\parallel \rangle \approx \frac{\lambda\gamma^2}{2\gamma_0^2} \rho_0^2 \frac{\sqrt{2\gamma}\pi}{4} = \frac{\lambda\pi}{4\sqrt{2}} \frac{\rho_0^2}{\gamma_0^2} \gamma^{5/2}. \quad (4.38)$$

A first result from these considerations is that a side injected electron will radiate more energy while it is trapped than another electron with same energy that is injected into a smaller bubble. In the simulations from the last two sections the bubble radii differ by a factor of 4 while the injection energies are 6 times smaller for those electrons that are injected into the larger bubble. In affect the slower electron radiates more than ten times

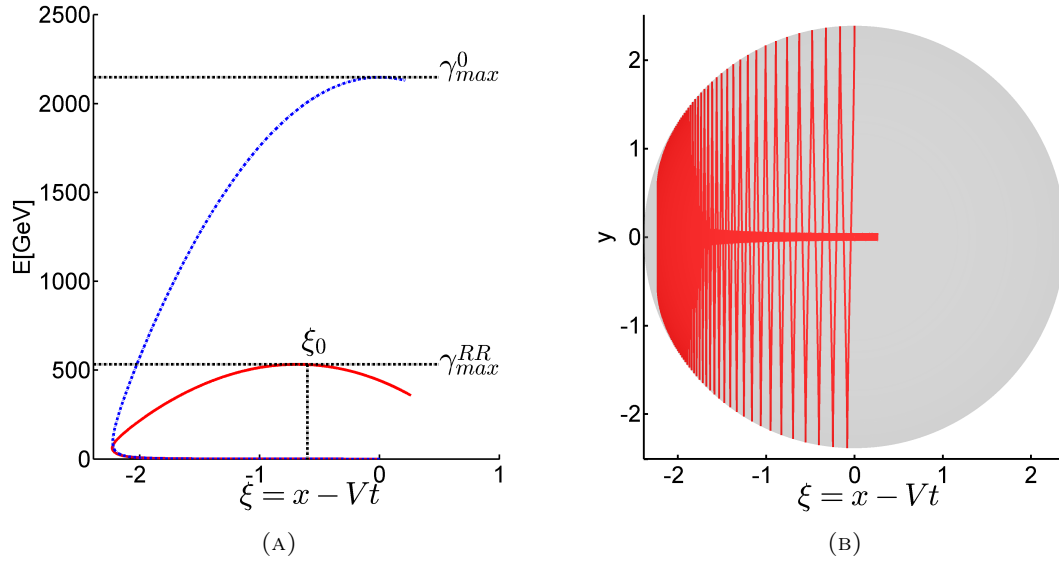


FIGURE 4.11: Comparison of energy gain with and without radiation reaction effects in a simulation with  $a_0 = 4$ ,  $\lambda_{laser} = 1 \mu\text{m}$ , and  $E = 1 \text{ MJ}$ . (a): Phase space plot of a simulation with RR (red line) and without RR (blue line). (b): Fast oscillation of a trapped electron in a simulation with RR.

more energy during the injection process and thus can be injected at an at least ten times larger angle. A comparison of Fig.4.7a and Fig.4.9a confirms this general statement.

If the oscillation number  $n$  is interpreted as a continuous variable - which is possible because the actual shift in  $\xi$ -direction is extremely small during one period - it is

$$\frac{d\xi(n)}{dn} = \frac{\xi_{n+1} - \xi_n}{(n+1) - n} = \frac{\pi\sqrt{2\gamma_n}}{\gamma_0^2} \quad (4.39)$$

where  $\xi_{n+1} = \xi_n + \pi\sqrt{2\gamma_n}/\gamma_0^2$  and  $\gamma_n = \gamma(\xi_n)$ . The total radiated energy during the acceleration is

$$E_{rad} = \sum_n E_n = \sum_n E_n \Delta n = \int E_n dn = \int_{-R}^{\xi_0} E_n \frac{dn}{d\xi_n} d\xi_n \quad (4.40)$$

where  $E_n = \langle E_{||}(\gamma_n) \rangle + \langle E_{\perp}(\gamma_n) \rangle$ . Thus it is

$$E_{rad} = \int_{-R}^{\xi_0} \frac{\lambda\gamma_0^2}{32} \rho_0^4 \gamma d\xi + \int_{-R}^{\xi_0} \frac{\lambda}{8} \rho_0^2 \gamma^2 d\xi \quad (4.41)$$

and the connection to the estimated energy gain without radiation  $\gamma_{max}^0$  is given by  $\gamma_{max}^0 = \gamma_{max}^{RR} + E_{rad}$  which in turn determines  $\gamma_{max}^{RR}$  in terms of  $\xi_0$ ,  $\rho_0$ ,  $R$ , and  $\gamma_0$ .  $\xi_0$  is given by Eq.(4.32) and both  $R$  and  $\gamma_0$  are related to the laser plasma parameter via known scaling laws [1]. The envelop function  $\rho_0$  is quasi constant in a wide range of the

bubble and has its smallest value at  $\xi_0$ . Thus Eq.(4.41) gives a good lower limit for an estimation of the amount of radiated energy.

## 4.7 Conclusion

In this chapter the side injection and acceleration of electrons in the bubble regime under consideration of radiation is discussed. The radiation reaction is derived from a covariant formulation of the equation of motion to which a linear damping term is added. This term then is discussed and analyzed for high energies and the special form of the bubble fields that are given analytically.

It is shown that the mean FWHM as well as the trapping rate can be optimized if the injection angle is chosen small enough. An important conclusion of this chapter is that for laser energies  $E \geq 50J$  and small injection angles  $\alpha \approx \pi/180$  rad the minimal mean FWHM of the trapped electron bunches cannot be pushed under a limit of 0.5% of the actual bunch energy. At the same time, the ratio of trapped electrons stays well above 70% for all energies. The cut-off angle above which no electrons can be trapped is numerically reviewed in 3d bubble multi particle simulations and analytically evaluated in a reduced 2d model. The comparison shows that for laser energies  $E \geq 50J$  both angles are comparable but not for lower energies. Consequently, the side injection of electron bunches in the GeV-regime is a promising accelerating and focusing mechanism that will be a center of interest for the next time.

For higher laser energies the radiation reaction terms lead to a broadening of the energy spreads so that it is not possible to achieve less than 1% mean energy spread if the laser energy is above a certain limit. For small laser intensities in the bulk of  $I = 10^{19}$  W/cm<sup>2</sup> the limit is 100 kJ. For higher intensities the limit decreases so that in a simulation series with  $I = 10^{22}$  W/cm<sup>2</sup> the mean FWHM is well above 1% if the energy is higher than 10 kJ. The optimal injection angles at which most electrons can be trapped must be chosen very small for energies larger than 1 kJ and small intensities. For high intensities the optimal injection angles are in the same order of magnitude as for low energies and low intensities again.

In the last section of this chapter an analytical estimate of the radiated energy is calculated from a guiding center approximation to the damped single particle trajectory. It could be shown that higher laser energies need smaller injection angles than lower ones and that higher laser intensities allow higher injection angles than lower ones. The solution of the guiding center approximation also showed that for ultra-high electron

energies the effective acceleration length is reduced proportional to the expected energy maximum after acceleration.

In the present and the last chapter the only limiting factor for the electron acceleration is the - damping dependent - dephasing length. Another factor that appears in experiments and PIC simulations is the depletion length after which the driver of the bubble is consumed and the bubble breaks. Recent PIC simulations and bubble models suggest that it is possible that avoid depletion if the driver runs through a plasma channel. If the plasma density drops to zero at the acceleration axis the intern bubble fields gain an additional degree of freedom. The next chapter introduces two analytical models for electron bunch driven wake fields in arbitrary radially symmetric plasma channels.

Results from this chapter are/will be published in the following publications:

J. Thomas, O. Jansen , A. Pukhov, *Radiation effects on ultra-high electron energies in the bubble regime*, to be submitted

## Chapter 5

# Deep plasma channels for tunable bubble fields

### 5.1 Introduction

Plasma wake fields provide a feasible path for high gradient particle acceleration [8, 13, 34, 100, 101]. Especially efficient are the so called bubble regime of laser-plasma wake fields [10] and the blow out regime of electron bunch driven wake fields [102]. In the first case the laser intensity is high enough to expel all background plasma electrons from the first half of the plasma wave. In the blowout regime all electrons are expelled from a region behind a driving electro bunch. The left behind void of plasma ions is surrounded by a thin layer of expelled electrons and a weakly perturbed plasma. The ions pull the electrons back to the acceleration axis in about a plasma wave length  $\lambda = 2\pi c/\omega_p$ . Overshooting electrons then create the characteristic volume. The advantage of the hollowed region is that it has a transversely uniform accelerating field [14, 103] that helps to generate quasi-mono-energetic electron bunches readily registered in experiments [104].

Despite various analytical approaches to the bubble and the blow out regime, a self-consistent theoretical description is still missing. What has been developed so far is a similarity theory for the bubble regime [29], a non-linear theory for the blow out regime [16, 46, 103], and a phenomenological model of the bubble [14]. In the similarity theory the leading parameters for homogeneous background plasmas are the  $S$ -number  $S = n_e/an_c \ll 1$  and the pulse aspect ratio  $\Pi = c\tau/R \leq 1$ . Here,  $n_e$  is the plasma electron density and  $n_c = \pi/r_e\lambda_0^2$  is the critical plasma density for a laser pulse with the wavelength  $\lambda_0$ ,  $a = eE_0/mc\omega_0$  is the relativistically normalized laser field amplitude,  $\omega_0 = 2\pi c/\lambda_0$ , and  $r_e = e^2/mc^2$  is the classical electron radius.

So far, energy conservation arguments and massive 3D PIC simulations have been used to get optimal scaling laws for the bubble regime in homogeneous plasmas [1, 28]. A straight forward estimation assumed that the laser energy first is converted into the wake field and afterwards into kinetic (bunch) energy. A similar argumentation holds for the blow out regime where the energy of the driving bunch is converted to kinetic energy of trapped electrons. The energy transfer process is stable as long as the accelerated bunch is in the accelerating phase of the wake and as long as the driver has enough energy to drive the wake - otherwise the driver depletes. In a uniform plasma the depletion length of the laser is shorter than the dephasing length which limits the maximum electron energy gain. Furthermore, the interaction of the accelerated electrons with the laser pulse can broaden the energy spectrum of the bunch [97, 105].

A common tool to increase the depletion length of laser pulses are plasma channels. Originally, they are used to guide weakly relativistic pulses over distances much larger than the Rayleigh length  $Z_R = \pi R^2 / \lambda_0$  but a recent work suggests to use nearly hollow plasma channels to provide independent control over the focusing and accelerating forces. They considered a moderately relativistic laser pulse and a rectangular channel density profile [106–108].

A deep plasma channel that is (nearly) empty on-axis can strongly modify both the bubble fields, the laser dynamics, and the trapping. In this context a recent work that looks for laser-plasma parameters that maximize the energy of the accelerated electron bunch and that reduce the energy spread [109]. Here the use of a deep channel demonstrates an increased effective bubble phase velocity, an improved energy gain, a longitudinal field that has a plateau and allows for mono-energetic acceleration, and a strongly reduced focusing force. Furthermore, new bubble scaling laws and field distributions for the deep channel are derived. According to these new scaling laws ultra-short pancake-like laser pulses help to match the dephasing and depletion length and thus lead to ultra high energy gains of accelerated electrons. The lack of focusing in the channel eliminates the betatron resonance and thus leads to much sharper beam energy distributions.

In this chapter the analysis that lead to the above found advantages and scalings in deep channels is presented. The followed analysis is done for a driving electron bunch but can easily be transferred to the bubble regime if the potentials of the driver are replaced by the laser potential and if the time averaged (over a laser period) ponderomotive force is included into the equations of motion of single test electrons.

In the next section first the general form of the electric and the magnetic field in terms of charge density and current density are derived in a quasi-static, cylindrical approximation. Then section 5.3 introduces an analytical model for an electron beam driven blow out that follows these approximations. The model further assumes that the blow

out surrounding electron layer is infinitely thin and carries a surface current that corresponds to a current generated by those electrons that are blown out from the cavity. A major result of this section is the connection between the fields, the currents, and the densities that allows to model the densities according to given fields and conversely. The following section 5.4 introduces a finite electron layer model that allows the study of side injection physics and has the same general field-source connection as the first model. Section 5.5 gives a few important examples for fields and density profiles before the last section summarized the found results.

## 5.2 Potentials and fields in a wake field in a plasma channel

Since the broken wake field is moving with almost speed of light through the plasma, it is convenient to perform all analysis in a co-moving frame of reference. If the frame is moving with speed of light to the right the corresponding canonical transformation of variables is  $\xi = ct - z$ . In the following the fields, potentials, densities ect. inside the blow out are assumed to be quasi-static which means that the variables are not no explicit time dependent in the moving frame. With this approximation the differential operators in the moving frame system are

$$\frac{\partial}{\partial t} = \frac{\partial \xi}{\partial t} \frac{\partial}{\partial \xi} + \frac{\partial t}{\partial t} \frac{\partial}{\partial t} = c \frac{\partial}{\partial \xi} + \frac{\partial}{\partial t} \equiv \frac{\partial}{\partial \xi} \quad (5.1)$$

$$\frac{\partial}{\partial z} = \frac{\partial \xi}{\partial z} \frac{\partial}{\partial \xi} + \frac{\partial t}{\partial z} \frac{\partial}{\partial t} = -\frac{\partial}{\partial \xi} + \frac{1}{c} \frac{\partial}{\partial t} \equiv -\frac{\partial}{\partial \xi} \quad (5.2)$$

Due to the cylindrical symmetry it is helpful to express the spatial variables in cylindrical coordinates. Thus it is

$$x = r \cos(\varphi), \quad y = r \sin(\varphi), \quad \xi = \xi. \quad (5.3)$$

Furthermore, all gradients in  $\varphi$ -direction vanish as no variable explicitly depends on  $\varphi$  - which is a key property in the simplification of all following equations. The vector potential  $\mathbf{A}$  inside a bubble or blow out has no  $\varphi$ -component so that the magnetic field has only a  $\varphi$ -direction which corresponds to all jet found analytical solutions to wake fields in recent models. A list of all differential operators in the moving frame in these cylindrical coordinates is given in appendix A.

In the following all variables are normalized to the speed of light  $c$ , to the electron mass  $m_e$ , to the electron plasma frequency  $\omega_{pe} = (4\pi e^2 n_0 / m_e)^{1/2}$ , and to the plasma background density  $n_0$  via  $x \rightarrow x\omega_{pe}/c$ ,  $t \rightarrow t\omega_{pe}$ ,  $\mathbf{v} \rightarrow \mathbf{v}/c$ ,  $\mathbf{p} \rightarrow \mathbf{p}/(m_e c)$ ,  $\Phi \rightarrow e\Phi/(m_e c^2)$ , and  $\mathbf{E} \rightarrow \mathbf{E}/m_e c^2$ . All bubble potentials are expressed in terms of the vector

potential  $\mathbf{A}$  and the wake field potential

$$\Psi = \varphi - A_z. \quad (5.4)$$

In terms of these potentials and aboce mentioned simplifications the Lorenz gauge is

$$\frac{1}{r} \frac{\partial}{\partial r} (r A_r) = -\frac{\partial \Psi}{\partial \xi}. \quad (5.5)$$

and the normalized Poisson equations for  $\mathbf{A}$  and  $\Psi$  are calculated from the plasma density and the electron current. Both are also cylindrical symmetric which means that they are only depending on the distance to the symmetry axis.

$$\left( \frac{\partial^2}{\partial t^2} - \nabla^2 \right) A_i = J_i, \quad \left( \frac{\partial^2}{\partial t^2} - \nabla^2 \right) \varphi = \rho, \quad (5.6)$$

$$\Rightarrow \frac{1}{r} \frac{\partial}{\partial r} \left( r \frac{\partial A_z}{\partial r} \right) = -J_z, \quad \Rightarrow \frac{1}{r} \frac{\partial}{\partial r} \left( r \frac{\partial \Psi}{\partial r} \right) = -\rho + J_z. \quad (5.7)$$

In general the electro magnetic fields are related to the potentials via

$$\mathbf{E} = -\nabla \varphi - \frac{\partial}{\partial t} \mathbf{A}, \quad \mathbf{B} = \nabla \times \mathbf{A}. \quad (5.8)$$

In the present approximations they reduce according to Eq.(A.7) to

$$\mathbf{E} = E_r \vec{e}_r + E_z \vec{e}_z = -\nabla \Psi - \nabla A_z - \frac{\partial \mathbf{A}}{\partial \xi}, \quad \mathbf{B} = B_\varphi \vec{e}_\varphi = - \left( \frac{\partial A_r}{\partial \xi} + \frac{\partial A_z}{\partial r} \right) \vec{e}_\varphi. \quad (5.9)$$

Thus the only non-vanishing coefficient functions of the electric and magnetic field inside the blowout are

$$E_z = \frac{\partial \Psi}{\partial \xi}, \quad E_r = -\frac{\partial \Psi}{\partial r} - \frac{\partial A_r}{\partial \xi} - \frac{\partial A_z}{\partial r}, \quad B_\varphi = -\frac{\partial A_r}{\partial \xi} - \frac{\partial A_z}{\partial r}. \quad (5.10)$$

### 5.3 The $\delta$ -layer model

In this section an analytical model for the blow out regime is introduced. In this model the assumptions and notations from the previous chapter are valid because the driving electron bunches usually have energies in the GeV regime so that their gamma factor is in the bulk of 100 to 1000. The blow out sheath is modeled as an infinitely thin layer because this section does not treat any injection techniques. What is treated, however, is a case sensitive partition of the interior potentials and fields. The cases in turn guaranty that the potentials and fields are reasonable. The electron density  $\rho_e$  and the  $\xi$ -coordinate of the electron current-density  $J_e$  both split up to distinguish between the driving and

the accelerated electron bunch. For simplicity the driver densities are assumed to be constant, i.e. there are no gradients in the driver density. The volume which is occupied by the driver is modeled as a cylinder with high  $l_e$  and radius  $r_e$ . The densities inside the accelerated bunch are given in a more general way so that they depend on  $\xi$  and  $r$ . The volume of the beam load is also modeled as a cylinder with high  $l_{ee}$  and radius  $r_{ee}$ . In terms of the coordinated  $\xi_e$  (starting point of the driver) and  $\xi_{ee}$  (starting point of the beam load) the densities can be written as

$$\rho_e = J_e = \begin{cases} J_0, & r < r_e, \quad \xi_e < \xi < \xi_e + l_e \\ j_a(\xi, r), & r < r_{ee}, \quad \xi_{ee} < \xi < \xi_{ee} + l_{ee} \\ 0, & \text{else} \end{cases} \quad (5.11)$$

The source term for the charge density  $\rho$  and the current  $\xi$ -coordinate  $J_z$  obeys the cylinder symmetric density profile for the channel and models the surrounding sheath by a delta distribution. Since the source is cylinder symmetric inside the blow out it only depends on the distance to the symmetry axis. Inside the sheath, however, the source depends only on the  $\xi$ -coordinate so that all currents in the sheath have no angular component.

$$S(\xi, r) = J_z - \rho = \begin{cases} s_i(r), & r < r_b(\xi) \\ s_0(\xi)\delta(r - r_b), & \text{else} \end{cases} \quad (5.12)$$

At this point it is important to mention that  $\rho$  is the sum of the electron density and the ion density  $\rho_i$ . Furthermore  $\mathbf{J}$  is the sum of the (local) electron current density and the ion current densities  $J_i$ . In terms of the sources above inside the blow out it is

$$\rho = \rho_e + \rho_i = j_a(\xi, r) + \rho_i \quad (5.13)$$

$$\mathbf{J} = J_z \vec{e}_z = (s_i(r) + \rho) \vec{e}_z = (j_a(\xi, r) + s_i(r) + \rho_i) \vec{e}_z \quad (5.14)$$

$$J_i = 0. \quad (5.15)$$

The radial component of the electron and ion current density does not vanish for a single electron but the sum of all radial currents inside the bunches vanishes in the average.

According to Eq.(5.11) the interior of the bubble can be separated into five zones (see Fig.5.1). The first (gray) zone describes the interior of the bubble that is free of electrons. The 2nd (light red) and 4th (light blue) zone are free of electrons too, but the potentials depend on the bunches. The last two zones are the inner domains of the bunches.

In the following subsections first the wake field potential  $\Psi$ , the vector potential  $\mathbf{A}$ , and the fields are calculated from the sources in all five zones. Afterwards, desired fields are

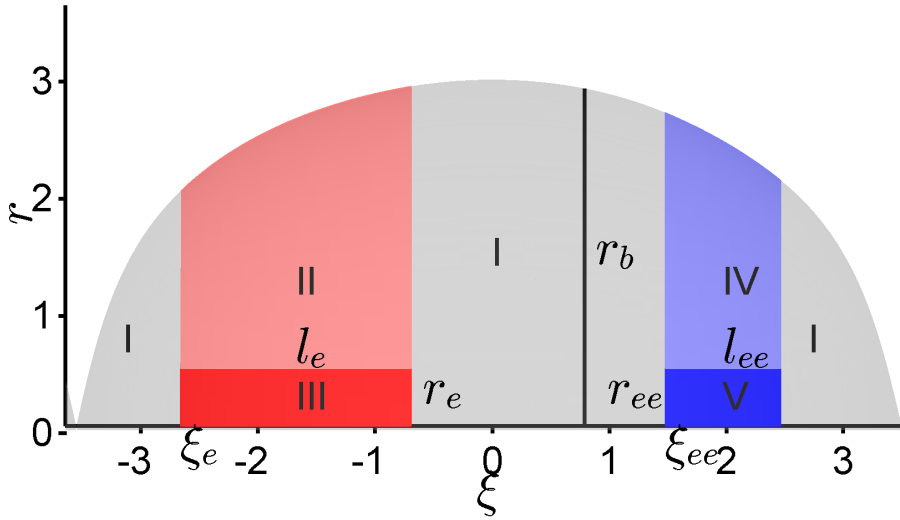


FIGURE 5.1: Five zones model of the blow out. Gray zone: empty zones, the electron bunches do not influence this zone; (II) Light red zone: also empty but the electromagnetic potential depends on the current from zone III; (III) Red zone: interior of the driving bunch; (IV) Light blue zone: empty but the electromagnetic potential depends on the current from zone V; (V) Blue zone: Interior of the accelerated electron bunch.

given and it is determined whether a  $J_z(\xi, r)$  and a  $s_i(r)$  existed that generate these fields. In both cases the bubble or blow out radius is assumed to be known from an ODE that is also derived in one subsection.

### 5.3.1 The potentials in terms of the sources

To determine the potentials in terms of the sources first the sheath source  $s_0(\xi)$  is calculated as a function of the blow out radius  $r_b(\xi)$ . Starting point will be the partial integration of the continuity equation in the cylindrical, quasi-static approximation under the consideration that  $J_r = 0$

$$\frac{\partial \rho}{\partial t} + \nabla \cdot \mathbf{J} = 0 \quad (5.16)$$

$$\Rightarrow \frac{\partial}{\partial \xi}(\rho - J_z) + \frac{1}{r} \frac{\partial}{\partial r}(r J_r) = 0 \quad (5.17)$$

$$\Rightarrow \frac{\partial}{\partial \xi}(\rho - J_z) = 0 \quad (5.18)$$

$$\Rightarrow \frac{\partial}{\partial \xi} \int_0^\infty S(\xi, r) r dr = 0 \quad (5.19)$$

$$\Rightarrow \int_0^{r_b} s_i(r) r dr + r_b(\xi) s_0(\xi) = -c_1 \quad (5.20)$$

Since the left hand side of Eq.(5.20) is independent from  $r$ , the integration constant is also and together with the integral source

$$S_I(r) = \int_0^r s_i(r')r' dr'. \quad (5.21)$$

the general solution for the sheath current source is  $s_0(\xi) = -[S_I(r_b(\xi)) + c_1]/r_b(\xi)$ . To determine  $c_1$  a boundary condition that is independent from  $r$  is necessary. Since  $S(r, \xi) = 0$  outside the boundary, it is convenient to demand the condition  $s_0(\xi(r_b = 0)) = 0$ . But since

$$\lim_{r_b \rightarrow 0} s_0(\xi(r_b)) = \lim_{r_b \rightarrow 0} \frac{S_I(r_b)}{r_b} \stackrel{v_H}{=} \lim_{r_b \rightarrow 0} \frac{s_i(r_b)r_b}{1} = 0, \quad (5.22)$$

$c$  must be zero too and it is

$$s_0(\xi) = -\frac{S_I(r_b(\xi))}{r_b(\xi)}. \quad (5.23)$$

This relation connects the inner and the outer source term so that the surface current equals the current that would be produced by all those electrons that are expelled from the volume inside the blow out or bubble.

To determine the wake field in terms of the inner source term the Poisson equation for  $\Psi$  in Eq.(5.7) and the model for the source in Eq.(5.12) are combined. Both give, after two partial integrations, two different solutions for  $\Psi(\xi, r)$

$$\Psi(\xi, r) = \int S_I(r) \frac{dr}{r} + c_2(\xi) \ln(r) + \Psi_0(\xi), \quad r < r_b(\xi), \quad (5.24)$$

$$\Psi(\xi, r) = [s_0(\xi)r_b(\xi) + c_3(\xi)] \ln(r) + c_4(\xi) \quad \text{else.} \quad (5.25)$$

The integration constants are deduced and simplified as follows:

1) The fields in the bubble interior are restricted  $\Rightarrow c_2(\xi) = 0$ .

2) The electric and the magnetic field vanish outside the boundary.

$$\frac{\partial}{\partial r} \Psi = 0 \quad \Rightarrow c_3(\xi) = -s_0(\xi)r_b(\xi), \quad \frac{\partial}{\partial \xi} \Psi = 0, \quad \Rightarrow c_4 = \text{const} \quad (5.26)$$

3)  $\Psi$  is continuous in  $r = r_b$ .

$$\int_{r=r_b} S_I(r) \frac{dr}{r} + \Psi_0(\xi) = c_4 \quad \Rightarrow \Psi_0(\xi) = c_4 - \int_{r=r_b} S_I(r) \frac{dr}{r} \quad (5.27)$$

If all terms are added together, the wake field potential can be written as

$$\Psi(\xi, r) = \int S_I(r) \frac{dr}{r} + \Psi_0(\xi) = \int S_I(r) \frac{dr}{r} - \int_{r=r_b} S_I(r) \frac{dr}{r} + c_4, \quad r \leq r_b(\xi), \quad (5.28)$$

$$\Psi(\xi, r) = 0 \quad \text{else.} \quad (5.29)$$

The electromagnetic potential  $\mathbf{A}$  can be derived in a similar way from the Poisson equation 5.7 and the Lorentz gauge 5.5. This time, however, the solutions will be presented by defined integrals so that no additional boundary condition is necessary.

Since the longitudinal component of the magnetic potential  $A_z$  only depends on the electron current in both the driving and the accelerated bunch  $J_e$ , the Poisson equation [see Eq.(5.7)] gives after partial integration

$$\frac{1}{r} \frac{\partial}{\partial r} \left( r \frac{\partial A_z}{\partial r} \right) = -J_z \quad \Rightarrow \quad A_z = - \int_0^r dr' \frac{r'}{r} J_z(\xi, r') \quad (5.30)$$

To determine the fields only terms proportional to  $\partial A_z / \partial r$  appear. Thus it is sufficient to derive all five derivatives. In terms of the integral current

$$J_A(\xi, r) = \int_0^r j_a(\xi, r') r' dr' \quad (5.31)$$

these can be expressed as

$$(I) \quad \frac{\partial A_z}{\partial r} = 0 \quad \text{else} \quad (5.32)$$

$$(II) \quad \frac{\partial A_z}{\partial r} = -\frac{J_0 r_e^2}{2 r} \quad r > r_e, \quad \xi_e < \xi < \xi_e + l_e \quad (5.33)$$

$$(III) \quad \frac{\partial A_z}{\partial r} = -\frac{J_0}{2} r \quad r \leq r_e, \quad \xi_e < \xi < \xi_e + l_e \quad (5.34)$$

$$(IV) \quad \frac{\partial A_z}{\partial r} = -\frac{J_A(\xi, r_{ee})}{r} \quad r > r_{ee}, \quad \xi_{ee} < \xi < \xi_{ee} + l_{ee} \quad (5.35)$$

$$(V) \quad \frac{\partial A_z}{\partial r} = -\frac{J_A(\xi, r)}{r} \quad r \leq r_{ee}, \quad \xi_{ee} < \xi < \xi_{ee} + l_{ee} \quad (5.36)$$

These five equations give the longitudinal electromagnetic potential component of the blow out potentials inside the cavity under the requirement that the potential does not diverge for small  $r$  and that it is continuous in  $r$ -direction. Outside the potential is set to zero so that the fields vanish again. Thus the  $A_z$  induced fields are discontinuous at the sheath.

The radial component  $A_r$  is calculated from the Lorentz gauge (5.5) and the wake field potential which is already known from Eq.(5.24)

$$\frac{1}{r} \frac{\partial}{\partial r} (r A_r(\xi, r)) = -\frac{\partial \Psi_0(\xi)}{\partial \xi} \quad \Rightarrow A_r(\xi, r) = -\frac{1}{2} r \frac{\partial \Psi_0(\xi)}{\partial \xi}. \quad (5.37)$$

### 5.3.2 Calculate the electron sheath current

To determine the electron current in the surrounding sheath it is necessary to solve the equations of motion of a test electron at positions  $r = r_b(\xi)$ . A simple method to do this could be to solve the equations of motion for a single electron inside the bubble in the moving frame of reference

$$\frac{d\mathbf{p}}{dt} = -\left(\mathbf{E} + \frac{\mathbf{p}}{\gamma} \times \mathbf{B}\right), \quad \frac{d\mathbf{r}_\perp}{dt} = \frac{\mathbf{p}_\perp}{\gamma} + \vec{e}_z \left(1 - \frac{p_z}{\gamma}\right). \quad (5.38)$$

in the limit  $r \rightarrow r_b$ . In the following, however, a differential equation that depends on the sources and  $r_b$  solely is derived. To achieve this first an expression for the change of the radial momentum due to a shift in  $\xi$ -direction inside the volume is calculated. Afterward the potentials are evaluated at the border.

Since trapped electrons perform betatron oscillations in a plain and since the energy gain of the accelerated electrons is coded in the longitudinal position, it is sufficient to split equations up into a radial part and a longitudinal part [also remember  $\vec{e}_r \times \vec{e}_\varphi = \vec{e}_z$  and  $\vec{e}_z \times \vec{e}_\varphi = -\vec{e}_r$ ]

$$\frac{dp_r}{dt} = -\left(E_r - \frac{p_z}{\gamma} B_\varphi\right), \quad \frac{dr}{dt} = \frac{p_r}{\gamma} \quad (5.39)$$

$$\frac{dp_z}{dt} = -\left(E_z + \frac{p_r}{\gamma} B_\varphi\right), \quad \frac{d\xi}{dt} = 1 - \frac{p_z}{\gamma}. \quad (5.40)$$

The angular part of the equations of motions does not contribute to the desired ODE.

The Hamiltonian  $H(\mathbf{p}, \mathbf{r}, t)$  for electrons in a quiescent plasma is one and since all potentials are time-independent,  $H$  is a constant of motion. The Hamiltonian of the system thus is [110]

$$H(\mathbf{p}, \mathbf{r}, t) = \gamma - \Pi_z - \varphi = \gamma - p_z - \Psi = 1, \quad (5.41)$$

where  $\vec{\Pi} = \mathbf{p} - \mathbf{A}$  is the canonical momentum and  $\gamma = \sqrt{1 + |\mathbf{p}|^2}$  is the electron energy. It follows from  $H = 1$  and Eq.(5.39) that

$$\frac{d\xi}{dt} = 1 - v_z = 1 - \frac{p_z}{\gamma} = \frac{1 + \Psi}{\gamma} \quad (5.42)$$

and

$$p_r = \gamma \frac{dr}{dt} = (1 + \Psi) \frac{dr}{d\xi}. \quad (5.43)$$

With Eq.(5.41) the energy can be written in terms of  $p_r$  and  $\Psi$  as

$$\gamma^2 = 1 + p_r^2 + p_z^2 \quad \Rightarrow \quad \gamma = \frac{1 + p_r^2 + (1 + \Psi)^2}{2(1 + \Psi)}. \quad (5.44)$$

Together with Eq.(5.42) this immediately gives

$$\frac{1}{1 - v_z} = \frac{\gamma}{1 + \Psi} = \frac{1 + p_r^2 + (1 + \Psi)^2}{2(1 + \Psi)^2}. \quad (5.45)$$

Adding together the relation between the fields and the potentials in the quasi-static approximation in cylindrical coordinates from Eqs.(5.10), (5.39), (5.40), and (5.42) the change of the radial momentum due to a shift in  $\xi$ -direction inside the volume is

$$\frac{dp_r}{d\xi} = -\frac{1}{1 - v_z} (E_r - v_z B_\varphi) \quad (5.46)$$

$$\Rightarrow \frac{dp_r}{d\xi} = -\frac{1}{1 - v_z} \left( -\frac{\partial \Psi}{\partial r} - \frac{\partial A_r}{\partial \xi} - \frac{\partial A_z}{\partial r} + v_z \frac{\partial A_r}{\partial \xi} + v_z \frac{\partial A_z}{\partial r} \right) \quad (5.47)$$

$$\Rightarrow \frac{dp_r}{d\xi} = \left[ \frac{1 + p_r^2 + (1 + \Psi)^2}{2(1 + \Psi)^2} \right] \frac{\partial \Psi}{\partial r} + \frac{\partial A_z}{\partial r} + \frac{\partial A_r}{\partial \xi} \quad (5.48)$$

To prepare an ODE for test electrons in the sheath this equation must be expressed in terms of the sources and  $r_b$  solely. Thus in the next steps  $\Psi$  and  $\mathbf{A}$  and their derivatives are evaluated at the sheath border. Here the potentials and their derivatives are

$$\Psi(\xi, r = r_b) = \int_{r=r_b} S_I(r) \frac{dr}{r} + \Psi_0(\xi) = c_4, \quad (5.49)$$

$$A_r(\xi, r = r_b) = r_b \sigma(\xi) \quad (5.50)$$

$$\frac{\partial \Psi}{\partial \xi} \Big|_{r=r_b} = \frac{d\Psi_0}{d\xi} = -\frac{S_I(r_b)}{r_b} \frac{dr_b}{d\xi}, \quad (5.51)$$

$$\frac{\partial \Psi}{\partial r} \Big|_{r=r_b} = \frac{S_I(r_b)}{r_b}, \quad (5.52)$$

$$\frac{\partial A_r}{\partial \xi} \Big|_{r=r_b} = r_b \frac{d\sigma}{d\xi} \quad (5.53)$$

$$\frac{A_z}{\partial r} \Big|_{r=r_b} = \begin{cases} \lambda(\xi)/r_b & \xi_e \leq \xi \leq \xi_e + l_e \\ J_A(\xi, r_{ee})/r_b & \xi_{ee} \leq \xi \leq \xi_{ee} + l_{ee} \end{cases} \quad (5.54)$$

$$\lambda(\xi) = -\frac{1}{2} J_0 r_e^2(\xi), \quad J_A(\xi, r_{ee}) = \int_0^{r_{ee}} j_a(\xi, r) r dr, \quad \sigma(\xi) = -\frac{1}{2} \frac{\partial \Psi_0(\xi)}{\partial \xi}. \quad (5.55)$$

Now Eq.(5.43) and (5.48) give the equation of motion for a test electron on the bubble border, i.e. for  $r = r_b$

$$\frac{d}{d\xi} \left[ (1 + \Psi) \frac{dr_b}{d\xi} \right] = \left[ \frac{1 + p_r^2 + (1 + \Psi)^2}{2(1 + \Psi)^2} \right] \frac{\partial \Psi}{\partial r} + \frac{\partial A_z}{\partial r} + \frac{\partial A_r}{\partial \xi} \quad (5.56)$$

$$\Rightarrow \frac{d\Psi(\xi)}{d\xi} \frac{dr_b}{d\xi} + (1 + \Psi) \frac{d^2 r_b}{d\xi^2} = \left[ \frac{1 + p_r^2 + (1 + \Psi)^2}{2(1 + \Psi)^2} \right] \frac{\partial \Psi}{\partial r} + \frac{\partial A_z}{\partial r} + \frac{\partial A_r}{\partial \xi} \quad (5.57)$$

If Eq.(5.57) is sorted with respect to derivations of  $r_b$  and if Eqs.(5.51) to (5.54) are substituted, the equation of motion can be expressed in form of a single ODE for the sheath radius  $r_b$

$$A(r_b) \frac{d^2 r_b}{d\xi^2} + B(r_b) \left( \frac{dr_b}{d\xi} \right)^2 + C(r_b) = \begin{cases} \lambda(\xi)/r_b & \xi_e \leq \xi \leq \xi_e + l_e \\ J_A(\xi, r_{ee})/r_b & \xi_{ee} \leq \xi \leq \xi_{ee} + l_{ee} \\ 0 & \text{else} \end{cases} \quad (5.58)$$

To determine the coefficient functions it is necessary to expand all potentials and abbreviating functions that were defined so far. For simplicity all terms that contribute to  $A(r_b)$  are marked red, all terms that contribute to  $B(r_b)$  are marked blue, and all terms that contribute to  $C(r_b)$  are marked green.

$$(i) \quad \frac{d\sigma}{d\xi} \stackrel{(5.55)}{=} -\frac{1}{2} \frac{d^2 \Psi_0}{d\xi^2} \stackrel{(5.27)}{=} \frac{1}{2} \frac{d}{d\xi} \left( \frac{S_I(r_b)}{r_b} \frac{dr_b}{d\xi} \right) \quad (5.59)$$

$$\Leftrightarrow \frac{d\sigma}{d\xi} \stackrel{(5.21)}{=} \frac{1}{2} \left( \frac{S_I(r_b)}{r_b} \frac{d^2 r_b}{d\xi^2} + \frac{s_i(r_b)r_b}{r_b} \left( \frac{dr_b}{d\xi} \right)^2 - \frac{S_I(r_b)}{r_b^2} \left( \frac{dr_b}{d\xi} \right)^2 \right) \quad (5.60)$$

$$(ii) \quad \frac{\partial A_r}{\partial \xi} \stackrel{(5.53)}{=} r_b \frac{d\sigma}{d\xi} \quad (5.61)$$

$$\Leftrightarrow \frac{\partial A_r}{\partial \xi} \stackrel{(5.60)}{=} \frac{S_I(r_b)}{2} \frac{d^2 r_b}{d\xi^2} + \frac{1}{2} \left[ s_i(r_b)r_b - \frac{S_I(r_b)}{r_b} \right] \left( \frac{dr_b}{d\xi} \right)^2 \quad (5.62)$$

$$(iii) \quad \frac{\partial \Psi}{\partial \xi} \frac{dr_b}{d\xi} \stackrel{(5.51)}{=} -\frac{S_I(r_b)}{r_b} \left( \frac{dr_b}{d\xi} \right)^2 \quad (5.63)$$

$$(iv) \quad (1 + \Psi) \frac{d^2 r_b}{d\xi^2} \stackrel{(5.51)}{=} (1 + c_4) \frac{d^2 r_b}{d\xi^2} \quad (5.64)$$

$$(v) \quad \left[ \frac{1 + p_r^2 + (1 + \Psi)^2}{2(1 + \Psi)^2} \right] \frac{\partial \Psi}{\partial r} \stackrel{(5.52)}{=} \left[ \frac{p_r^2}{2(1 + \Psi)^2} + \frac{1 + (1 + \Psi)^2}{2(1 + \Psi)^2} \right] \frac{S_I(r_b)}{r_b} \quad (5.65)$$

$$\Leftrightarrow \left[ \frac{1 + p_r^2 + (1 + \Psi)^2}{2(1 + \Psi)^2} \right] \frac{\partial \Psi}{\partial r} \stackrel{(5.43)}{=} \frac{1 + (1 + c_4)^2}{(1 + c_4)^2} \frac{S_I(r_b)}{2r_b} + \frac{S_I(r_b)}{2r_b} \left( \frac{dr_b}{d\xi} \right)^2 \quad (5.66)$$

Now the coefficients of the colored expressions are summarized. The integration constant  $c_4$  that appears explicitly is a global constant for the wake field inside and outside the blow out. To get the same expression for  $A$  and  $B$  as in recent works it is not explicitly given but rather estimated as small against  $S_I(r_b)/2$  and simultaneously large against 1 in a direct comparison. Then the functions  $A$ ,  $B$ , and  $C$  in Eq.(5.58) are

$$\mathbf{1)} \quad A(r_b) \approx 1 - \frac{S_I(r_b)}{2}, \quad (5.67)$$

$$\mathbf{2)} \quad B(r_b) = -\frac{S_I(r_b)}{r_b} - \frac{1}{2} \left[ s_i(r_b)r_b - \frac{S_I(r_b)}{r_b} \right] - \frac{S_I(r_b)}{2r_b} \quad (5.68)$$

$$\Rightarrow B(r_b) = -\frac{S_I(r_b)}{r_b} - \frac{s_i(r_b)r_b}{2} = s_0(\xi) - \frac{s_i(r_b)r_b}{2}, \quad (5.69)$$

$$\mathbf{3)} \quad C(r_b) = -\left[ 1 + \frac{1}{(1 + c_4)^2} \right] \frac{S_I(r_b)}{2r_b} \approx -\frac{S_I(r_b)}{2r_b} = \frac{s_0(\xi)}{2}. \quad (5.70)$$

Another argumentation that leads to these limits is that the potentials are sufficiently large at the blow out border. However this condition is not always fulfilled because the electron layer crosses the  $\xi$  axis at two distinctive points. At these points the argumentation fails and the coefficients do not reduce to the above shown form. for a further discussion see [46].

Summarizing the equations of motion for an electron in the sheath - the sheath current - is

$$\left[ 1 - \frac{S_I(r_b)}{2} \right] r_b \frac{d^2 r_b}{d\xi^2} - \left[ S_I(r_b) + \frac{s_i(r_b)r_b^2}{2} \right] \left( \frac{dr_b}{d\xi} \right)^2 - \frac{S_I(r_b)}{2} = \begin{cases} \lambda(\xi) & \xi_e \leq \xi \leq \xi_e + l_e \\ J_A(\xi, r_{ee}) & \xi_{ee} \leq \xi \leq \xi_{ee} + l_{ee} \\ 0 & \text{else} \end{cases} \quad (5.71)$$

### 5.3.3 Calculate the bubble fields from the sources and vice versa

Now that the bubble potentials, the equations of motion for test electrons inside the bubble, and an equation for the electron sheath current is found, it is possible to calculate the bubble fields in terms of the sources either from Maxwell's equations or from Eq.(5.10)

directly. Since there are five different solutions to  $A_z$ , one for each of five areas inside the bubble, the solution for the fields will be case sensitive, too. In the following Eq.(5.10) is followed while the derivation through Maxwell's equations is given in the appendix A as an alternative way.

The  $\varphi$ -component of the magnetic field can be calculated from the explicit form of  $A_z$  and  $A_r$  in Eqs.(5.32) - (5.36) and Eq.(5.37)

$$B_\varphi = -\frac{\partial A_r}{\partial \xi} - \frac{\partial A_z}{\partial r} = -r \frac{d\sigma}{d\xi} - \frac{\partial A_z}{\partial r}. \quad (5.72)$$

The component functions of  $\mathbf{E}$  are given by the inner wake field potential in Eq.(5.28), too, so that

$$E_r = -\frac{\partial \Psi}{\partial r} - \frac{\partial A_z}{\partial r} - \frac{\partial A_r}{\partial \xi} = -\frac{S_I}{r} - r \frac{d\sigma}{d\xi} - \frac{\partial A_z}{\partial r}, \quad (5.73)$$

$$E_z = \frac{\partial \Psi}{\partial \xi} = \frac{\partial \Psi_0}{\partial \xi} = -2\sigma. \quad (5.74)$$

With the new and most general model for the source terms inside the bubble [cmp. Eqs.(5.11) and (5.12)] five different solutions for the  $\mathbf{E}$  and  $\mathbf{B}$  field arise. They are coded in  $A_z$  which in turn is related to the fields via

$$\mathbf{B} = -\left(r \frac{d\sigma}{d\xi} + \frac{\partial A_z}{\partial r}\right) \vec{e}_\varphi, \quad \mathbf{E} = -\left(\frac{S_I}{r} + r \frac{d\sigma}{d\xi} + \frac{\partial A_z}{\partial r}\right) \vec{e}_r - 2\sigma \vec{e}_z. \quad (5.75)$$

Now that an expression is found that links the  $\mathbf{E}$  and  $\mathbf{B}$  field to the plasma and bunch source, the last step must be done. This is to invert the equations found above in order to find proper conditions for which it is possible to recalculate the sources for given fields, this means for given  $B_\varphi$ ,  $E_r$ , and  $E_z$ . For  $E_z$  this is simply

$$E_z = -2\sigma = \frac{\partial \Psi_0}{\partial \xi} = \frac{d\Psi_0}{d\xi} = -\frac{S_I(r_b)}{r_b} r'_b = s_0(\xi) r'_b(\xi) \quad (5.76)$$

independent from the region in the bubble interior. Furthermore, the  $E_z$  component always determines the current sheath density  $s_0(\xi)$  with this equation. Since the difference

between  $B_\varphi$  and  $E_r$  is also independent from the bubble region, it is always

$$B_\varphi - E_r = \frac{S_I(r)}{r} \quad (5.77)$$

$$\Rightarrow S_I(r) = (B_\varphi - E_r)r \quad (5.78)$$

$$\Rightarrow s_i(r)r = (B_\varphi - E_r) + r \frac{\partial}{\partial r}(B_\varphi - E_r) \quad (5.79)$$

$$\Rightarrow s_i(r) = \left( \frac{1}{r} + \frac{\partial}{\partial r} \right) [B_\varphi(\xi, r) - E_r(\xi, r)]. \quad (5.80)$$

Another term that needs to be calculated in every region is

$$\frac{d\sigma}{d\xi} = -\frac{1}{2} \frac{d^2\Psi_0}{d\xi^2} = -\frac{1}{2} [s'_0(\xi)r'_b(\xi) + s_0(\xi)r''_b(\xi)] \quad (5.81)$$

To get the  $r$ -dependency of the sources  $B_\varphi$  and  $E_r$  must be inverted. This, however, must be done for every sector independently. For simplicity, the following calculation assumes that  $r_b$  is already known from the sheath current ODE in Eq.(5.58).

### Region I - no electron bunch - compare Eq.(5.32)

$$\mathbf{B} = \frac{r}{2} [s'_0(\xi)r'_b(\xi) + s_0(\xi)r''_b(\xi)] \vec{e}_\varphi, \quad (5.82)$$

$$\mathbf{E} = - \left[ \frac{S_I(r)}{r} - \frac{r}{2} [s'_0(\xi)r'_b(\xi) + s_0(\xi)r''_b(\xi)] \right] \vec{e}_r + s_0(\xi)r'_b(\xi) \vec{e}_z \quad (5.83)$$

In all other regions the  $B_\varphi$  and  $E_r$  are related to the sources via

$$B_\varphi = - \left( r \frac{d\sigma}{d\xi} + \frac{\partial A_z}{\partial r} \right), \quad E_r = - \left( \frac{S_I}{r} + r \frac{d\sigma}{d\xi} + \frac{\partial A_z}{\partial r} \right), \quad (5.84)$$

so the next overviews just collect all specific forms of  $A_z$  and give the corresponding field-source relations.

In the next two overviews  $J_0$  is assumed to be constant so one degree of freedom is lost but if  $E_z$  and  $E_r$  are given it is possible to calculate from this expression all  $B_\varphi$  so that  $J_0$  is constant.

**Region II - outside the driving electron bunch - compare Eq. (5.33)**

$$B_\varphi = \frac{r}{2}[s'_0(\xi)r'_b(\xi) + s_0(\xi)r''_b(\xi)] + \frac{J_0}{2} \frac{r_e^2}{r}, \quad (5.85)$$

$$E_r = -\frac{S_I(r)}{r} + \frac{r}{2}[s'_0(\xi)r'_b(\xi) + s_0(\xi)r''_b(\xi)] + \frac{J_0}{2} \frac{r_e^2}{r} \quad (5.86)$$

$$B_\varphi - \frac{r}{2} \frac{d}{d\xi} E_z = \frac{J_0}{2} \frac{r_e^2}{r} \quad (5.87)$$

$$\Rightarrow J_0 = 2 \frac{r}{r_e^2} B_\varphi(\xi, r) - \frac{r^2}{r_e^2} E'_z(\xi) \quad (5.88)$$

**Region III - inside the driving electron bunch - compare (5.34)**

$$B_\varphi = \frac{r}{2}[s'_0(\xi)r'_b(\xi) + s_0(\xi)r''_b(\xi)] + \frac{J_0}{2} r, \quad (5.89)$$

$$E_r = -\frac{S_I(r)}{r} + \frac{r}{2}[s'_0(\xi)r'_b(\xi) + s_0(\xi)r''_b(\xi)] + \frac{J_0}{2} r \quad (5.90)$$

$$B_\varphi - \frac{r}{2} \frac{d}{d\xi} E_z = \frac{J_0}{2} r \quad (5.91)$$

$$\Rightarrow J_0 = \frac{2}{r} B_\varphi(\xi, r) - E'_z(\xi) \quad (5.92)$$

**Region IV - outside the accelerated electron bunch - compare Eq. (5.35)**

$$B_\varphi = \frac{r}{2}[s'_0(\xi)r'_b(\xi) + s_0(\xi)r''_b(\xi)] + \frac{J_A(\xi, r_{ee})}{r} \quad (5.93)$$

$$E_r = -\frac{S_I(r)}{r} + \frac{r}{2}[s'_0(\xi)r'_b(\xi) + s_0(\xi)r''_b(\xi)] + \frac{J_A(\xi, r_{ee})}{r} \quad (5.94)$$

$$B_\varphi - \frac{r}{2} \frac{d}{d\xi} E_z = \frac{J_A(\xi, r_{ee})}{r} \quad (5.95)$$

$$\Rightarrow J_A(\xi, r_{ee}) = r B_\varphi - \frac{r^2}{2} E'_z(\xi) \quad (5.96)$$

**Region V - inside the accelerated electron bunch - compare Eq. (5.36)**

$$B_\varphi = \frac{r}{2}[s'_0(\xi)r'_b(\xi) + s_0(\xi)r''_b(\xi)] + \frac{J_A(\xi, r)}{r} \quad (5.97)$$

$$E_r = -\frac{S_I(r)}{r} + \frac{r}{2}[s'_0(\xi)r'_b(\xi) + s_0(\xi)r''_b(\xi)] + \frac{J_A(\xi, r)}{r} \quad (5.98)$$

$$B_\varphi - \frac{r}{2} \frac{d}{d\xi} E_z = \frac{J_A(\xi, r)}{r} \quad (5.99)$$

$$\Rightarrow \int_0^r j_a(\xi, r') r' dr' = r B_\varphi - \frac{r^2}{2} E'_z(\xi) \quad (5.100)$$

$$\Rightarrow j_a(\xi, r) = \left( \frac{1}{r} + \frac{\partial}{\partial r} \right) B_\varphi(\xi, r) - E'_z(\xi) \quad (5.101)$$

### 5.3.4 Summary for the $\delta$ -layer model

The aim of this section was to introduce a most general model for the blow out or bubble model in terms of sources for the electron density and current

$$\rho_e = J_e = \begin{cases} J_0, & r < r_e, \quad \xi_e < \xi < \xi_e + l_e, \\ j_a(\xi, r), & r < r_{ee}, \quad \xi_{ee} < \xi < \xi_{ee} + l_{ee}, \\ 0, & \text{else} \end{cases} \quad (5.102)$$

and sources for the background plasma density

$$S(\xi, r) = J_z - \rho = \begin{cases} s_i(r), & r < r_b(\xi) \\ s_0(\xi) \delta(r - r_b), & \text{else} \end{cases}. \quad (5.103)$$

The electric and magnetic field inside the void behind the driver in a quasi-static cylindrical approximation are related to the electromagnetic potential  $\mathbf{A}$  and the wake field potential  $\Psi$  via

$$\mathbf{B} = - \left( r \frac{d\sigma}{d\xi} + \frac{\partial A_z}{\partial r} \right) \vec{e}_\varphi, \quad \mathbf{E} = - \left( \frac{S_I}{r} + r \frac{d\sigma}{d\xi} + \frac{\partial A_z}{\partial r} \right) \vec{e}_r - 2\sigma \vec{e}_z. \quad (5.104)$$

In turn the potentials inside the void are related to the sources as

$$A_z = -\frac{J_0}{4}r_e^2 - \frac{J_0}{2}r_e^2 \ln\left(\frac{r}{r_e}\right) \quad r > r_e, \quad \xi_e < \xi < \xi_e + l_e \quad (5.105)$$

$$A_z = -\frac{J_0}{4}r^2 \quad r \leq r_e, \quad \xi_e < \xi < \xi_e + l_e \quad (5.106)$$

$$A_z = -\int_0^{r_{ee}} \frac{J_A(\xi, r')}{r'} dr' - J_A(\xi, r_{ee}) \ln\left(\frac{r}{r_{ee}}\right) \quad r > r_{ee}, \quad \xi_{ee} < \xi < \xi_{ee} + l_{ee} \quad (5.107)$$

$$A_z = -\int_0^r \frac{J_A(\xi, r')}{r'} dr' \quad r \leq r_{ee}, \quad \xi_{ee} < \xi < \xi_{ee} + l_{ee} \quad (5.108)$$

$$\Psi(\xi, r) = \int S_I(r) \frac{dr}{r} + \Psi_0(\xi), \quad A_r(\xi, r) = -\frac{1}{2}r \frac{\partial \Psi_0(\xi)}{\partial \xi} \quad (5.109)$$

where

$$S_I(r) = \int_0^r s_i(r) r dr, \quad J_A(\xi, r) = \int_0^r j_a(\xi, r') r' dr', \quad \sigma(\xi) = -\frac{1}{2} \frac{d\Psi_0}{d\xi}, \quad (5.110)$$

$$\Psi_0(\xi) = -\int_{r=r_b} S_I(r) \frac{dr}{r} + c_4. \quad (5.111)$$

The inverted component functions of  $\mathbf{E}$  and  $\mathbf{B}$  give expressions for the sources in terms of the fields. This allows for a

The electron sheath radius  $r_b$  is related to the sources by an ordinary differential equation with coefficients that depend on the sources. If the driver - a short high energetic electron bunch - is substituted by a short, high intense laser pulse

## 5.4 The finite layer model

In the last section an electron beam driven blow out model was introduced that allowed to derive the inner fields in terms of sources for the electron current, the electron density, and the charge density. The model assumed that the surrounding sheath is infinitely thin and that it does not act on the driving electron bunch. In this section the plasma density is modeled with an additional finite layer that is important for a study of electron injection dynamics. Furthermore, the layer allows to demand additional continuity conditions so that - in contrast to the former model - the fields at the border are steady.

In this section the normalized electron current and charge density are modeled again as in Eq.(5.11)

$$\rho_e = J_e = \begin{cases} J_0, & r < r_e, \quad \xi_e < \xi < \xi_e + l_e \\ j_a(\xi, r), & r < r_{ee}, \quad \xi_{ee} < \xi < \xi_{ee} + l_{ee}, \\ 0, & \text{else} \end{cases} \quad (5.112)$$

For simplicity the driver densities are assumed to be constant and the volume which is occupied by the driver is modeled as a cylinder with high  $l_e$  and radius  $r_e$  [see Fig.5.2 red area III]. The electron densities inside the accelerated bunch are given in a more general way so that they depend on  $\xi$  and  $r$ . The volume of the beam load is also modeled as a cylinder with high  $l_{ee}$  and radius  $r_{ee}$  [see Fig.5.2 blue area V].

The source term for the plasma ion density and the  $\xi$ -coordinate of the electron current-density  $J_e$  of the driving and the accelerated electron bunch is modeled in comparable way as before. This time, however, the electron sheath has a small but still finite width  $\Delta$

$$S(\xi, r) = J_z - \rho = \begin{cases} s_i(r), & r < r_b(\xi) \\ s_0(\xi), & r_b(\xi) \leq r < r_b(\xi) + \Delta \\ 0, & \text{else} \end{cases} \quad (5.113)$$

Since the source is cylinder symmetric inside the blow out it only depends on the distance to the symmetry axis. Inside the sheath, however, the source depends only on the  $\xi$ -coordinate so that all currents in the sheath have no angular component. Similar to the last section  $\rho$  is the sum of the electron density and the ion density  $\rho_i$ . Furthermore  $\mathbf{J}$  is the sum of the (local) electron current density and the ion current densities  $J_i$ . In terms of the sources above inside the blow out it is

$$\rho = \rho_e + \rho_i = j_a(\xi, r) + \rho_i, \quad (5.114)$$

$$\mathbf{J} = J_z \vec{e}_z = (s_i(r) + \rho) \vec{e}_z = (j_a(\xi, r) + s_i(r) + \rho_i) \vec{e}_z, \quad (5.115)$$

$$J_i = 0. \quad (5.116)$$

The radial component of the electron and ion current density does not vanish for a single electron but the sum of all radial currents inside the bunches vanishes in the average.

According to Eq.(5.112) the interior of the bubble can be separated into five zones (see Fig.5.2). The first (gray) zone describes the interior of the bubble that is free of electrons. The 2nd (light red) and 4th (light blue) zone are free of electrons too, but the potentials depend on the bunches. The last two colored zones are the inner domains of the bunches.

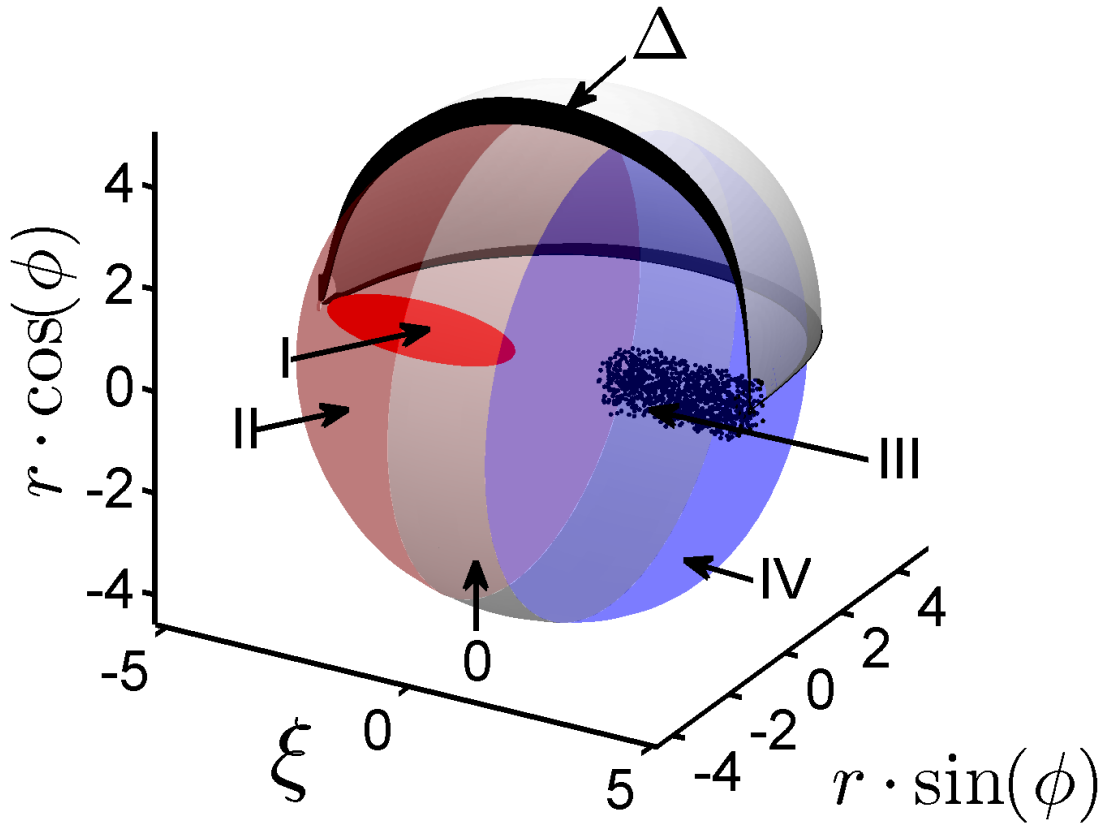


FIGURE 5.2: Five zones model of the blow out with finite sheath thickness  $\Delta$ . (I) Gray zone: empty zones, the electron bunches do not influence this zone; (II) Light red zone: also empty but the electromagnetic potential depends on the current from zone III; (III) Red zone: interior of the driving bunch; (IV) Light blue zone: empty but the electromagnetic potential depends on the current from zone V; (V) Blue zone: Interior of the accelerated electron bunch; Dashed line: External limit of the electron sheath.

The interior of the sheath is an additional 6th region. It is important for the study of injection physics but does not affect the inner fields if the thickness  $\Delta$  is much smaller than the blowout radius.

In the following subsections first the wake field potential  $\Psi$ , the vector potential  $\mathbf{A}$  and the fields are calculated from the sources in all five zones. Afterwards, the electron sheath current for is calculated in the limit that the thickness  $\Delta$  is much smaller than the blowout radius. In the last part the desired fields are given and it is determined whether a  $J_z(\xi, r)$  and a  $s_i(r)$  existed that generate these fields.

#### 5.4.1 The potentials in term of the sources

To determine the potentials in terms of the sources first the sheath source  $s_0(\xi)$  is calculated in terms of the bubble radius. Afterwards the wake field potential is calculated in all six zones. Starting point is the partial integration of the continuity equation (5.17)

under the general consideration that  $J_r \neq 0$  in the sheath and zero outside.

$$\frac{\partial \rho}{\partial t} + \nabla \cdot \mathbf{J} = 0 \quad (5.117)$$

$$\Rightarrow \frac{\partial}{\partial \xi} (\rho - J_z) + \frac{1}{r} \frac{\partial}{\partial r} (r J_r) = 0 \quad (5.118)$$

$$\Rightarrow \frac{\partial}{\partial \xi} \int_0^\infty S(\xi, r) r dr + [r J_r]_0^\infty = 0 \quad (5.119)$$

$$\Rightarrow \frac{\partial}{\partial \xi} \int_0^{r_b} S(\xi, r) r dr + \frac{\partial}{\partial \xi} \int_{r_b}^{r_b+\Delta} S(\xi, r) r dr + \frac{\partial}{\partial \xi} \int_{r_b+\Delta}^\infty S(\xi, r) r dr = 0 \quad (5.120)$$

$$\Rightarrow \int_0^{r_b} s_i(r) r dr + \frac{1}{2} [(r_b(\xi) + \Delta)^2 - r_b(\xi)^2] s_0(\xi) = -c \quad (5.121)$$

Since the left hand side of Eq.(5.121) is independent from  $r$ , the integration constant is also and in terms of the integral source from Eq.(5.21) it is

$$\int_0^{r_b} s_i(r) r dr + \frac{1}{2} [(r_b(\xi) + \Delta)^2 - r_b(\xi)^2] s_0(\xi) = -c \quad (5.122)$$

$$\Rightarrow s_0(\xi) = \frac{-2c - 2S_I(r_b(\xi))}{(r_b(\xi) + \Delta)^2 - r_b^2(\xi)} = \frac{-2c - 2S_I(r_b(\xi))}{r_b^2(\xi)[(1 + \epsilon)^2 - 1]} = -\frac{2[S_I(r_b(\xi)) + c]}{r_b^2(\xi)(X^2(\xi) - 1)}. \quad (5.123)$$

Here the relative bunch width  $\epsilon$  and the abbreviation  $X$  is are introduced. For the following calculations it is useful to introduce two additional abbreviations  $\beta$  and  $\delta$  which are related to  $\epsilon$  and  $X$  via

$$\epsilon = \frac{\Delta}{r_b}, \quad X = 1 + \epsilon \quad \delta(\xi) = \frac{X^2}{X^2 - 1}, \quad \beta(\xi) = 2\delta(\xi) \ln(X) - 1. \quad (5.124)$$

In contrast to the last section  $c$  can be used to apply a further continuity condition at the layer border so that the fields do not jump in radial direction. Before this can be done it is necessary to determine the wake field potential. This can be done by two partial integrations of the Poisson equation (5.7). According to the source in Eq.(5.113) there are three different solutions for  $\Psi(\xi, r)$

$$\Psi(\xi, r) = \int S_I(r) \frac{dr}{r} + c_1(\xi) \ln(r) + \Psi_0(\xi), \quad r \leq r_b(\xi) \quad (5.125)$$

$$\Psi(\xi, r) = \frac{s_0(\xi)}{4} r^2 + s_1(\xi) \ln(r) + \Psi_1(\xi), \quad r_b(\xi) \leq r \leq r_b(\xi) + \Delta \quad (5.126)$$

$$\Psi(\xi, r) = c_5(\xi) \ln(r) + c_6(\xi), \quad r > r_b(\xi) + \Delta. \quad (5.127)$$

The integration constants - including  $c$  from Eq.(5.121) - are deduced and simplified as follows:

1) All fields vanish outside the bubble sheath:  $r > r_b + \Delta \Rightarrow c_5(\xi) = c_6(\xi) = 0$ .

2) The fields in the bubble interior are restricted  $\Rightarrow c_1(\xi) = 0$ .

3)  $\partial_r \Psi$  is continuous in  $r = r_b$ .

$$\Rightarrow \frac{S_I(r_b)}{r_b} = \frac{s_0(\xi)}{2} r_b + \frac{s_1(\xi)}{r_b} \quad (5.128)$$

$$\stackrel{(5.123)}{\Rightarrow} s_1(\xi) = S_I(r_b) + c - c + \frac{S_I(r_b) + c}{X^2 - 1} \quad (5.129)$$

$$\stackrel{(5.124)}{\Rightarrow} s_1(\xi) = [S_I(r_b) + c]\delta(\xi) - c \quad (5.130)$$

4)  $\partial_r \Psi$  is continuous in  $r = r_b + \Delta$ .

$$\Rightarrow \frac{r_b + \Delta}{2} s_0(\xi) + \frac{s_1(\xi)}{r_b + \Delta} = 0 \quad (5.131)$$

$$\stackrel{(5.123), (5.134)}{\Rightarrow} -\frac{r_b^2 X^2}{2} \frac{2[S_I(r_b) + c]}{r_b^2 (X^2 - 1)} + [S_I(r_b) + c]\delta(\xi) - c = 0 \quad (5.132)$$

$$\stackrel{(5.124)}{\Rightarrow} c = 0 \quad (5.133)$$

$$\Rightarrow s_1(\xi) = S_I(r_b)\delta(\xi) \quad (5.134)$$

5)  $\Psi$  is continuous in  $r = r_b + \Delta$ .

$$\Rightarrow \frac{s_0(\xi)}{4} (r_b + \Delta)^2 + s_1(\xi) \ln(r_b + \Delta) + \Psi_1(\xi) = 0 \quad (5.135)$$

$$\stackrel{(5.123), (5.134)}{\Rightarrow} \Psi_1(\xi) = \frac{1}{2} S_I(r_b)\delta(\xi) - S_I(r_b)\delta(\xi) \ln(r_b X) \quad (5.136)$$

6)  $\Psi$  is continuous in  $r = r_b$ .

$$\Rightarrow \int_{r=r_b} S_I(r) \frac{dr}{r} + \Psi_0(\xi) = \frac{s_0(\xi)}{4} r_b^2 + c_3(\xi) \ln(r_b) + \Psi_1(\xi) \quad (5.137)$$

$$\stackrel{(5.123)}{\Rightarrow} \Psi_0(\xi) = - \int_{r=r_b} S_I(r) \frac{dr}{r} - \frac{S_I(r_b)}{2(X^2 - 1)} + S_I(r_b)\delta(\xi) \ln(r_b) + \Psi_1(\xi) \quad (5.138)$$

$$\stackrel{(5.136)}{\Rightarrow} \Psi_0(\xi) = - \int_{r=r_b} S_I(r) \frac{dr}{r} - \frac{S_I(r_b)}{2(X^2 - 1)} + S_I(r_b)\delta(\xi) \ln(r_b) + \frac{1}{2} S_I(r_b)\delta(\xi) - S_I(r_b)\delta(\xi) \ln(r_b X) \quad (5.139)$$

$$\Rightarrow \Psi_0(\xi) = - \int_{r=r_b} S_I(r) \frac{dr}{r} + \frac{S_I(r_b)}{2} - S_I(r_b)\delta(\xi) \ln(X) \quad (5.140)$$

$$\stackrel{(5.124)}{\Rightarrow} \Psi_0(\xi) = - \int_{r=r_b} S_I(r) \frac{dr}{r} - \frac{S_I(r_b)}{2} \beta(\xi) \quad (5.141)$$

With these integration constants the wake field potential inside the blow out, in the sheath, and outside the layer is

$$\Psi(\xi, r) = \int S_I(r) \frac{dr}{r} - \int_{r=r_b} S_I(r) \frac{dr}{r} - \frac{S_I(r_b)}{2} \beta(\xi), \quad r \leq r_b(\xi) \quad (5.142)$$

$$\begin{aligned} \Psi(\xi, r) &= -\frac{1}{2} \frac{r^2}{r_b^2(\xi)} \frac{S_I(r_b(\xi))}{(X^2(\xi) - 1)} + S_I(r_b) \delta(\xi) \ln(r) \\ &+ \frac{1}{2} S_I(r_b) \delta(\xi) - S_I(r_b) \delta(\xi) \ln(r_b X), \quad r_b(\xi) \leq r \leq r_b(\xi) + \Delta \end{aligned} \quad (5.143)$$

$$\Psi(\xi, r) = 0, \quad \text{else.} \quad (5.144)$$

This complicated appearing wake potential has the known  $r$ -dependency inside the blow out and converges to a function at the inner layer border that depends on  $\beta$  and the blow out radius  $r_b$ . As is shown later, the function  $\beta$  converges to zero for  $\epsilon \rightarrow 0$  so that in this limit both this wake potential and that from the  $\delta$ -layer model are the same.

The inner longitudinal component of the electromagnetic potential  $A_z$  only depends on the electron current in both the driving and the accelerated bunch  $J_e$ . Since the bunches are located in the bubble interior, the Poisson equation (5.7) can be solved in the same way as in the last section. The result is the same cases sensitive solution as in Eqs.(5.32) to (5.36). These five equations give the longitudinal electromagnetic field component of the blow out potentials inside the cavity. Outside the layer the potential is set to zero so that the fields vanish again. In contrast to the last section the sheath can be used to ensure that  $A_z$  is not discontinuous at the inner bunch radius  $r_b$ . In the layer the only non-vanishing source term is  $s_0(\xi)$  which is related to the inner source  $s_i$  by Eq.(5.123) and  $r_b(\xi)$ . So the fields inside the layer are determined by the wake potential solely. Similar to the last section the radial component  $A_r$  can be expressed in terms of  $\sigma(\xi) = -0.5 \partial \Psi_0(\xi) / \partial \xi$  again

$$\frac{1}{r} \frac{\partial}{\partial r} (r A_r(\xi, r)) = -\frac{\partial \Psi}{\partial \xi} \quad \Rightarrow A_r(\xi, r) = -\frac{1}{2} r \frac{\partial \Psi_0(\xi)}{\partial \xi} = r \sigma(\xi). \quad (5.145)$$

This time, however, the function  $\Psi_0$  bears information about the sheath width  $\Delta$ .

### 5.4.2 Calculate the electron sheath current

To determine the electron current in the bubble sheath it is necessary to solve the equations of motion of a test electron at positions  $r = r_b(\xi)$ . In the last section a differential equation that depends on the sources and  $r_b$  solely was derived. To achieve this first an expression for the change of the radial momentum due to a shift in  $\xi$ -direction inside the volume was calculated. Afterward the potentials were evaluated at the border. Since  $\Psi(\xi, r)$  and  $\mathbf{A}(\xi, r)$  are continuous in  $r = r_b$  and since the general equation of motion

(5.48) applies also in this section, it is possible to give an equivalent expression for a finite width layer. All that remains to do is to evaluate the potentials and their derivations at position  $r = r_b$ :

$$\Psi(\xi, r = r_b) = \int_{r=r_b} S_I(r) \frac{dr}{r} + \Psi_0(\xi) = -\frac{S_I(r_b)}{2} \beta(\xi), \quad (5.146)$$

$$A_r(\xi, r = r_b) = r_b \sigma(\xi), \quad (5.147)$$

$$\left. \frac{\partial \Psi}{\partial \xi} \right|_{r=r_b} = \frac{d\Psi_0}{d\xi} = -\frac{S_I(r_b)}{r_b} \frac{dr_b}{d\xi} - \frac{s_i(r_b)r_b}{2} \beta(r_b) \frac{dr_b}{d\xi} - \frac{S_I(r_b)}{2} \beta'(r_b) \frac{dr_b}{d\xi}, \quad (5.148)$$

$$\left. \frac{\partial \Psi}{\partial r} \right|_{r=r_b} = \frac{S_I(r_b)}{r_b}, \quad (5.149)$$

$$\left. \frac{\partial A_r}{\partial \xi} \right|_{r=r_b} = r_b \frac{d\sigma}{d\xi} \quad (5.150)$$

$$\left. \frac{A_z}{\partial r} \right|_{r=r_b} = \begin{cases} \lambda(\xi)/r_b & r_e < \xi < r_e + l_e \\ J_A(\xi, r_{ee})/r_b & r_{ee} < \xi < r_{ee} + l_{ee} \end{cases}. \quad (5.151)$$

Here, the functions  $\lambda$  and  $J_A$  are defined in Eq.(5.55) and it was used that  $\beta'(r_b) = d\beta(r_b)/dr_b$ .

The difference to the  $\delta$ -layer model is now visible. It is the appearance of the factors  $\beta$  and  $\beta'$  that bear the information about the layer with width  $\Delta$ . The equation of motion for a single electron at position  $r_b$  - the electron sheath current - can be written in the same form as in the last section [cmp. Eq.(5.58)]

$$A(r_b) \frac{d^2 r_b}{d\xi^2} + B(r_b) \left( \frac{dr_b}{d\xi} \right)^2 + C(r_b) = \begin{cases} \lambda(\xi)/r_b & \xi_e \leq \xi \leq \xi_e + l_e \\ J_A(\xi, r_{ee})/r_b & \xi_{ee} \leq \xi \leq \xi_{ee} + l_{ee} \\ 0 & \text{else} \end{cases}. \quad (5.152)$$

To determine the coefficient functions the procedure is the same as in before. This time, however, all derivatives must include the  $\beta$ -terms, too. Fortunately, all derivations are terms of  $d\sigma/d\xi$ , so it is sufficient to calculate first

$$\begin{aligned} \frac{d\sigma}{d\xi} &= -\frac{1}{2} \frac{d^2 \Psi_0}{d\xi^2} = -\frac{1}{4} \frac{d}{d\xi} \left( \left[ -2 \frac{S_I(r_b)}{r_b} - s_i(r_b)r_b\beta - S_I(r_b)\beta' \right] \frac{dr_b}{d\xi} \right) \quad (5.153) \\ \Rightarrow \frac{d\sigma}{d\xi} &= \frac{1}{4} \left[ 2 \frac{S_I(r_b)}{r_b} + s_i(r_b)r_b\beta + S_I(r_b)\beta' \right] \frac{d^2 r_b}{d\xi^2} + \frac{1}{4} S_I(r_b)\beta'' \left( \frac{dr_b}{d\xi} \right)^2 \\ &+ \frac{1}{4} \left[ 2s_i(r_b) - 2 \frac{S_I(r_b)}{r_b^2} + s_i(r_b)\beta + 2s_i(r_b)r_b\beta' + s_i'(r_b)r_b\beta \right] \left( \frac{dr_b}{d\xi} \right)^2. \quad (5.154) \end{aligned}$$

Now every summand in Eq.(5.57) is calculated anew and the different contributions to

$A$ ,  $B$ , and  $C$  are marked colored. Terms that belong to  $A(r_b)$  are marked red, those that belong to  $B(r_b)$  are marked blue and all other terms are marked green. They belong to  $C(r_b)$ .

$$(i) \quad \frac{\partial A_r}{\partial \xi} = r_b \frac{d\sigma}{d\xi} \quad (5.155)$$

$$\begin{aligned} \stackrel{(5.154)}{\Rightarrow} \frac{\partial A_r}{\partial \xi} &= \frac{1}{4} [2S_I(r_b) + s_i(r_b)r_b^2\beta + S_I(r_b)r_b\beta'] \frac{d^2r_b}{d\xi^2} + \frac{1}{4} S_I(r_b)r_b\beta'' \left(\frac{dr_b}{d\xi}\right)^2 \\ &+ \frac{1}{4} \left[ 2s_i(r_b)r_b - 2\frac{S_I(r_b)}{r_b} + s_i(r_b)r_b\beta + 2s_i(r_b)r_b^2\beta' + s'_i(r_b)r_b^2\beta \right] \left(\frac{dr_b}{d\xi}\right)^2 \end{aligned} \quad (5.156)$$

$$(ii) \quad \frac{\partial \Psi}{\partial \xi} \frac{dr_b}{d\xi} \stackrel{(5.148)}{=} - \left( \frac{S_I(r_b)}{r_b} + \frac{s_i(r_b)r_b}{2}\beta(r_b) + \frac{S_I(r_b)}{2}\beta'(r_b) \right) \left(\frac{dr_b}{d\xi}\right)^2 \quad (5.157)$$

$$(iii) \quad (1 + \Psi) \frac{d^2r_b}{d\xi^2} \stackrel{(5.146)}{=} \left( 1 - \frac{S_I(r_b)}{2}\beta(\xi) \right) \frac{d^2r_b}{d\xi^2} \quad (5.158)$$

$$(iv) \quad \left[ \frac{1 + p_r^2 + (1 + \Psi)^2}{2(1 + \Psi)^2} \right] \frac{\partial \Psi}{\partial r} = \left[ \frac{1 + p_r^2}{2(1 + \Psi)^2} + \frac{(1 + \Psi)^2}{2(1 + \Psi)^2} \right] \frac{S_I(r_b)}{r_b} \quad (5.159)$$

$$\stackrel{(5.43)}{\Rightarrow} \left[ \frac{1 + p_r^2 + (1 + \Psi)^2}{2(1 + \Psi)^2} \right] \frac{\partial \Psi}{\partial r} = \frac{S_I(r_b)}{r_b} \frac{1 + (1 + \Psi)^2}{2(1 + \Psi)^2} + \frac{S_I(r_b)}{2r_b} \left(\frac{dr_b}{d\xi}\right)^2 \quad (5.160)$$

Adding all colored terms together gives the coefficient functions

$$\mathbf{1)} \quad A(r_b) = 1 - \frac{S_I(r_b)}{2}\beta - \frac{1}{4} [2S_I(r_b) + s_i(r_b)r_b^2\beta + S_I(r_b)r_b\beta'] \quad (5.161)$$

$$\Rightarrow A(r_b) = 1 - \frac{S_I(r_b)}{2} - \frac{1}{4} (2S_I(r_b) + s_i(r_b)r_b^2)\beta - \frac{r_b}{4} S_I(r_b)\beta' \quad (5.162)$$

$$\begin{aligned} \mathbf{2)} \quad B(r_b) &= -\frac{S_I(r_b)}{r_b} - \frac{s_i(r_b)r_b}{2}\beta - \frac{S_I(r_b)}{2}\beta' - \frac{S_I(r_b)}{2r_b} - \frac{r_b}{4} S_I(r_b)\beta'' \\ &- \frac{1}{4} \left[ 2s_i(r_b)r_b - 2\frac{S_I(r_b)}{r_b} + s_i(r_b)r_b\beta + 2s_i(r_b)r_b^2\beta' + s'_i(r_b)r_b^2\beta \right] \end{aligned} \quad (5.163)$$

$$\begin{aligned} \Rightarrow B(r_b) &= - \left[ \frac{S_I(r_b)}{r_b} + \frac{s_i(r_b)r_b}{2} \right] - [3s_i(r_b)r_b + s'_i(r_b)r_b^2] \frac{\beta}{4} \\ &- [S_I(r_b) + s_i(r_b)r_b^2] \frac{\beta'}{2} - S_I(r_b)r_b \frac{\beta''}{4} \end{aligned} \quad (5.164)$$

$$\mathbf{3)} \quad C(r_b) = -\frac{1 + (1 + \Psi)^2}{2(1 + \Psi)^2} \frac{S_I(r_b)}{r_b} \quad (5.165)$$

$$\Rightarrow C(r_b) = -\frac{S_I(r_b)}{2r_b} \left( 1 + \left( 1 - \frac{S_I(r_b)}{2}\beta \right)^{-2} \right) \quad (5.166)$$

### 5.4.3 Calculate the electron sheath current in the limit $\epsilon \rightarrow 0$

To model the electron sheath usually a very thin sheath around a large bubble is assumed. A more mathematical expression for this idea is that for  $\epsilon \rightarrow 0$  the electrons generate a quasi two-dimensional surface-current density. In this case also the equation of motion for a single test electron in the bubble sheath simplifies dramatically. Of course the absolute thickness is never zero but the limit  $\epsilon \rightarrow 0$  later implies that the inner fields are independent from the sheath. This in turn is helpful because then all results from the last section can be transferred to this section.

Since all  $\beta$ ,  $\beta'$ ,  $\beta''$ , and  $r_b$  strongly depend on  $\epsilon$  this subsection derives the reduced sheath equation of motion in terms of  $X = 1 + \epsilon$  [also remember the definitions in Eq.(5.124)]. To determine the limits in Eqs.(5.162), (5.164), and(5.166) it is necessary to know the source term  $s_i(r)$  or at least how it behaves for  $r \rightarrow r_b$ . To calculate the most general limits, however, it is sufficient to assume that  $s_i$  is analytical. Then  $s_i(r)$ ,  $s'_i(r)$ , and  $S_I(r)$  are expandable in the Taylor series

$$s_i|_{r=0}(r) = \sum_{n=0}^{\infty} \frac{s_i^{(n)}(0)}{n!} r^n \quad (5.167)$$

$$s'_i|_{r=0}(r) = \sum_{n=1}^{\infty} \frac{s_i^{(n)}(0)}{n!} n r^{n-1} \quad (5.168)$$

$$S_I|_{r=0}(r) = \int_0^r s_i(r') r' dr' = \sum_{n=0}^{\infty} \frac{s_i^{(n)}(0)}{n!} \int_0^r r'^{n+1} dr' = \sum_{n=0}^{\infty} \frac{s_i^{(n)}(0)}{n!} \frac{r^{n+2}}{(n+2)} \quad (5.169)$$

around the origin and the expansions converge inside the blow out. Following the idea above these Taylor expansions are substituted into Eqs.(5.162), (5.164), and (5.166):

$$A(r_b) = 1 - \frac{S_I(r_b)}{2} - \frac{1}{4}(2S_I(r_b) + s_i(r_b)r_b^2)\beta - \frac{r_b}{4}S_I(r_b)\beta' \quad (5.170)$$

$$\Rightarrow A(r_b) = 1 - \sum_{n=0}^{\infty} \left[ \frac{s_i^{(n)}(0)}{n!} \frac{r_b^{n+2}}{2(n+2)} - \frac{1}{4} \left( \frac{2s_i^{(n)}(0)}{n!} \frac{r_b^{n+2}}{(n+2)} + \frac{s_i^{(n)}(0)}{n!} r_b^{n+2} \right) \beta \right] \\ - \frac{1}{4} \sum_{n=0}^{\infty} \frac{s_i^{(n)}(0)}{n!} \frac{r_b^{n+3}}{(n+2)} \beta' \quad (5.171)$$

$$\Rightarrow A(r_b) = 1 - \sum_{n=0}^{\infty} \frac{s_i^{(n)}(0)}{n!} r_b^{n+2} \left[ \frac{1}{2(n+2)} - \frac{1}{4} \left( \frac{2}{n+2} + 1 \right) \beta - \frac{1}{4} \frac{r_b}{(n+2)} \beta' \right] \quad (5.172)$$

$$B(r_b) = - \left[ \frac{S_I(r_b)}{r_b} + \frac{s_i(r_b)r_b}{2} \right] - [3s_i(r_b)r_b + s_i'(r_b)r_b^2] \frac{\beta}{4} \\ - [S_I(r_b) + s_i(r_b)r_b^2] \frac{\beta'}{2} - S_I(r_b)r_b \frac{\beta''}{4} \quad (5.173)$$

$$\Rightarrow B(r_b) = - \sum_{n=0}^{\infty} \left[ \frac{s_i^{(n)}(0)}{n!} \frac{r_b^{n+1}}{(n+2)} + \frac{s_i^{(n)}(0)}{2n!} r_b^{n+1} \right] \\ - \sum_{n=0}^{\infty} \left[ \frac{3s_i^{(n)}(0)}{n!} r_b^{n+1} + \frac{s_i^{(n)}(0)}{n!} n r_b^{n+1} \right] \frac{\beta}{4} \quad (5.174) \\ - \sum_{n=0}^{\infty} \left[ \frac{s_i^{(n)}(0)}{n!} \frac{r_b^{n+2}}{(n+2)} + \frac{s_i^{(n)}(0)}{n!} r_b^{n+2} \right] \frac{\beta'}{2} - \sum_{n=0}^{\infty} \frac{s_i^{(n)}(0)}{n!} \frac{r_b^{n+3}}{(n+2)} \frac{\beta''}{4}$$

$$\Rightarrow B(r_b) = - \sum_{n=0}^{\infty} \frac{s_i^{(n)}(0)}{n!} r_b^{n+1} \left[ \frac{1}{n+2} + \frac{1}{2} + \frac{n+3}{4} \beta + \frac{n+3}{n+2} r_b \frac{\beta'}{2} + \frac{r_b^2}{(n+2)} \frac{\beta''}{4} \right] \quad (5.175)$$

$$C(r_b) = - \frac{S_I(r_b)}{2r_b} \left( 1 + \left( 1 - \frac{S_I(r_b)}{2} \beta \right)^{-2} \right) \quad (5.176)$$

$$\Rightarrow C(r_b) = - \frac{S_I(r_b)}{2r_b} \left( 1 + \left( 1 - \sum_{n=0}^{\infty} \frac{s_i^{(n)}(0)}{n!} \frac{r_b^{n+2}}{2(n+2)} \beta \right)^{-2} \right) \quad (5.177)$$

All terms that must be considered in Eqs.(5.172) and (5.175) in the limit  $\epsilon \rightarrow 0$  are similar to  $\beta$ ,  $r_b\beta'$ , and  $r_b^2\beta''$ . In Eq.(5.177), however, terms like  $r^k\beta$  appear for arbitrary  $k \geq 2$ . This circumstance leads to a situation similar to that from last section where the argumentation was to assume that an integration constant, namely  $c_4$ , was larger than unity but smaller than  $S_I/2$ . In the following more general calculations this conclusion arises automatically.

To calculate the limits for the derivatives of  $\beta$  first it is necessary to differentiate with respect to  $r_b$ . With

$$\frac{d}{dr_b} = \frac{d\epsilon}{dr_b} \frac{dX}{d\epsilon} \frac{d}{dX} = -\frac{\Delta}{r_b^2} \frac{d}{dX} = -\frac{X-1}{r_b} \frac{d}{dX} = -\frac{(X-1)^2}{\Delta} \frac{d}{dX}. \quad (5.178)$$

this can be done according to

$$\beta'(r_b) = \frac{d\beta}{dr_b} = -\frac{(X-1)^2}{\Delta} \frac{d\beta}{dX} \stackrel{(5.124)}{=} -\frac{(X-1)^2}{\Delta} \frac{d}{dX} \left( 2\frac{X^2 \ln(X)}{X^2-1} - 1 \right) \quad (5.179)$$

$$\Rightarrow \beta'(r_b) = -\frac{(X-1)^2}{\Delta} \left( \frac{4X \ln(X) + 2X}{X^2-1} - \frac{4X^3 \ln(X)}{(X^2-1)^2} \right) \quad (5.180)$$

$$\Rightarrow \beta'(r_b) = -\frac{1}{\Delta} \left( \frac{-4X \ln(X) + 2X^3 - 2X}{(X+1)^2} \right) \quad (5.181)$$

and

$$\beta''(r_b) = \frac{d\beta'}{dr_b} = \frac{(X-1)^2}{\Delta^2} \frac{d}{dX} \left( (X-1)^2 \frac{d\beta}{dX} \right) \quad (5.182)$$

$$\Rightarrow \beta''(r_b) = \frac{(X-1)^2}{\Delta^2} \frac{d}{dX} \left( \frac{-4X \ln(X) + 2X^3 - 2X}{(X+1)^2} \right) \quad (5.183)$$

$$\Rightarrow \beta''(r_b) = \frac{(X-1)^2}{\Delta^2} \left( \frac{-4 \ln(X) - 4 + 6X^2 - 2}{(X+1)^2} - \frac{-8X \ln(X) + 4X^3 - 4X}{(X+1)^3} \right) \quad (5.184)$$

In the coefficient functions both  $\beta'$  and  $\beta''$  are multiplied by  $r_b$  and  $r_b^2$  respectively. Thus, the  $\Delta$  in the denominators cancel and it is

$$r_b \beta' = -\frac{1}{\Delta} \left( \frac{-4X \ln(X) + 2X^3 - 2X}{(X+1)^2} \right) \frac{\Delta}{(X-1)} = \frac{-4X \ln(X) + 2X^3 - 2X}{(X+1)^2(X-1)} \quad (5.185)$$

$$r_b^2 \beta'' = \beta'' \frac{\Delta^2}{(X-1)^2} = 2 \left( \frac{-2 \ln(X) - 2 + 3X^2 - 1}{(X+1)^2} - \frac{-4X \ln(X) + 2X^3 - 2X}{(X+1)^3} \right) \quad (5.186)$$

The limits of  $\beta$ ,  $r_b \beta'$ , and  $r_b^2 \beta''$  now vanish as

$$\lim_{\epsilon \rightarrow 0} \beta(\epsilon) = \lim_{X \rightarrow 1} \left( 2\frac{X^2 \ln(X)}{X^2-1} - 1 \right) \stackrel{l'H}{=} \lim_{X \rightarrow 1} \left( \frac{4X \ln(X) + 2X}{2X} - 1 \right) = 0. \quad (5.187)$$

$$\lim_{X \rightarrow 1} r_b \beta' = \lim_{X \rightarrow 1} \frac{4X \ln(X) - 2X^3 + 2X}{(X+1)^2(X-1)} \stackrel{l'H}{=} \lim_{X \rightarrow 1} \frac{4 \ln(X) + 4 - 6X^2 + 2}{2(X+1)(X-1) + (X+1)^2} = 0, \quad (5.188)$$

$$\lim_{X \rightarrow 1} r_b^2 \beta'' = \lim_{X \rightarrow 1} 2 \left( \frac{-2 \ln(X) - 2 + 3X^2 - 1}{(X+1)^2} - \frac{-4X \ln(X) + 2X^3 - 2X}{(X+1)^3} \right) = 0. \quad (5.189)$$

All other limits of the form  $\lim_{\epsilon \rightarrow 0} r_b^k \beta$  diverge for  $k \geq 2$  because

$$\begin{aligned} \lim_{\epsilon \rightarrow 0} r_b^k \beta &= \lim_{X \rightarrow 1} \frac{\Delta^k}{(X-1)^k} \left( 2 \frac{X^2 \ln(X)}{X^2 - 1} - 1 \right) = \Delta^k \lim_{X \rightarrow 1} \left( \frac{2X^2 \ln(X) - (X^2 - 1)}{(X-1)^{k+1}(X+1)} \right) \\ &\stackrel{vH}{=} \Delta^k \lim_{X \rightarrow 1} \left( \frac{4X \ln(X) + 2X - 2X}{(k+1)(X-1)^k(X+1) + (X-1)^{k+1}} \right) \\ &\stackrel{vH}{=} \Delta^k \lim_{X \rightarrow 1} \left( \frac{4 \ln(X) + 4}{k(k+1)(X-1)^{k-1}(X+1) + 2(k+1)(X-1)^k} \right) \end{aligned} \quad (5.190)$$

$$\Rightarrow \lim_{\epsilon \rightarrow 0} r_b^k \beta = \infty, \quad \forall k \geq 2 \quad (5.191)$$

If Eqs.(5.187), (5.188), (5.189), and (5.191) are substituted into Eqs.(5.172), (5.175), and (5.177) the coefficient functions in the limit  $\epsilon \rightarrow 0$  are

$$\lim_{\epsilon \rightarrow 0} A(r_b) = 1 - \sum_{n=0}^{\infty} \frac{s_i^{(n)}(0)}{n!} r_b^{n+2} \left[ \frac{1}{2(n+2)} \right] = 1 - \frac{S_I(r_b)}{2} \quad (5.192)$$

$$\lim_{\epsilon \rightarrow 0} B(r_b) = - \sum_{n=0}^{\infty} \frac{s_i^{(n)}(0)}{n!} r_b^{n+1} \left[ \frac{1}{n+2} + \frac{1}{2} \right] = - \left[ \frac{S_I(r_b)}{r_b} + \frac{s_i(r_b)r_b}{2} \right] \quad (5.193)$$

$$\lim_{\epsilon \rightarrow 0} C(r_b) = - \frac{S_I(r_b)}{2r_b}. \quad (5.194)$$

At this point it is important to mention that  $A$ ,  $B$ , and  $C$  converge for all possible source terms  $s_i(r)$  as long as these are analytical. Furthermore, it is now possible to write down the equation of motion for a test particle in the electron sheath in the limit of an arbitrary thin sheath. This ODE is exactly the same as in Eq.(5.71) which proves that the model of a blow out with an infinitely thin layer indeed is a useful model.

$$\left[ 1 - \frac{S_I(r_b)}{2} \right] r_b \frac{d^2 r_b}{d\xi^2} - \left[ S_I(r_b) + \frac{s_i(r_b)r_b^2}{2} \right] \left( \frac{dr_b}{d\xi} \right)^2 - \frac{S_I(r_b)}{2} = \begin{cases} \lambda(\xi) & \xi_e \leq \xi \leq \xi_e + l_e \\ J_A(\xi, r_{ee}) & \xi_{ee} \leq \xi \leq \xi_{ee} + l_{ee} \\ 0 & \text{else} \end{cases} \quad (5.195)$$

Since this section includes a layer around the blow out it is more appropriate for the study of injection physics. In the following the fields in all regions of the bubble are calculated first for a finite  $\epsilon = \Delta/r_b$  and afterwards in the limit  $\epsilon \rightarrow 0$  again.

#### 5.4.4 Calculate the fields from the sources and vice versa

Now that the wake field potential and the electromagnetic potential, the equations of motion for test electrons inside the blowout, and an equation for the electron sheath current is found, it is possible to calculate the fields in terms of the sources. Since there are five different solutions to  $A_z$ , one for each of five areas inside the bubble, the solution for the fields will be case sensitive, too. The general expression is already known from Eq.(5.75)

$$\mathbf{B} = - \left( r \frac{d\sigma}{d\xi} + \frac{\partial A_z}{\partial r} \right) \vec{e}_\varphi, \quad \mathbf{E} = - \left( \frac{S_I}{r} + r \frac{d\sigma}{d\xi} + \frac{\partial A_z}{\partial r} \right) \vec{e}_r - 2\sigma \vec{e}_z, \quad (5.196)$$

In this section, however, all coefficient functions are depending on the sheath width. This means that

$$S_I(r) = \int_0^r s_i(r') r' dr', \quad J_A(\xi, r) = \int_0^r j_a(\xi, r') r' dr', \quad \sigma(\xi) = -\frac{1}{2} \frac{d\Psi_0}{d\xi}, \quad (5.197)$$

$$\Psi_0(\xi) = - \int_{r=r_b} S_I(r) \frac{dr}{r} - \frac{S_I(r_b)}{2} \beta, \quad \beta = 2\delta(\xi) \ln(X) - 1, \quad \delta(\xi) = \frac{X^2}{X^2 - 1}, \quad (5.198)$$

$$X = 1 + \epsilon, \quad \epsilon = \frac{\Delta}{r_b}, \quad \lambda(\xi) = -\frac{1}{2} J_0 r_e^2(\xi). \quad (5.199)$$

In the limit  $\epsilon \rightarrow 0$  all these terms converge to the known terms from the  $\delta$ -layer model. Thus, all inner fields converge to those summarized in subsection 5.3.4 and since  $\Delta \ll r_b$  is assumed everywhere inside the blow out, it is justified to adopt the sources in terms of given fields from the  $\delta$ -layer model. The fields and the source inside the sheath are always given by the limit of the inner sources in Eq.(5.123).

## 5.5 Important examples

In this section some important examples are studied. The first examples calculate the ion density, the electron currents and the electron density inside the blow out from  $\rho_e = J_e$  and  $\rho_{ion}(\xi, r) = J_e(\xi, r) - s_i(r) - \rho_e = -s_i(r)$  inside the electron bunches as well as  $\rho_e = J_e = 0$  and  $\rho_{ion}(\xi, r) = -s_i(r)$  outside the bunches. Under the assumption that the driver and the accelerated bunch do not affect the sheath shape the perpendicular parts of the fields calculate like those in sector I

$$B_\varphi \stackrel{(5.82)}{=} \frac{r}{2} [s'_0(\xi) r'_b(\xi) + s_0(\xi) r''_b(\xi)], \quad E_r \stackrel{(5.83)}{=} \frac{r}{2} [s'_0(\xi) r'_b(\xi) + s_0(\xi) r''_b(\xi)] - \frac{S_I(r)}{r}. \quad (5.200)$$

The only missing variable is the explicit solution of the blow out radius  $r_b$ . This can be calculated in some special cases.

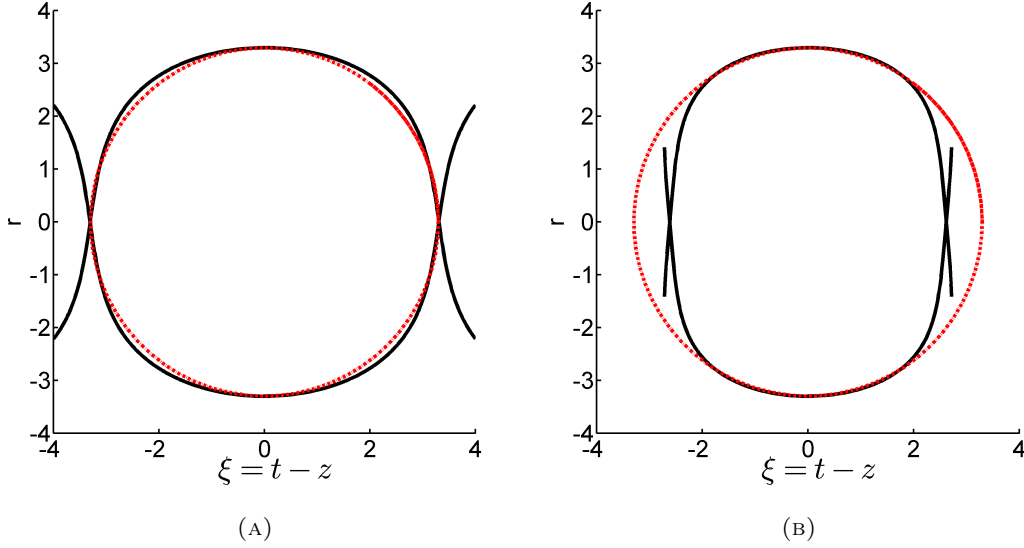


FIGURE 5.3: Electron layer shapes in black are solutions to the electron current ODE. Red circles represent former idealized bubble models. (a): Difference between a perfect sphere and the actual layer for a constant plasma density. (b): Difference between a perfect sphere and the actual layer for a linear plasma density.

### 5.5.1 $\rho_{ion}(r) = \text{const}$

For the case of a constant density the new blow out model gives the known fields from previous works. Now, however, it is possible to include a shape deformation of the electron layer due to the driver and the accelerated bunch. Since the density is normalized to the plasma background density it is  $\rho_{ion} = 1$  and thus

$$\rho_{ion} = 1 \quad \Rightarrow \quad s_i = -1 \stackrel{(5.110)}{\Rightarrow} \frac{S_i(r)}{r} = -\frac{r}{2} \stackrel{(5.23)}{\Rightarrow} s_0(\xi) = \frac{r_b(\xi)}{2}, \quad (5.201)$$

$$s_0(\xi) = \frac{r_b(\xi)}{2} \quad \Rightarrow \quad s'_0(\xi) = \frac{r'_b(\xi)}{2} \quad \Rightarrow \quad s''_0(\xi) = \frac{r''_b(\xi)}{2}, \quad (5.202)$$

$$E_z(\xi) = s_0(\xi)r'_b(\xi) = \frac{1}{2}r_b(\xi)r'_b(\xi). \quad (5.203)$$

According to Eq.(5.71) the sheath radius can be found by solving the ODE

$$\left[1 + \frac{r_b^2}{4}\right] r_b \frac{d^2 r_b}{d\xi^2} + r_b^2 \left(\frac{dr_b}{d\xi}\right)^2 + \frac{r_b^2}{4} = 0. \quad (5.204)$$

As Fig.5.3a shows the blow out is spherical near the peak and the tail but in between the shape slightly differs from a perfect sphere. In recent analytical bubble models [17, 18, 22]

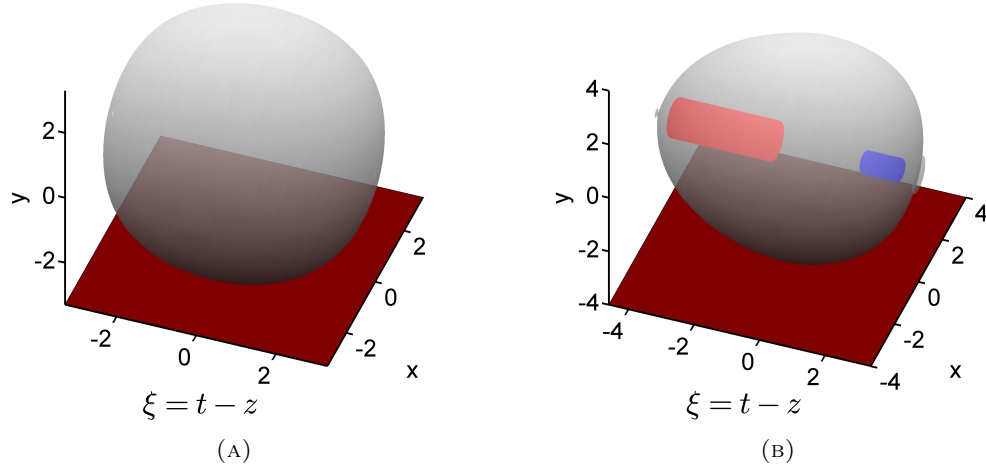


FIGURE 5.4: Plasma density and blow out radius for constant plasma density. (a): Empty volume. (b): Volume with driver and accelerated bunch.

the confining radial electrical and circular magnetic field

$$\mathbf{E} = \frac{1}{4} \begin{pmatrix} x \\ y \\ -2\xi \end{pmatrix} = \frac{r}{4} \vec{e}_r - \frac{\xi}{2} \vec{e}_z, \quad \mathbf{B} = \frac{1}{4} \begin{pmatrix} y \\ -x \\ 0 \end{pmatrix} = -\frac{r}{4} \vec{e}_\varphi \quad (5.205)$$

are calculated for a perfect sphere. In this model these fields also imply a perfect sphere because  $E_z = r_b r_b' / 2 = -\xi / 2$  gives

$$r_b r_b' = -\xi \quad \Rightarrow \quad r_b = \sqrt{c - \xi^2} \quad \Rightarrow \quad r_b^2 + \xi^2 = c. \quad (5.206)$$

In Fig.5.4 the 3D blow out is shown both as an empty volume and with a deformation due to the included bunches. The red background symbolizes the constant background density. If the bunch densities are considered the perpendicular fields are modified. Since  $r_b' = -\xi / r_b$  and  $r_b'' = -1/r_b + \xi r_b' / r_b^2$  the corrected fields inside the driver are

$$B_\varphi \stackrel{(5.89)}{=} \frac{r}{2} \left[ \frac{(r_b')^2}{2} + \frac{r_b r_b''}{2} \right] + \frac{J_0}{2} r = \left( \frac{J_0}{2} - \frac{1}{4} \right) r, \quad (5.207)$$

$$E_r \stackrel{(5.90)}{=} \frac{r}{2} \left[ \frac{(r_b')^2}{2} + \frac{r_b r_b''}{2} \right] + \frac{r}{2} + \frac{J_0}{2} r = \left( \frac{J_0}{2} + \frac{1}{4} \right) r. \quad (5.208)$$

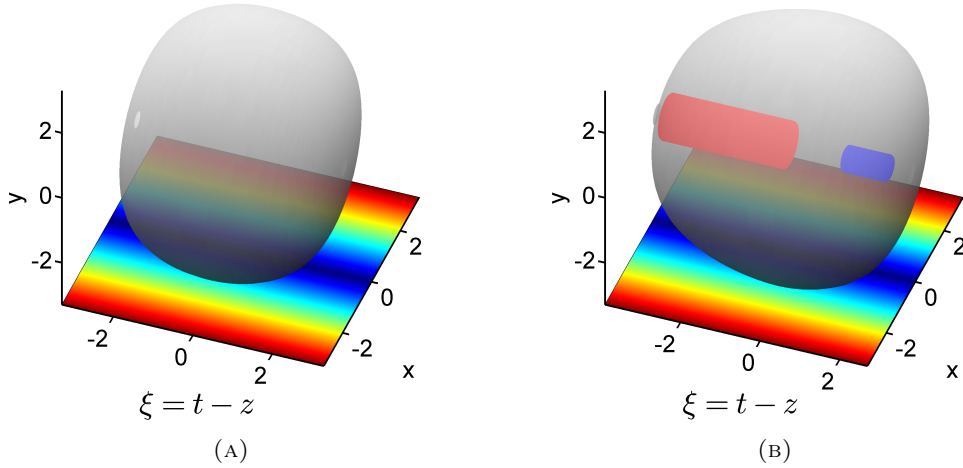


FIGURE 5.5: Plasma density and blow out radius for linear plasma density profile and  $\alpha = 1$ . (a): Empty volume. (b): Volume with driver and accelerated bunch.

Inside the accelerated electron bunch the field components are

$$B_\varphi \stackrel{(5.97)}{=} \frac{r}{2} \left[ \frac{(r'_b)^2}{2} + \frac{r_b r''_b}{2} \right] + \frac{J_A(\xi, r)}{r} = \frac{J_A(\xi, r)}{r} - \frac{1}{4}r, \quad (5.209)$$

$$E_r \stackrel{(5.98)}{=} \frac{r}{2} \left[ \frac{(r'_b)^2}{2} + \frac{r_b r''_b}{2} \right] + \frac{r}{2} + \frac{J_A(\xi, r)}{r} = \frac{J_A(\xi, r)}{r} + \frac{1}{4}r. \quad (5.210)$$

### 5.5.2 $\rho_{ion}(r) = \alpha r$

If the plasma density is linear in  $r$  the border shape is further deformed and steeper at the tail (see Fig.5.3b). The longitudinal field component can be calculated very easy as

$$\rho_{ion} = \alpha r \Rightarrow s_i = -\alpha r \stackrel{(5.110)}{\Rightarrow} \frac{S_i(r)}{r} = -\alpha \frac{r^2}{3} \stackrel{(5.23)}{\Rightarrow} s_0(\xi) = \alpha \frac{r_b(\xi)^2}{3}, \quad (5.211)$$

$$s_0(\xi) = \alpha \frac{r_b(\xi)^2}{3} \Rightarrow s'_0(\xi) = \alpha \frac{2}{3} r_b(\xi) r'_b(\xi) \Rightarrow s''_0(\xi) = \alpha \frac{2}{3} [r_b r''_b + (r'_b)^2], \quad (5.212)$$

$$E_z(\xi) = s_0(\xi) r'_b(\xi) = \frac{\alpha}{3} r_b(\xi)^2 r'_b(\xi). \quad (5.213)$$

According to Eq.(5.71) the sheath radius can be found by solving the ODE

$$\left[ 1 + \alpha \frac{r_b^3}{6} \right] r_b \frac{d^2 r_b}{d\xi^2} + \alpha \frac{5r_b^2}{6} \left( \frac{dr_b}{d\xi} \right)^2 + \alpha \frac{r_b^3}{6} = 0. \quad (5.214)$$

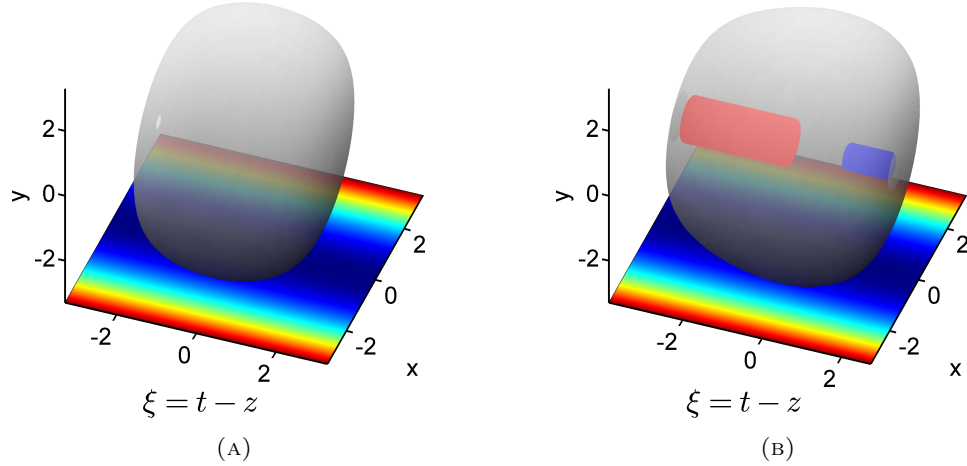


FIGURE 5.6: Plasma density and blow out radius for parabolic plasma density profile with  $\alpha = 1$ . (a): Empty volume. (b): Volume with driver and accelerated bunch.

As Fig.5.5a suggests the form of an empty blow out is more pan cake like. If the inner bunch densities are considered, however, the shape is stretched like in the previous example. The only difference is that the left and right tail are still more flattened.

### 5.5.3 $\rho_{ion}(r) = \alpha r^2$

If the plasma density is parabolic in  $r$  the border shape is further deformed and even steeper at the tail as in the linear model. In the present model the longitudinal field component and the electron sheath current are

$$\rho_{ion} = \alpha r^2 \Rightarrow s_i = -\alpha r^2 \stackrel{(5.110)}{\Rightarrow} \frac{S_i(r)}{r} = -\alpha \frac{r^3}{4} \stackrel{(5.23)}{\Rightarrow} s_0(\xi) = \alpha \frac{r_b(\xi)^3}{4}, \quad (5.215)$$

$$s_0(\xi) = \alpha \frac{r_b(\xi)^3}{4} \Rightarrow s'_0(\xi) = \alpha \frac{3}{4} r_b(\xi)^2 r'_b(\xi) \Rightarrow s''_0(\xi) = \alpha \frac{3}{4} r_b r''_b + \alpha \frac{3}{2} r_b (r'_b)^2, \quad (5.216)$$

$$E_z(\xi) = s_0(\xi) r'_b(\xi) = \frac{\alpha}{4} r_b(\xi)^3 r'_b(\xi) \quad (5.217)$$

$$\left[ 1 + \alpha \frac{r_b^4}{8} \right] r_b \frac{d^2 r_b}{d\xi^2} + \alpha \frac{3r_b^4}{4} \left( \frac{dr_b}{d\xi} \right)^2 + \alpha \frac{r_b^4}{8} = 0. \quad (5.218)$$

As Fig.5.6 shows, the plasma density is very steep at the channel border and flat in the mid. Thus the consideration of the shape adjustment to the bunch densities is almost negligible for the trapped blue bunch. The driver still elongates the blow out but compared to the last two examples the resulting shape change is rather small. In general the blow out has lost its spherical form.

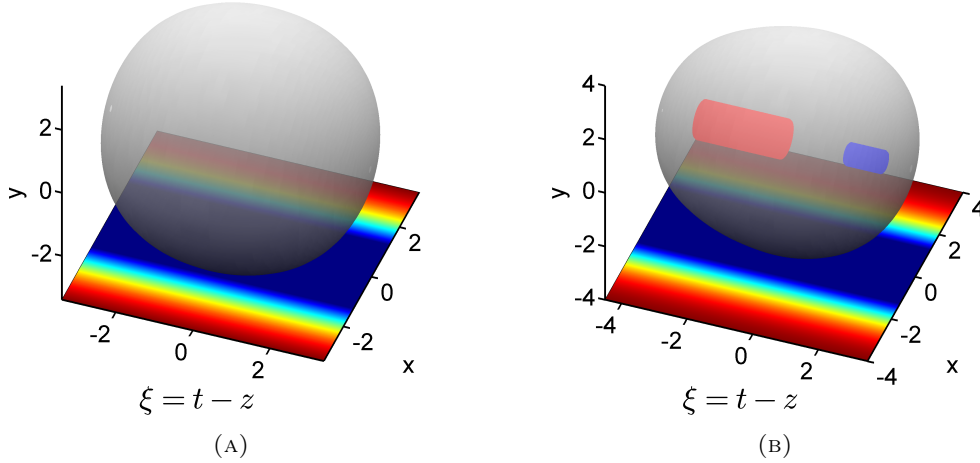


FIGURE 5.7: Plasma density and blow out radius for Gaussian plasma density profile with  $\alpha = -1.5$  and  $\sigma = 4$ . (a): Empty volume. (b): Volume with driver and accelerated bunch.

#### 5.5.4 $\rho_{ion}(r) = 1 - \alpha \exp(-r^2/\sigma^2)$

In this example a Gaussian plasma profile of the form  $\rho_{ion}(r) = \max(0, 1 - \alpha \exp(-r^2/\sigma^2))$  is assumed so that for  $\alpha > 1$  the density is not negative. If  $\alpha$  and  $\sigma$  are chosen right the accelerated bunch is accelerated in the empty part of the channel. Here the sources are simply

$$s_i(r) = 0 \quad \Rightarrow \quad \frac{S_I(r)}{r} = 0 \quad \Rightarrow \quad B_\varphi = E_r = \frac{r}{4} [(r'_b)^2 + r_b r''_b] \quad (5.219)$$

At the blow out border the density is finite so that the sources are

$$\begin{aligned} \rho_{ion} = 1 - \alpha e^{-r^2/\sigma^2} &\Rightarrow s_i = -1 + \alpha e^{-r^2/\sigma^2} \stackrel{(5.110)}{\Rightarrow} \frac{S_i(r)}{r} = -\frac{r}{2} - \frac{\alpha\sigma^2}{2r} e^{-r^2/\sigma^2}, \quad (5.220) \\ \stackrel{(5.23)}{\Rightarrow} s_0(\xi) = \frac{r_b}{2} + \frac{\alpha\sigma^2}{2r_b} e^{-r_b^2/\sigma^2} &\Rightarrow E_z(\xi) = s_0(\xi)r'_b(\xi) = \frac{r_b r'_b}{2} + \frac{\alpha\sigma^2}{2r_b} r'_b e^{-r_b^2/\sigma^2}. \end{aligned} \quad (5.221)$$

Now, that the channel density is dropped to zero on the acceleration axis the focusing electric and magnetic fields are identical. Thus the focusing force at the bunch border  $r = \rho$  is - according to Eq.(5.39) -

$$F_\perp = \frac{dp_r}{dt} = -\frac{\rho}{2} [s'_0(\xi)r'_b(\xi) + s_0(\xi)r''_b(\xi)] \left(1 - \frac{p_z}{\gamma}\right) \approx -\frac{\rho}{4\gamma^2} [s'_0(\xi)r'_b(\xi) + s_0(\xi)r''_b(\xi)]. \quad (5.222)$$

## 5.6 Summary

In this chapter two analytical models for the blow out regime of a radially symmetric plasma channel are derived. Both models hold for arbitrary radial profiles and represent the basis for tunable blow out fields. The presented analysis is done for a driving electron bunch but can easily be transferred to the bubble regime if the potentials of the driver are replaced by the laser potential and if the time averaged (over a laser period) ponderomotive force is included into the equations of motion of single test electrons.

The first model in section 5.3 describes a blow out with an infinitely thin electron layer. The layer carries a surface current that corresponds to a current generated by those electrons that are blown out from the cavity. A major result of this section is the connection between the fields, the currents, and the densities that allows to model the densities according to given fields and conversely. The form of the layer is determined by an ODE with coefficients that are given by the densities and currents. The potentials and fields inside the blow out are calculated from source terms for electron and ion density and currents. Afterward, the sources for given field configurations are calculated.

The second model considers a thin but finite electron layer around the blowout. The electron sheath current in this layer is calculated in terms of the layer width as well as in the limit that the layer is very small against the blowout radius. The inner fields and potentials are calculated in terms of sources again and around. In the limit that the relative sheath width vanishes the sheath current converges to that from the first model and the inner fields converge to the known ones, too. The advantage of the second model over the first is that the physics of electron injection can be studied in more realistic way while it is still possible to adjust the plasma density to desired fields.

A recent work that is build up on these models but is settled in the bubble regime has shown that a deep plasma channel that is (nearly) empty on-axis can strongly modify both the bubble fields, the laser dynamics, and the trapping [109]. Here the use of a deep channel demonstrates an increased effective bubble phase velocity, an improved energy gain, a longitudinal field that has a plateau and allows for mono-energetic acceleration, and a strongly reduced focusing force. Furthermore, new bubble scaling laws and field distributions for the deep channel are derived. According to these new scaling laws ultra-short pancake-like laser pulses help to match the dephasing and depletion length and thus lead to ultra high energy gains of accelerated electrons. The lack of focusing in the channel eliminates the betatron resonance and thus leads to much sharper beam energy distributions.

The last section of this chapter discusses some important examples that show how the blow out shape is deformed by the driving and the trapped electron bunch. The plasma

densities for which the shape and the fields are calculated have a constant, a linear, a square, and an exponential profile.

Results from this chapter are/will be published in the following publications:

A. Pukhov, O. Jansen, T. Tueckmantel, J. Thomas, and I. Yu. Kostyukov, *Field-reversed bubble in deep plasma channels for high quality electron acceleration*, PRL 113, 245003 (2014), published

J. Thomas, J. Pronold, A. Garbonov, I. Kostyukov, A. Pukhov, *A non-linear theory for multi-dimensional relativistic plasma wave wake fields in tailored plasma channels*, to be submitted

J. Thomas, A. Pukhov, *Delta layer model with important examples*, to be submitted

J. Thomas, J. Pronold, A. Pukhov, *Electron injection mechanisms for broken wake fields in deep plasma channels*, to be submitted

## Chapter 6

# Summary and prospect

In the past, many acceleration concepts for electrons were investigated and developed. In the field of plasma-based electron acceleration two principle methods are distinguished: the particle beam-driven plasma wake field acceleration (PWFA) and the laser-driven plasma wake field acceleration (LWFA). The latter can form a highly non-linear broken wave which leads to an electronic plasma cavity ("bubble") [10]. A similar wake field structure can be created in PWFA by a dense charged particle beam in the "blowout regime". These regimes can be used as effective electron accelerators with various possible electron injection techniques. The strong and nearly harmonic wake fields (with electric field strength of more than 100 GV/m) focus the injected electrons to the center of the cavity.

Recent injection techniques as the beat wave mechanism, the density gradient method, the ionization-based injection, the injection by (transverse) colliding laser pulses, and the self-injection of plasma background electrons have been developed. During this process the achievable electron energy has been continuously raised. Recent experiments report form bunches with energies above 10 GeV and numerical simulations suggest that the limit is not reached by far [1, 74]. The relativistic emittance of the accelerated electron bunch has been reduced to a few mm mrad while at the same time smaller energy spreads could be produced. In comparison to classical linear or circular accelerators, however, these energy spreads are rather large. Since many present-day applications base on the production of high energetic, small spread electron bunches, it is of utmost interest to develop new bubble acceleration techniques that minimize the energy spread and maximize the number of accelerated electrons.

This thesis presents a new injection mechanism that helps to reduce the energy spread under a critical value of 1% mean bunch energy and simultaneously allows to trap more than 70% of the injected electrons. Furthermore, a new bubble model is introduced that

includes radiation reaction effects for ultra-high particle energies. In this context it is analyzed again at which injection angle electron bunches must be injected to minimize the energy spread. In both cases - the model with and without radiation reaction - limiting factors like depletion are neglected.

After the second chapter has given an over view of recent and former plasma wake fields acceleration and injection techniques, the third chapter discusses the new injection mechanism for the bubble regime. Here, the lateral injection of an electron bunch under a certain angle into the bubble is investigated. Furthermore, it has been shown that the mean FWHM as well as the trapping rate can be optimized if the injection angle is chosen small enough. An analytical estimate for the maximal applicable injection angle has been found from a guiding center approximation and a multi-scale approach to the envelope approximation function of the trajectory of a single test electron.

An important conclusion of this chapter is that for high laser energies  $E \geq 50J$  and small injection angles  $\alpha \approx \pi/180$  rad the minimal FWHM of the trapped electron bunches could be pushed well under 0.5% of the actual bunch energy. At the same time, the ratio of trapped electrons stays well above 70% for all energies. The cut-off angle above which no electrons can be trapped was numerically reviewed in 3d bubble multi particle simulations and analytically evaluated in a reduced 2d model. The comparison showed that for laser energies  $E \geq 50J$  both angles are comparable but not for lower energies. Consequently, the side injection of electron bunches in the GeV-regime is a promising accelerating and focusing mechanism that will be a center of interest for the next time.

Another important aspect of the side injection, that has been ignored so far, is the effect of radiation reaction of accelerated electrons. In the bubble regime the field strengths are small compared to the Schwinger fields but if the electron energies is in the order of 10 GeV and above, radiation reaction effects become important. The most energetic simulations in this chapter involve laser energies of  $J = 1$  kJ and lead to mean electron bunch energies in the range of 23 GeV. Since the energy spread is minimized for these high energies, the forth chapter discusses the side injection and acceleration of electrons in the bubble regime under consideration of radiation. The radiation reaction is derived from a covariant formulation of the equation of motion to which a linear damping term is added. This term then is discussed and analyzed for high energies and the special form of the bubble fields that are given analytically.

It is shown that the mean FWHM as well as the trapping rate can be optimized if the injection angle is chosen small enough. An important conclusion of this chapter is that for laser energies  $E \geq 50J$  and small injection angles  $\alpha \approx \pi/180$  rad the minimal mean FWHM of the trapped electron bunches cannot be pushed under a limit of 0.5% of the actual bunch energy. At the same time, the ratio of trapped electrons stays well

above 70% for all energies. The cut-off angle above which no electrons can be trapped is numerically reviewed in 3d bubble multi particle simulations and analytically evaluated in a reduced 2d model. The comparison shows that for laser energies  $E \geq 50J$  both angles are comparable but not for lower energies. Consequently, the side injection of electron bunches in the GeV-regime is a promising accelerating and focusing mechanism that will be a center of interest for the next time. For higher laser energies the radiation reaction terms lead to a broadening of the energy spreads so that it is not possible to achieve less than 1% mean energy spread if the laser energy is above a certain limit. For small laser intensities in the bulk of  $I = 10^{19}$  W/cm<sup>2</sup> the limit is 100 kJ. For higher intensities the limit decreases so that in a simulation series with  $I = 10^{22}$  W/cm<sup>2</sup> the mean FWHM is well above 1% if the energy is higher than 10 kJ. The optimal injection angles at which most electrons can be trapped must be chosen very small for energies larger than 1 kJ and small intensities. For high intensities the optimal injection angles are in the same order of magnitude as for low energies and low intensities again.

In the last section of the forth chapter an analytical estimate of the radiated energy is calculated from a guiding center approximation to the damped single particle trajectory. It could be shown that higher laser energies need smaller injection angles than lower ones and that higher laser intensities allow higher injection angles than lower ones. The solution of the guiding center approximation also showed that for ultra-high electron energies the effective acceleration length is reduced proportional to the expected energy maximum after acceleration.

In the third and forth chapter the only limiting factor for the electron acceleration is the -damping dependent - dephasing length. Another factor that appears in experiments and PIC simulations is the depletion length after which the driver of the bubble is consumed and the bubble breaks. Recent PIC simulations and bubble models suggest that it is possible that avoid depletion if the driver runs through a plasma channel. If the plasma density drops to zero at the acceleration axis the intern bubble fields gain an additional degree of freedom. In this context the fifth chapter two analytical models for the blow out regime of a radially symmetric plasma channel are derived. Both models hold for arbitrary radial profiles and represent the basis for tunable blow out fields. The presented analysis is done for a driving electron bunch but can easily be transferred to the bubble regime if the potentials of the driver are replaced by the laser potential and if the time averaged (over a laser period) ponderomotive force is included into the equations of motion of single test electrons.

The first model in section 5.3 describes a blow out with an infinitely thin electron layer. The layer carries a surface current that corresponds to a current generated by those electrons that are blown out from the cavity. A major result of this section is the

connection between the fields, the currents, and the densities that allows to model the densities according to given fields and conversely. The form of the layer is determined by an ODE with coefficients that are given by the densities and currents. The potentials and fields inside the blow out are calculated from source terms for electron and ion density and currents. Afterward the sources for given field configurations are calculated. The second model considers a thin but finite electron layer around the blowout. The electron sheath current in this layer is calculated in terms of the layer width as well as in the limit that the layer is very small against the blowout radius. The inner fields and potentials are calculated in terms of sources again and around. In the limit that the relative sheath width vanishes the sheath current converges to that from the first model and the inner fields converge to the known ones, too. The advantage of the second model over the first is that the physics of electron injection can be studied in more realistic way while it is still possible to adjust the plasma density to desired fields.

The last section of the fifth chapter discusses some important examples that show how the blow out shape is deformed by the driving and the trapped electron bunch. The plasma densities for which the shape and the fields are calculated have a constant, a linear, a square, and an exponential profile.

A recent work that is build up on these models but is settled in the bubble regime has shown that a deep plasma channel that is (nearly) empty on the driver axis can strongly modify both the bubble fields, the laser dynamics, and the trapping [109]. Here the use of a deep channel demonstrates an increased effective bubble phase velocity, an improved energy gain, a longitudinal field that has a plateau and allows for mono-energetic acceleration, and a strongly reduced focusing force. Furthermore, new bubble scaling laws and field distributions for the deep channel are derived. According to these new scaling laws ultra-short pancake-like laser pulses help to match the dephasing and depletion length and thus lead to ultra high energy gains of accelerated electrons. The lack of focusing in the channel eliminates the betatron resonance and thus leads to much sharper beam energy distributions.

## Appendix A

# Derivations in the quasi-static cylindrical approximation for chapter 5

In section 5.2 a canonical transformation into the moving frame system

$$\xi = ct - z \quad (\text{A.1})$$

was implemented and it was assumed that all functions are quasi-static in this frame. Thus it was found that  $\partial/\partial t \equiv 0$  and the differential operators transformed according to  $\partial/\partial z \equiv -\partial/\partial \xi$  and  $\partial/\partial t \equiv +\partial/\partial \xi$ . A further symmetry in the system assumed that the plasma density and all functions are cylinder symmetric which means that in the coordinates

$$x = r \cos(\varphi), \quad y = r \sin(\varphi), \quad \xi = \xi \quad (\text{A.2})$$

all derivatives in  $\varphi$ -direction vanish. With these assumptions all first order derivatives in the co-moving frame in cylindric coordinates are

$$\text{grad}f = \nabla f = \vec{e}_r \frac{\partial f}{\partial r} + \frac{\vec{e}_\varphi}{r} \frac{\partial f}{\partial \varphi} - \vec{e}_z \frac{\partial f}{\partial \xi} \equiv \vec{e}_r \frac{\partial f}{\partial r} - \vec{e}_z \frac{\partial f}{\partial \xi} \quad (\text{A.3})$$

$$\text{div}\mathbf{A} = \frac{1}{r} \frac{\partial}{\partial r}(rA_r) + \frac{1}{r} \frac{\partial A_\varphi}{\partial \varphi} - \frac{\partial A_z}{\partial \xi} \equiv \frac{1}{r} \frac{\partial}{\partial r}(rA_r) - \frac{\partial A_z}{\partial \xi} \quad (\text{A.4})$$

$$\text{rot}\mathbf{A} = \vec{e}_r \left( \frac{1}{r} \frac{\partial A_z}{\partial \varphi} + \frac{\partial A_\varphi}{\partial \xi} \right) + \vec{e}_\varphi \left( -\frac{\partial A_r}{\partial \xi} - \frac{\partial A_z}{\partial r} \right) + \frac{\vec{e}_z}{r} \left( \frac{\partial(rA_\varphi)}{\partial r} - \frac{\partial A_r}{\partial \varphi} \right) \quad (\text{A.5})$$

$$\text{rot}\mathbf{A} = \vec{e}_r \left( \frac{\partial A_\varphi}{\partial \xi} \right) + \vec{e}_\varphi \left( -\frac{\partial A_r}{\partial \xi} - \frac{\partial A_z}{\partial r} \right) + \frac{\vec{e}_z}{r} \left( \frac{\partial(rA_\varphi)}{\partial r} \right) \quad (\text{A.6})$$

If the vector valued function  $\mathbf{A}$  represents the vector potential inside the bubble or the blow out, the cylindrical symmetry further implies that  $\mathbf{A}$  has no  $\varphi$ -component and the rotation further reduces to

$$\text{rot}\mathbf{A} \equiv -\vec{e}_\varphi \left( \frac{\partial A_r}{\partial \xi} + \frac{\partial A_z}{\partial r} \right). \quad (\text{A.7})$$

All second order derivatives in the co-moving frame in cylindric coordinates are

$$\text{div}(\text{grad}f) = \frac{1}{r} \frac{\partial}{\partial r} \left( r \frac{\partial f}{\partial r} \right) + \frac{\partial^2 f}{\partial \xi^2} \quad (\text{A.8})$$

$$\text{grad}(\text{div}\mathbf{A}) = \vec{e}_r \frac{\partial}{\partial r} \left( \frac{1}{r} \frac{\partial}{\partial r} (r A_r) - \frac{\partial A_z}{\partial \xi} \right) - \vec{e}_z \frac{\partial}{\partial \xi} \left( \frac{1}{r} \frac{\partial}{\partial r} (r A_r) - \frac{\partial A_z}{\partial \xi} \right) \quad (\text{A.9})$$

$$\Delta f = \frac{1}{r} \frac{\partial}{\partial r} \left( r \frac{\partial f}{\partial r} \right) + \frac{1}{r^2} \frac{\partial^2 f}{\partial \varphi^2} + \frac{\partial^2 f}{\partial \xi^2} = \frac{1}{r} \frac{\partial}{\partial r} \left( r \frac{\partial f}{\partial r} \right) + \frac{\partial^2 f}{\partial \xi^2} \quad (\text{A.10})$$

$$\begin{aligned} \Delta \mathbf{A} = & \left[ \frac{\partial}{\partial r} \left( \frac{1}{r} \frac{\partial}{\partial r} (r A_r) \right) + \frac{1}{r^2} \frac{\partial}{\partial \varphi} \left( \frac{\partial A_r}{\partial \varphi} - 2A_\varphi \right) + \frac{\partial^2 A_r}{\partial \xi^2} \right] \vec{e}_r \\ & + \left[ \frac{\partial}{\partial r} \left( \frac{1}{r} \frac{\partial}{\partial r} (r A_\varphi) \right) + \frac{1}{r^2} \frac{\partial}{\partial \varphi} \left( \frac{\partial A_\varphi}{\partial \varphi} + 2A_r \right) + \frac{\partial^2 A_\varphi}{\partial \xi^2} \right] \vec{e}_\varphi \\ & + \left[ \frac{1}{r} \frac{\partial}{\partial r} \left( r \frac{\partial A_z}{\partial r} \right) + \frac{1}{r^2} \frac{\partial^2 A_z}{\partial \varphi^2} + \frac{\partial^2 A_z}{\partial \xi^2} \right] \vec{e}_z \end{aligned} \quad (\text{A.11})$$

$$\begin{aligned} \Delta \mathbf{A} = & \left[ \frac{\partial}{\partial r} \left( \frac{1}{r} \frac{\partial}{\partial r} (r A_r) \right) + \frac{\partial^2 A_r}{\partial \xi^2} \right] \vec{e}_r + \left[ \frac{\partial}{\partial r} \left( \frac{1}{r} \frac{\partial}{\partial r} (r A_\varphi) \right) + \frac{\partial^2 A_\varphi}{\partial \xi^2} \right] \vec{e}_\varphi \\ & + \left[ \frac{1}{r} \frac{\partial}{\partial r} \left( r \frac{\partial A_z}{\partial r} \right) + \frac{\partial^2 A_z}{\partial \xi^2} \right] \vec{e}_z \end{aligned} \quad (\text{A.12})$$

$$\Delta \mathbf{A} = \left[ \frac{\partial}{\partial r} \left( \frac{1}{r} \frac{\partial}{\partial r} (r A_r) \right) + \frac{\partial^2 A_r}{\partial \xi^2} \right] \vec{e}_r + \left[ \frac{1}{r} \frac{\partial}{\partial r} \left( r \frac{\partial A_z}{\partial r} \right) + \frac{\partial^2 A_z}{\partial \xi^2} \right] \vec{e}_z \quad (\text{A.13})$$

where the last step assumed again that the vector valued function  $\mathbf{A}$  represents the vector potential inside the bubble or the blow out and thus has no  $\varphi$ -component.

# Bibliography

- [1] O. Jansen, T. Tückmantel, and A. Pukhov. Scaling electron acceleration in the bubble regime for upcoming lasers. *Eur. Phys. J. Special Topics*, 223:1017–1030, 2014.
- [2] D. Strickland and G. Mourou. Compression of amplified chirped optical pulses. *Opt. Commun.*, 56:219–221, 1985.
- [3] M. Martinez, E. Gaul, T. Ditmire, S. Douglas, D. Gorski, W. Henderson, J. Blakeney, D. Hammond, M. Gerity, J. Caird, A. Erlandson, I. Iovanovic, C. Ebberts, and B. Molander. The texas petawatt laser. *Proc. SPIE 5991, Laser-Induced Damage in Optical Materials: 2005*, 5991(1), 2006.
- [4] M. Perry. Crossing the petawatt threshold. *LLNL Science and Technology Review*, 4, 1996.
- [5] C. A. Haynam, R. A. Sacks, P. J. Wegner, M. W. Bowers, S. N. Dixit, G. V. Erbert, G. M. Heestand, M. A. Henesian, M. R. Hermann, K. S. Jancaitis, K. R. Manes, C. D. Marshall, N. C. Mehta, J. Menapace, M. C. Nostrand, C. D. Orth, M. J. Shaw, S. B. Sutton, W. H. Williams, C. C. Widmayer, R. K. White, S. T. Yang, and B. M. Van Wonterghem. The national ignition facility 2007 laser performance status. *Journal of Phys.: Conf Ser*, 112(3):032004, 2008.
- [6] M. Marklund and P. K. Shukla. Nonlinear collective effects in photon-photon and photon-plasma interactions. *Rev. Mod. Phys.*, 78(591), 2006.
- [7] J. M. Dawson. Nonlinear electron oscillations in a cold plasma. *Phys. Rev.*, 113:383, 1959.
- [8] T. Tajima and J. M. Dawson. Laser electron accelerator. *Phys. Rev. Lett.*, 43:267, 1979.
- [9] E. Esarey, P. Sprangle, J Krall, and A. Ting. Overview of plasma-based accelerator concepts. *IEEE Trans. Plas. Sci.*, 24(2):252–288, 1996.

- 
- [10] A. Pukhov and J. Meyer ter Vehn. Laser wake field acceleration: The highly non-linear broken-wave regime. *Appl. Phys. B*, 74:355, 2002.
- [11] J.B. Rosenzweig, B. Breizman, T. Katsouleas, and J.J. Su. Acceleration and focusing of electrons in two-dimensional nonlinear plasma wake fields. *Phys. Rev. A*, Vol. 44 Nr. 10:R6189–R6192, 1991.
- [12] K.V. Lotov. Blowout regimes of plasma wakefield acceleration. *Phys. Rev. E*, 69: 046405, 2004.
- [13] P. Chen, J.M. Dawson, R.W. Huff, and T. Katsouleas. Acceleration of electrons by the interaction of a bunched electron beam with a plasma. *Phys. Rev. Lett.*, 54(7): 693–696, 1985.
- [14] I. Kostyukov, A. Pukhov, and S. Kiselev. Phenomenological theory of laser-plasma interaction in "bubble" regime. *Phys. Plasmas*, 11m(11):5256–5264, 2004.
- [15] S. V. Bulanov, F. Pegoraro, A. M. Pukhov, and A. S. Sakharov. Transverse-wake wave breaking. *Phys. Rev. Lett.*, 78(22):4205–4208, 1997.
- [16] W. Lu, M. Tzoufras, C. Joshi, F.S. Tsung, W.B. Mori, J. Vieira, R.A. Fonseca, and L.O. Silva. Generating multi-GeV electron bunches using single stage laser wf acc. in a 3d nonlin. regime. *Phys. Rev. STAccel. Beams*, 10:061301, 2007.
- [17] I. Kostyukov, E. Nerush, A. Pukhov, and V. Seredov. A multidimensional theory for electron trapping by plasma wake generated in the bubble regime. *New J. Phys.*, 12:045009, 2010.
- [18] J. Thomas, A. Pukhov, and I. Yu Kostyukov. Temporal and spatial expansion of a multi-dimensional model for electron acceleration in the bubble regime. *Laser and Particle Beams*, 32:277–284, 2014.
- [19] E. Oz, S. Deng, T. Katsouleas, P. Muggli, BarnesC.D., I. Blumenfeld, F.J. Decker, P. Emma, M.J. Hogan, R. Ischebeck, R.H. Iverson, N. Kirby, P. Krejci, C. O'Connell, R.H. Siemann, D. Walz, D. Auerbach, C.E. Clayton, C. Huang, D.K. Johnson, C. Joshi, W. Lu, K.A. Marsh, W.B Mori, , and M. Zhou. Ionization-induced electron trapping in ultrarelativistic plasma wakes. *Phys. Rev. Lett.*, 98: 084801, 2007.
- [20] B. Hidding, G. Pretzler, J. B. Rosenzweig, T. Königstein, D. Schiller, and D. L. Bruhwiler. Ultracold electron bunch generation via plasma photocathode emission and acceleration in a beam-driven plasma blowout. *Phys. Rev. Lett.*, 108:035001, 2012.

- [21] M. Chen, E. Esarey, C. G. R. Geddes, E. Cormier-Michel, C. B. Schroeder, S. S. Bulanov, C. Benedetti, L. L. Yu, S. Rykovanov, D. L. Bruhwiler, , and W. P. Leemans. Electron injection and emittance control by transverse colliding pulses in a laser-plasma accelerator. *Phys. Rev. ST Accel. Beams*, 17:051303, 2014.
- [22] I. Kostyukov, E. Nerush, A. Pukhov, and V. Seredov. Electron self-injection in multidimensional relativistic-plasma wake fields. *Phys. Rev. Lett.*, 103:175003, 2009.
- [23] S. Corde, A. Stordeur, and V. Malka. Comment on 'scalings for radiation from plasma bubbles' [ phys. plasmas 17, 056708 (2010) ]. *Phys. Plasmas*, 18:034701, 2011.
- [24] S. A. Yi, V. Khudik, C. Siemon, and G. Shvetsa. Analytic model of electromagnetic fields around a plasma bubble in the blow-out regime. *Phys. Plasmas*, 20:013108, 2013.
- [25] R. Weingartner, S. Raith, A. Popp, S. Chou, J. Wenz, K. Khrennikov, M. Heigoldt, A. R. Maier, N. Kajumba, M. Fuchs, B. Zeitler, F. Krausz, S. Karsch, and F. Grüner. Ultralow emittance electron beams from a laser-wakefield accelerator. *PRST-AB*, 15:111302, 2012.
- [26] S. Kneip, C. McGuffey, J. L. Martins, M. S. Bloom, V. Chvykov, F. Dollar, R. Fonseca, S. Jolly, G. Kalintchenko, K. Krushelnick, A. Maksimchuk, S. P. D. Mangles, Z. Najmudin, C. A. J. Palmer, K. Ta Phuoc, W. Schumaker, L. O. Silva, J. Vieira, V. Yanovsky, and A. G. R. Thomas. Characterization of transverse beam emittance of electrons from a laser-plasma wakefield accelerator in the bubble regime using betatron x-ray radiation. *Phys. Rev. ST Accel. Beams*, 15 (2):021302, 2012.
- [27] M. Schnell, A. Sävert, B. Landgraf, M. Reuter, M. Nicolai, O. Jäckel, C. Peth, T. Thiele, O. Jansen, A. Pukhov, O. Willi, M. C. Kaluza, and C. Spielmann. Deducing the electron-beam diameter in a laser-plasma accelerator using x-ray betatron radiation. *Phys. Rev. Lett.*, 108:075001, Feb 2012.
- [28] A. Pukhov and S. Gordienko. Bubble regime of wake field acceleration: similarity theory and optical scalings. *Phil. Trans. R. Soc. A*, 364:623–633, 2006.
- [29] S. Gordienko, A. Pukhov, O. Shokorov, and T. Baeva. Relativistic doppler effect: Universal spectra and zeptosecond pulses. *Phys. Rev. Lett.*, 93:135002, 2004.
- [30] H. Burkhardt. Introduction to accelerators. In *ISEF2012 students at CERN*, 2012.
- [31] W. Kruer. *The physics of laser plasma interaction*, volume ISBN-10: 0813340837. Westview Press, 1988.

- [32] P. Sprangle, E. Esarey, J. Krall, and G. Joyce. Propagation and guiding of intense laser pulses in plasmas. *Phys. Rev. Lett.*, 69(15):2200–2203, 1992.
- [33] E. Esarey, P. Sprangle, and A. Ting. Nonlinear wakefield generation and relativistic optical guiding of intense laser pulses in plasmas. *Soc. Photo-Opt. Instr. Eng.*, 1407:407–417, 1991.
- [34] E. Esarey, C.B. Schroeder, and W.P. Leemans. Physics of laser-driven plasma-based electron accelerators. *Rev. Mod. Phys.*, 81(3):1229, 2009.
- [35] P. Sprangle, E. Esarey, and A. Ting. Nonlinear interaction of intense laser pulses in plasmas. *Rhys. Rev. A*, 41:4463, 1990.
- [36] P. Sprangle, E. Esarey, and A. Ting. Nonlinear theory of intense laser-plasma interactions. *Phys. Rev. Lett.*, 64:2011, 1990.
- [37] A. I. Akhiezer and R. V. Polovin. Theory of wave motion of an electron plasma. *Sov. Phys. JETP*, 3:696, 1956.
- [38] F.S. Tsung, R. Narang, W.B. Mori, C. Joshi, R.A. Fonseca, and L.O. Silva. Near-gev-energy laser-wakefield acceleration of self-injected electrons in a centimeter-scale plasma channel. *Phys. Rev. Lett.*, 93(18):185002, 2004.
- [39] W.P. Leemans, C.W. Siders, E. Esarey, N.E. Andreev, G. Shvets, and W.B. Mori. Plasma guiding and wakefield generation for second-generation experiments. *IEEE Trans. Plas. Sci.*, 24(2):331–342, 1996.
- [40] D. Gordon, K. C. Tzeng, C. E. Clayton, A. E. Dangor, V. Malka, K. A. Marsh, A. Modena, W. B. Mori, P. Muggli, Z. Najmudin, D. Neely, C. Danson, and C. Joshi. Observation of electron energies beyond the linear dephasing limit from a laser-excited relativistic plasma wave. *Phys. Rev. Lett.*, 80(10):2133 – 2136, 1998.
- [41] V. Malka, S. Fritzler, E. Lefebvre, M.-M. Aeonard, F. Burgy, J.-P. Chambaret, J.-F. Chemin, K. Krushelnick, G. Malka, S.P.D. Mangles, Z. Najmudin, M. Pittman, J.-P. Rousseau, J.-N. Scheurer, B. Walton, and A.E. Dangor. Electron acceleration by a wakefield forced by an intense ultrashort laser pulse. *Science*, 298 (5598):1596–1600, 2002.
- [42] M.N. Rosenbluth and C.S. Liu. Excitation of plasma waves by two laser beams. *Phys. Rev. Lett.*, 29(701), 1972.
- [43] C.E. Clayton, C. Joshi, C. Darrow, and D. Umstadter. Relativistic plasma-wave excitation by collinear optical mixing. *Phys. Rev. Lett.*, 54(2343), 1985.

- [44] D. Umstadter, J. Kim, E. Esarey, E. Dodd, and T. Neubert. Resonantly laser-driven plasma waves for electron acceleration. *Phys. Rev. E*, 51(3484), 1995.
- [45] A. Modena, Z. Najmudin, A. E. Dangor, C. E. Clayton, K. A. Marsh, C. Joshi, V. Malka, C. B. Darrow, C. Danson, D. Neely, and F. N. Walsh. Electron acceleration from the breaking of relativistic plasma waves. *Nature*, 377:606, 1995.
- [46] W. Lu, C. Huang, M. Zhou, M. Tzoufras, F. S. Tsung, W. B. Mori, and T. Katsouleas. A nonlinear theory for multidimensional relativistic plasma wave wakefields. *Phys. Plasmas*, 13:056709, 2006.
- [47] I. Blumenfeld, C.E. Clayton, F.-J. Decker, M.J. Hogan, C. Huang, R. Ischebeck, R. Iverson, C. Joshi, T. Katsouleas, N. Kirby, W. Lu, K.A. Marsh, W.B. Mori, P. Muggli, E. Oz, R.H. Siemann, D. Walz, and M. Zhou. Energy doubling of 42 GeV electrons in a metre-scale plasma wakefield accelerator. *Nature*, 44:741–744, 2007.
- [48] A. Pukhov. Strong field interaction of laser radiation. *Rep. Prog. Phys.*, 66:47–101, 2003.
- [49] S. Gordienko and A. Pukhov. Scalings for ultrarelativistic laser plasma and quasi-monoenergetic electrons. *Phys. Plasmas*, 12:043109, 2005.
- [50] E. Esarey, R. F. Hubbard, W. P. Leemans, A. Ting, and P. Sprangle. Electron injection into plasma wake fields by colliding laser pulses. *Phys. Rev. Lett.*, 79:2682, 1997.
- [51] C. B. Schroeder, E. Esarey, B. A. Shadwick, and W. P. Leemans. Trapping, dark current, and wave breaking in nonlinear plasma waves. *Phys. Plasmas*, 13(3):033103, 2006.
- [52] T. Katsouleas, S. Wilks, P. Chen, J.M. Dawson, and J.J. Su. Beam loading in plasma accelerators. *Particle Accelerators*, 22:81–99, 1987.
- [53] A.G.R. Thomas. Scalings for radiation from plasma bubbles. *Phys. Plasmas*, 17(5):056708, 2010.
- [54] A. G. R. Thomas. Response to 'comment on 'scalings for radiation from plasma bubbles' [ phys. plasmas 18, 034701 (2011) ]. *Phys. Plasmas*, 18:034702, 2011.
- [55] S. Kalmykov, S. A. Yi, V. Khudik, and G. Shvets. Electron self-injection and trapping into an evolving plasma bubble. *Phys. Rev. Lett.*, 103:135004, 2009.
- [56] S. A. Yi, V. Khudik, S. Y. Kalmykov, and G. Shvets. Hamiltonian analysis of electron self-injection and acceleration into an evolving plasma bubble. *Plasma Phys. Control. Fusion*, 53:014012, 2011.

- [57] S. Y. Kalmykov, A. Beck, X. Davoine, E. Lefebvre, and B. A. Shadwick. Laser plasma acceleration with a negatively chirped pulse: all-optical control over dark current in the blowout regime. *New J. Phys.*, 14:033025, 2012.
- [58] A. Pak, K. A. Marsh, S. F. Martins, W. Lu, W. B. Mori, and C. Joshi. Injection and trapping of tunnel-ionized electrons into laser-produced wakes. *Phys. Rev. Lett.*, 104:025003, 2010.
- [59] M. Zeng, A. Davidson, W. Lu, W. An, Z.-M. Sheng, and W. B. Mori. Some observations on trapping in nonlinear multi-dimensional wakes. *AIP Conf. Proc.*, 1507:351, 2012.
- [60] G. Fubiani, E. Esarey, C. B. Schroeder, and W. P. Leemans. Beat wave injection of electrons into plasma using two interfering laser pulses. *Phys. Rev. E*, 70:016402, 2004.
- [61] D. Umstadter, J.K. Kim, and E. Dodd. Laser injection of ultrashort electron pulses into wakefield plasma waves. *Phys. Rev. Lett.*, 76(2073), 1996.
- [62] J.E. Moore. Nonlinear radiation pressure and stochasticity in ultraintense laser fields. *Phys. Rev. E*, 59:2281–2285, 1999.
- [63] S. Bulanov, N. Naumova, F. Pegoraro, and J. Sakai. Particle injection into the wave acceleration phase due to nonlinear wake wave breaking. *Phys. Rev. E.*, 58: 5257, 1998.
- [64] T.-Y. Chien, C.-L. Chang, C.-H. Lee, J.-Y. Lin, J. Wang, and S.-Y. Chen. Spatially localized self-injection of electrons in a self-modulated laser-wakefield accelerator by using a laser-induced transient density ramp. *Phys. Rev. Lett.*, 94(115003), 2005.
- [65] C. G. R. Geddes, K. Nakamura, G. R. Plateau, Cs. Toth, E. Cormier-Michel, E. Esarey, C. B. Schroeder, J. R. Cary, and W. P. Leemans. Plasma-density-gradient injection of low absolute-momentum-spread electron bunches. *Phys. Rev. Lett.*, 100:215004, 2008.
- [66] M. Tzoufras, W. Lu, F. S. Tsung, C. Huang, W. B. Mori, T. Katsouleas, J. Vieira, R. A. Fonseca, and L. O. Silva. Beam loading in the nonlinear regime of plasma-based acceleration. *Phys. Rev. Lett.*, 101:145002, 2008.
- [67] Z.-M. Sheng, K. Mima, Y. Sentoku, M. S. Jovanovic, T. Taguchi, J. Zhang, and J. Meyer-ter Vehn. Stochastic heating and acceleration of electrons in colliding laser fields in plasma. *Phys. Rev. Lett.*, 88:055004, 2002.

- [68] C. McGuffey, A. G. R. Thomas, W. Schumaker, T. Matsuoka, V. Chvykov, F. J. Dollar, G. Kalintchenko, V. Yanovsky, A. Maksimchuk, K. Krushelnick, V. Yu. Bychenkov, I. V. Glazyrin, and A. V. Karpeev. Ionization induced trapping in a laser wakefield accelerator. *Phys. Rev. Lett.*, 104:025004, 2010.
- [69] B. Shen, Y. Li, K. Nemeth, H. Shang, Y.-C. Chae, R. Soliday, R. Crowell, E. Frank, W. Gropp, and J. Cary. Electron injection by a nanowire in the bubble regime. *Phys. Plasmas*, 14:053115, 2007.
- [70] A. Pukhov and I. Kostyukov. Control of laser-wakefield acceleration by the plasma-density profile. *Phys. Rev. E*, 77:025401(R), 2008.
- [71] L. Mingping, L. Sanqiu, H. Jun, and L. Jie. Electron acceleration during the mode transition from laser wakefield to plasma wakefield acceleration with a dense-plasma wall. *Plasma Science and Technology*, 15:9, 2013.
- [72] R. M. G. M. Trines, R. Bingham, Z. Najmudin, S. Mangles, L. O. Silva, R. Fonseca, and P. A. Norreys. Electron trapping and acceleration on a downward density ramp: a two-stage approach. *New J. Phys.*, 12:045027, 2010.
- [73] J. Faure, C. Rechatin, A. Norlin, A. Lifschitz, Y. Glinec, and V. Malka. Controlled injection and acceleration of electrons in plasma wakefields by colliding laser pulses. *Nature*, 444:737, 2006.
- [74] C. E. Clayton, B. E. Blue, E. S. Dodd, C. Joshi, K. A. Marsh, W. B. Mori, S. Wang, P. Catravas, S. Chattopadhyay, E. Esarey, W. P. Leemans, R. Assmann, F. J. Decker, M. J. Hogan, R. Iverson, P. Raimondi, R. H. Siemann, D. Walz, T. Katsouleas, S. Lee, and P. Muggli. Transverse envelope dynamics of a 28.5 GeV electron beam in a long plasma. *PRL*, 88 (15):154801, 2002.
- [75] C.G.R. Geddes, Cs. Toth, J. van Tilborg, E. Esarey, C. B. Schroeder, D. Bruhwiler, C. Nieter, J. Cary, and W. P. Leemans. High-quality electron beams from a laser wakefield accelerator using plasma-channel guiding. *Nature*, 431:538, 2004.
- [76] X. Wang, R. Zgadzaj, N. Fazel, Z. Li, S. A. Yi, Xi Zhang, W. Henderson, Y.-Y. Chang, R. Korzekwa, C.-H. Tsai, H.-E. andn Pai, H. Quevedo, G. Dyer, E. Gaul, M. Martinez, A. C. Bernstein, T. Borger, M. Spinks, M. Donovan, V. Khudik, G. Shvets, T. Ditmire, and M. C. Downer. Quasi-monoenergetic laser-plasma acceleration of electrons to 2 GeV. *Nat. Com.*, 4:1988, 2013.
- [77] A. K. Upadhyay, S. A Samant, D. Sarkar, P. Jha, and S. Krishnagopal. Generation of very low energy-spread electron beams using low-intensity laser pulses in a low-density plasma. *Phys. Plasmas*, 18:033109, 2011.

- [78] S. P. D. Mangles, C. D. Murphy, Z. Najmudin, A. G. R. Thomas, J. L. Coller, A. E. Dangor, E. J. Divall, P. S. Foster, J. G. Gallacher, S. M. Hooker, D. Jaroszynski, A. J. Langley, W. B. Mori, P. A. Norreys, F. S. Tsung, R. Viskup, B. Walton, and K. Krushelnick. Monoenergetic beams of relativistic electrons from intense laser-plasma interaction. *Nature*, 431:535–538, 2004.
- [79] G. A. Mourou, T. Tajima, and S. V. Bulanov. Optics in the relativistic regime. *Rev. Mod. Phys.*, 78:309–371, 2006.
- [80] G. Lehmann and K. H. Spatschek. Energy gain of an electron by a laser pulse in the presence of radiation reaction. *Phys. Rev. E*, 84:046409, 2011.
- [81] P. A. M. Dirac. Classical theory of radiating electrons. *Proc. R. Soc. Lond A*, 148 (148), 1938.
- [82] F. Sauter. über das verhalten eines elektrons im homogenen elektrischen feld nach der relativistischen theorie diracs. *Zeitschrit für Physik*, 82:742–764, 1931.
- [83] A. R. Bell, J. G. Kirk, and I. Arkar. Possibility of prolific pair production with high-power lasers. *Phys. Rev. Lett.*, 101(200403), 2008.
- [84] J. G. Kirk, A. R. Bell, and I. Arkar. Pair production in counter-propagating laser beams. *Plasma Phys, Control. Fusion*, 51(085008), 2009.
- [85] A. M. Fedotov, N. B. Narozhny, G. Mourou, and G. Korn. Limitations on the attainable intensity of high power lasers. *Phys. Rev. Lett.*, 105(080402), 2010.
- [86] N. V. Elkina, A. M. Fedotov, I. Yu. Kostyukov, M. V. Legkov, N. B. Narozhny, E. N. Nerush, and H. Ruhl. Qed cascades induced by circularly polarized laser fields. *Phys. Rev. ST Accel. Beams*, 14:054401, 2011.
- [87] S. Gordienko, T. Baeva, and A. Pukhov. Focusing of laser-generated ion beams by a plasma cylinder: Similarity theory and the thick lens formula. *Phys. Plasmas*, 13:063103, 2006.
- [88] F. Bloch and A. Nordsieck. Note on the radiation field of the electron. *Phys. Rev.*, 52(54), 1937.
- [89] L.D. Landau, E.M. Lifschitz, L. P. Pitaevskii, and B. Berestetskii. *Landau-Lifshitz Course of Theoretical Physics, Quantum Electrodynamics*, volume 4. Reed Educational and Professional Publishing, Oxford, 1982.
- [90] J. C. Butcher and H. Messel. Electron number distribution in electron-photon showers. *Phys. Rev.*, 112(2096), 1958.

- [91] A. I. Akhiezer, N. P. Merenkov, and A. P. Rekalov. On a kinetic theory of electromagnetic showers in strong magnetic fields. *J. Phys. G*, 20(1499), 1994.
- [92] V. Anguelov and H. Vankov. Electromagnetic showers in a strong magnetic field. *J. Phys. G*, 25(1755), 1999.
- [93] L.D. Landau and E.M. Lifschitz. *Lehrbuch der Theoretischen Physik II - Klassische Feldtheorie*, volume 12. Harri Deutsch GmbH, Frankfurt am Main, 2009.
- [94] Y. Hadad, L. Labun, J. Rafelski, N. Elkina, C. Klier, and H. Ruhl. Effects of radiation reaction in relativistic laser acceleration. *Phys. Rev. D*, 82(096012), 2010.
- [95] M. Tamburini, F. Pegoraro, A. Di Piazza, C. H. Keitel, and A. Macchi. Radiation reaction effects on radiation pressure acceleration. *New J. Phys.*, 12, 2010.
- [96] M. Tabak, J. Hammer, M.E. Glinsky, W.L. Kruer, S.C. Wilks, J. Woodworth, E.M. Campbell, M.D. Perry, and Mason R.J. Ignition and high gain with ultrapowerful lasers. *Phys. Plasmas*, 1:1626, 1994.
- [97] A. Pukhov, Z.-M. Sheng, and J. Meyer-ter Vehn. Particle acceleration in relativistic laser channels. *Phys. Plasmas*, 6(7):2847–2854, 1999.
- [98] C. Gahn, G. D. Tsakiris, A. Pukhov, J. Meyer ter Vehn, G. Pretzler, P. Thirolf, D. Habs, and K. J. Witte. Multi-Mev electron beam generation by direct laser acceleration in high-density plasma channels. *Phys. Rev. Lett.*, 83(23):4772 – 4775, 1999.
- [99] E. Esarey, B. A. Shadwick, P. Catravas, and W. P. Leemans. Synchrotron radiation from electron beams in plasma-focusing channels. *Phys. Rev. E*, 65(056505.), 2002.
- [100] C. Joshi. Plasma accelerators. *Scientific American*, 294:40–47, February 2006.
- [101] C. Joshi and A. Caldwell. *Plasma Accelerators, Handbook for Elementary Particle Physics*, volume Volume III. Heidelberg, Springer, 2013.
- [102] W. Lu, C. Huang, M. M. Zhou, W. B. Mori, and T. Katsouleas. Limits of linear plasma wakefield theory for electron or positron beams. *Phys. Plasmas*, 12:063101, 2005.
- [103] W. Lu, C. Huang, M. Zhou, W. B. Mori, and T. Katsouleas. Nonlinear theory for relativistic plasma wakefields in the blowout regime. *Phys. Rev. Lett.*, 96:165002, 2006.
- [104] V. Malka. *Laser Plasma Accelerators, Laser-Plasma Interactions and Applications*. Scottish Graduate Series, 2013.

- 
- [105] J. L. Shaw, F. S. Tsung, N. Vafaei-Najafabadi, K. A. Marsh, N. Lemos, W. B. Mori, and C. Joshi. Role of direct laser acceleration in energy gained by electrons in a laser wakefield accelerator with ionization injection. *arXiv:1404.4926v1*, 2014.
- [106] C. B. Schroeder, E. Esarey, C. Benedetti, and W. Leemans. Control of focusing forces and emittances in plasma-based accelerators using near-hollow plasma channels. *Phys. Plasmas*, 20:080701, 2013.
- [107] C. B. Schroeder, C. Benedetti, E. Esarey, and W. Leemans. Beam loading in a plasma-based accelerator using a near-hollow plasma channel. *Phys. Plasmas*, 20:123115, 2013.
- [108] T. C. Chiou, T. Katsouleas, C. Decker, W. B. Mori, J. S. Wurtele, G. Shvets, and J. J. Su. Laser wake-field acceleration and optical guiding in a hollow plasma channel. *Phys. Plasmas*, 2:310, 1995.
- [109] A. Pukhov, O. Jansen, T. Tueckmantel, J. Thomas, and I. Yu. Kostyukov. Field-reversed bubble in deep plasma channels for high quality electron acceleration. *arXiv:1408.0155v2*, 2014.
- [110] P. Mora and T. M. Jr. Antonsen. Kinetic modeling of intense, short laser pulses propagating in tenuous plasmas. *Phys. Plasmas*, 4:217, 1997.

